

Design, Construction and Flight Control of a
Quad Tilt-Wing Unmanned Aerial Vehicle

by
Ertuğrul Çetinsoy

Submitted to the Graduate School of Sabancı University
in partial fulfillment of the requirements for the degree of
Doctor of Philosophy

Sabancı University

August, 2010

Design, Construction and Flight Control of a Quad Tilt-Wing
Unmanned Aerial Vehicle

APPROVED BY:

Assoc. Prof. Dr. Mustafa Ünel
(Thesis Advisor)

.....

Assoc. Prof. Dr. Mahmut Akşit
(Thesis Co-Advisor)

.....

Prof. Dr. Asif Şabanoviç

.....

Assist. Prof. Dr. Mehmet Yıldız

.....

Assist. Prof. Dr. İlyas Kandemir

.....

DATE OF APPROVAL:

.....

© Ertuğrul Çetinsoy 2010
All Rights Reserved

Design, Construction and Flight Control of a Quad Tilt-Wing Unmanned Aerial Vehicle

Ertuğrul Çetinsoy

ME, Ph.D. Thesis, 2010

Thesis Advisor: Assoc. Prof. Mustafa Ünel

Thesis Co-Advisor: Assoc. Prof. Mahmut Akşit

Keywords: UAV, Quad Tilt-Wing, IMU, Extended Kalman Filter, Sensor
Fusion, Supervisory Control, VTOL, Horizontal Flight

Abstract

Unmanned Aerial Vehicles (UAVs) are flying robots that are employed both in civilian and military applications with a steeply increasing trend. They are already used extensively in civilian applications such as law enforcement, earth surface mapping and surveillance in disasters, and in military missions such as surveillance, reconnaissance and target acquisition. As the demand on their utilization increases, novel designs with far more advances in autonomy, flight capabilities and payloads for carrying more complex and intelligent sensors are emerging. With these technological advances, people will find even newer operational fields for UAVs.

This thesis work focuses on the design, construction and flight control of a novel UAV (SUAVI: Sabancı University Unmanned Aerial Vehicle). SUAVI is an electric powered compact size quad tilt-wing UAV, which is capable of vertical takeoff and landing (VTOL) like a helicopter, and flying horizontally like an airplane by tilting its wings. It carries onboard cameras for capturing images and broadcasting them via RF communication with the ground station. In the aerodynamic and mechanical design of SUAVI, flight duration, flight speed, size, power source and missions to be carried out are taken into account. The aerodynamic design is carried out by considering the maximization of the aerodynamic efficiency and the safe flight characteristics. The components in the propulsion system are selected to optimize propulsion efficiency and fulfill the requirements of the control for a stable flight in the entire speed range. Simulation results obtained by ANSYS and

NASA FoilSimII are evaluated and motor thrust tests are conducted during this optimization process. The power source is determined by taking the weight and flight duration into account. The wings and the fuselage are shaped iteratively in fluid flow simulations. Additionally, the verification of aerodynamic design and maneuverability are assessed in the wind tunnel tests on the half-body prototype. The mechanical structure is designed to be lightweight, strong and protective, and to allow easy assembly and disassembly of SUAVI for practical use. The safety factors in the mechanical system are determined using FEM analysis in ANSYS environment. Specimens of candidate composite skin materials are prepared and tested for lightness, strength and integrity in mechanical tests. The ready for flight prototype SUAVI is produced from the selected composite material.

Dynamical model of SUAVI is obtained using Newton-Euler formulation. Aerodynamic disturbances such as wind gusts are modeled using the well-known Dryden wind turbulence model. As the flight control system, a supervisory control architecture is implemented where a Gumstix microcomputer and several Atmega16 microcontrollers are used as the high-level and low-level controllers, respectively. Gumstix computer acts as a supervisor which orchestrates switching of low-level controllers into the system and is responsible for decision making, monitoring states of the vehicle and safety checks during the entire flight. It also generates attitude references for the low-level controllers using data from GPS or camera. Various analog and digital filters are implemented to smooth out noisy sensor measurements. Extended Kalman filter is utilized to obtain reliable orientation information by fusing data from low-cost MEMS inertial sensors such as gyros, accelerometers and the compass. PID controllers are implemented for both the high-level GPS based acceleration controller and the low-level altitude and attitude controllers. External disturbances are estimated and compensated by a disturbance observer. Real-time control software is developed for the whole flight control system. SUAVI can operate in semi-autonomous mode by communicating with the ground station. A quadrotor test platform (SUQUAD: Sabancı University QUADrotor) is also produced and used for the initial performance tests of the flight control system. After successful flight tests on this platform, the control system is transferred to SUAVI. Performance of the flight control system is verified by numerous simulations and real flight experiments. VTOL and horizontal flights are successfully realized.

Dört Rotorlu Döner-Kanat bir İnsansız Hava Aracının Tasarımı, İmalatı ve Uçuş Kontrolü

Ertuğrul Çetinsoy

ME, Doktora Tezi, 2010

Tez Danışmanı: Doç. Dr. Mustafa Ünel

Tez Eş Danışmanı: Doç. Dr. Mahmut Akşit

Anahtar Kelimeler: İHA, Dört Rotorlu Döner-Kanat, IMU, Genişletilmiş Kalman Filtresi, Sensör Tümlleştirilmesi, Gözetimci Kontrol, VTOL, Yatay Uçuş

Özet

İnsansız Hava Araçları (İHA) hem sivil hem de askeri uygulamalarda her geçen gün daha çok kullanılan uçan robotlardır. Bu araçlar halihazırda kanun uygulama, gökyüzünden haritalandırma ve felaketlerde gözlem gibi sivil uygulamalarda, ve gözlem, keşif, hedef tespiti gibi askeri uygulamalarda yaygın olarak kullanılmaktadır. Bu araçların kullanımına talep arttıkça otonomi, uçuş yetenekleri ve daha kompleks ve akıllı sensörler taşıma kapasitesi daha da geliştirilmiş yeni tasarımlar ortaya çıkmaktadır. Bu teknolojik gelişmelerle beraber, insansız hava araçları için daha da yeni kullanım alanları ortaya çıkacaktır.

Bu tez çalışması yeni bir insansız hava aracının (SUAVI: Sabancı University Unmanned Aerial Vehicle) tasarım, imalat ve uçuş kontrolüne odaklanmaktadır. SUAVI, helikopter gibi dikey kalkış-iniş, kanatlarını yatırarak uçak gibi yatay uçuş yapabilen, elektrikle çalışan, küçük boyutlu bir dört-rotorlu döner-kanat insansız hava aracıdır. Üstünde, yer istasyonu ile kurulan kablosuz haberleşme yoluyla görüntü yollamak için kameralar taşımaktadır. SUAVI'nin aerodinamik ve mekanik tasarımında uçuş süresi, uçuş hızı, boyut, enerji kaynağı ve yürütülecek görevler dikkate alınmıştır. Aerodinamik tasarım, aerodinamik verimin en üst düzeye çıkarılması ve güvenli uçuş niteliklerinin elde edilmesi için yapılmıştır. İtke sistemindeki bileşenler itke üretim verimini eniyilemek ve bütün hız bandında kararlı bir uçuş sağlamak için seçilmiştir.

Bu süreçte ANSYS ve NASA FoilSimII’de elde edilen benzetim sonuçları değerlendirilmiş ve itki ölçüm testleri yapılmıştır. Enerji kaynağı, ağırlık ve uçuş süresi dikkate alınarak belirlenmiştir. Kanatlar ve gövde, döngülü hava akış testlerinde şekillendirilmiştir. Ayrıca, aerodinamik tasarım ve manevra yeteneğinin doğrulanması rüzgar tüneline yarı-gövde prototipin üzerinde tamamlanmıştır. Aracın mekanik yapısı hafif, sağlam, koruyucu olacak ve pratik kullanım için kolay montaj-demontaja izin verecek şekilde tasarlanmıştır. Mekanik sistemin güvenlik katsayıları ANSYS’te sonlu elemanlar yöntemi temelli analizlerle bulunmuştur. Kullanılmaya aday kompozit cidar numuneleri hazırlanmış; bu numunelere hafiflik, sağlamlık ve bütünlüğü koruma bakımından mekanik testler uygulanmıştır. SUAVI’nin uçuşa hazır prototipi belirlenmiş olan kompozit malzemeden üretilmiştir.

SUAVI’nin dinamik modeli Newton-Euler formülasyonu ile elde edilmiştir. Rüzgar ve rüzgar akımları gibi aerodinamik bozucular literatürde iyi bilinen Dryden rüzgar modeliyle modellenmiştir. Uçuş kontrol sistemi olarak Gumstix mikrobilgisayarın üst-seviye, bir dizi Atmega16 mikrodenetleyicinin ise alt-seviye denetleyici olarak kullanıldığı gözetimci bir kontrol mimarisi uygulanmıştır. Gumstix bilgisayar alt-seviye denetleyicilerin sistemdeki anahtarlamasını düzenleyen bir gözetimci olarak çalışmanın yanısıra karar verme işleminden, aracın verilerinin gözlenmesinden ve güvenlik kontrollerinin sürekli yürütülmesinden sorumludur. Ayrıca GPS ve görüntü tabanlı kontrol için alt-seviye denetleyicilere açılı referansları üreten bir üst-seviye denetleyici görevini yürütmektedir. Gürültülü sensör ölçümlerinin gürültüden arındırılması için çeşitli analog ve dijital filtreler uygulanmıştır. Jiroplar, ivmeölçerler gibi düşük maliyetli ataletsel MEMS sensörler ve pusuladan elde edilen verinin tümleştirilmesiyle güvenilir yönelim bilgisi elde edilmesi için Genişletilmiş Kalman Filtresi (EKF) kullanılmıştır. GPS tabanlı yüksek seviyeli kontrolör ile düşük seviyeli irtifa ve yönelim kontrolörleri olarak PID denetleyici kullanılmıştır. Dıştan bozucu etkiler bir bozucu gözlemci kullanılarak kestirilmiş ve kompanse edilmiştir. Tüm uçuş kontrol sistemi için gerçek zamanlı kontrol yazılımı geliştirilmiştir. SUAVI yer istasyonu ile haberleşerek yarı-otonom moda çalışabilir. Uçuş kontrol sisteminin ilk testlerinin yürütülmesi için dört-rotorlu helikopter test platformu (SUQUAD: Sabancı University QUADrotor) üretilmiş ve kullanılmıştır. Bu platform üzerindeki başarılı uçuş testlerinden sonra kontrol sistemi SUAVI’ye aktarılmıştır. Uçuş kontrol sisteminin performansı birçok benzetim ve gerçek uçuş testiyle doğrulanmıştır. Dikey kalkış-iniş ve yatay uçuşlar başarıyla gerçekleştirilmiştir.

Acknowledgements

It is a great pleasure to extend my sincere gratitude and appreciation to my thesis advisor Assoc. Prof. Dr. Mustafa Ünel for his precious guidance and support. I am greatly indebted to him for his excellent supervision and invaluable advises throughout my Ph.D. study.

I would like to thank Assoc. Prof. Dr. Mahmut Akşit (my thesis co-advisor), Prof. Dr. Asif Şabanoviç, Assist. Prof. Dr. Mehmet Yıldız and Assist. Prof. İlyas Kandemir for their feedbacks and spending their valuable time to serve as my jurors.

I would like to acknowledge the financial support provided by The Scientific & Technological Research Council of Turkey (TÜBİTAK) through the project “Mechanical Design, Prototyping and Flight Control of an Unmanned Autonomous Aerial Vehicle” under the grant 107M179.

I would like to thank SUAVI project members Efe Sırımoğlu, Kaan Taha Öner, Cevdet Hançer and Serhat Dikyar for their pleasant team-work and providing me with the necessary motivation during hard times.

I would like to thank all mechatronics laboratory members for their great friendship throughout my Ph.D. study.

Finally, I would like to thank my family for all their love and support throughout my life. I would like to thank by heart my current fiancée and future spouse Elif Hocaoğlu for all her support, friendship, motivation and love that fed me throughout this Ph.D. work.

Contents

1	Introduction	1
1.1	UAV Studies in the Literature	5
1.2	Motivation	15
1.3	Thesis Organization and Contributions	17
1.4	Notes	21
1.4.1	Journal Papers	21
1.4.2	Published Conference Papers	22
1.5	Nomenclature	24
2	Aerodynamic Design and Wind Tunnel Tests	29
2.1	Aerodynamic Design	29
2.1.1	Propulsion System Design	32
2.1.2	Aerodynamic Design	37
2.2	Wind Tunnel Tests	47
2.2.1	Wind Tunnel Test Facility	47
2.2.2	Aerodynamic Tests	50
3	Mechanical Design and Prototyping	68
3.1	Mechanical Design and Production of the First Prototype . . .	69
3.1.1	Mechanical Design of the First Prototype	69
3.1.2	Production of the First Prototype	73
3.2	Mechanical Design and Prototyping of the Second Prototype .	78
3.2.1	Mechanical Design of the Second Prototype	78
3.2.2	Production of the Second Prototype	84
4	Dynamical Model and Supervisory Control	90

4.1	Dynamical Model	90
4.1.1	Hybrid Frame	91
4.1.2	Newton-Euler Formulation	93
4.2	Disturbance Modeling	103
4.3	Disturbance Observer	105
4.4	Supervisory Flight Control System	108
4.4.1	The High-level Controller	111
4.4.2	The Low-level Controller	116
4.5	Overall Supervisory Control System	118
5	Flight Control System Components	121
5.1	Sensors	121
5.1.1	Inertial Measurement Unit (IMU)	121
5.1.2	Compass	122
5.1.3	Sonar	126
5.1.4	Altimeter	127
5.1.5	GPS	128
5.1.6	Airspeed Sensor with Pitot Tube	132
5.2	Filters	133
5.2.1	Analog Low-pass Filter	134
5.2.2	Digital Exponentially Weighted Moving Average Filter	136
5.3	Sensor Fusion via Kalman Filter	137
5.4	Microcontrollers	142
5.5	Overall Electronic Control System	143
6	Simulations and Experiments	151
6.1	Simulation Results	151

6.1.1	GPS Based Hover	151
6.1.2	GPS Based Trajectory Tracking	157
6.2	Experimental Results	164
6.2.1	Vertical Flight Stabilization Tests	165
6.2.2	GPS Based Hover during Vertical Flight	168
6.2.3	Horizontal Flight Tests	168
7	Concluding Remarks and Future Work	175

List of Figures

2.1	CAD model of SUAVI in vertical (a), transition (b) and horizontal (c) flight modes	31
2.2	The motor test bench	34
2.3	Relationship between the thrust and square of angular velocity for 14x7 propeller	38
2.4	Top (a) and side (b) views of the fuselage	39
2.5	The test system for the effect of wing occlusion on the slipstream	40
2.6	NACA 2410 wing profile	42
2.7	NACA 2410 airfoil	44
2.8	Spanwise air flow on wings with high angle of attack	44
2.9	Reduction of the spanwise air flow by winglets	45
2.10	Aerodynamic design of the wing	45
2.11	Streamlines showing the downwash and its effect on the rear wing	46
2.12	CAD drawing of the wind tunnel and the half model	48
2.13	Outer (a) and inner (b) view of aluminum half body	49
2.14	Half model in the wind tunnel	50
2.15	Half model with single wing in the wind tunnel	51
2.16	Lift coefficient vs angle of attack graph for one wing	52
2.17	Drag coefficient vs angle of attack graph for one wing	52
2.18	Drag coefficient vs lift coefficient graph for one wing	53
2.19	Lift vs speed graph for one wing	54
2.20	Drag vs speed graph for one wing	55
2.21	Front (a) and rear (b) wing angle of attacks in the tests of some of the wing tip choices	57

2.22	Front (a) and rear (b) motor PWM duty ratios in the tests of some of the wing tip choices	58
2.23	Current drawn by two motors for various wing tip choices . . .	59
2.24	Wing angle of attacks for steady flight at various speeds . . .	61
2.25	Motor PWM duty ratios for steady flight at various speeds . .	61
2.26	Current drawn by the half model for steady flight at various speeds	62
2.27	Pitch moment generated at steady flight wrt. front motor (a) and rear motor (b) combined PWM changes	64
2.28	Pitch moment generated at steady flight wrt. front wing (a) and rear wing (b) combined angle of attack changes	66
2.29	Front, rear motor PWMs (a) and the current drawn by two motors (b) for steady flight at various speeds under several motor voltages	67
3.1	Mechanical design of SUAVI	70
3.2	Mechanical design of the wing tilting mechanism	71
3.3	Stress analysis of the wing for the worst case scenario	72
3.4	Stress analysis of the fuselage under 2.5 g vertical acceleration	72
3.5	Production of the molds (a, b), finished mold of the wings (c) and the molds of the fuselage (d, e)	73
3.6	Hand lay-up (a, b), vacuum bagging processes (c, d, e, f), cured skin (g) and finished skin (h)	75
3.7	Wood interface parts being attached to the lower wing skin (a), near sides of the wings being glued (b), carbon composite spar being fixed to the wing (c), upper skin joining the lower skin (d), motor joining the wing (e) and the finished wing . . .	76

3.8	Matching (a) and joining of the two halves of the fuselage (b), the cover (c), assembly of the wing tilting mechanism (d), attachment of the wing tilting mechanism on the fuselage (e) and the final assembly (f)	77
3.9	SUAVI prototype in horizontal (a) and vertical (b) flight modes	77
3.10	Balsa (a), Aero-mat (b) and Aramid honeycomb (c) in flexure test	79
3.11	Specimens with balsa (a), Aero-mat (b) and Aramid honeycomb (c) core material	80
3.12	CAD model of the wing with regionally cut upper skin to reveal the details (a) and with its final shape (b)	81
3.13	CAD model of the body without covering (a), wing-tilting mechanism-carbon pipe connection (b) and the wing-tilting mechanism detail with transparent outer static structure (c) .	83
3.14	CAD model of SUAVI in horizontal (a), transition (b) and vertical (c) flight modes	84
3.15	Finished molds and inner parts of the wings (a, b) and the molds of the fuselage (c, d)	85
3.16	Hand lay-up (a), cured skin (c) and lower and the cutting marks on the skins (d, e)	86
3.17	Inner parts being attached to the lower wing skin (a), glass-bubble epoxy mixture support (b), drilling of the wing spar root for connection to the wing tilting mechanism (c), joining of the upper skin onto the wing (d), addition of aluminum ring (e) and joining of the winglet (f)	87

3.18	Wing tilting mechanism (a), the assembly of the fuselage skeleton (b), final assembly of the fuselage and the wings (c)	88
3.19	Cable connections during the assembly (a) and addition of electronic control system and batteries (b)	88
3.20	SUAVI prototype in horizontal (a) and vertical (b) flight modes	89
4.1	Coordinate frames of the aerial vehicle	91
4.2	External forces and torques acting on the vehicle	94
4.3	Effective angle of attack α_i	96
4.4	Block diagram of the closed loop disturbance observer	108
4.5	Supervisory control architecture	109
4.6	Different flight modes of SUAVI	109
4.7	PID controller	110
4.8	The processor block diagram	112
4.9	Flow diagram of the GPS based control	113
4.10	GPS based hovering control	115
4.11	GPS based waypoint navigation	117
4.12	PID altitude control system	118
4.13	PID attitude control system	118
4.14	The schematic of the supervisory control system	120
5.1	Inertial Measurement Unit (IMU) used in the system	122
5.2	Digital compass used in the system	123
5.3	The reason for the errors on the heading measurement due to one axis (a) and two axes (b) inclinations	124
5.4	Compass reading with the noise due to the vibration and without that noise	125
5.5	Ultrasonic distance sensor used in the system	126

5.6	Ultrasonic sensor used in the system	127
5.7	Sonar and altimeter measurements without motor operation (a) and during the flight (b)	128
5.8	GPS module used in the system	129
5.9	GPS measurement deviation in static conditions	129
5.10	GPS measurement on an L shaped trajectory with low speed motion	130
5.11	Visualization of GPS measurement around Sabancı University at high speed	131
5.12	Airspeed sensor with Pitot Tube used in the system	132
5.13	Calibration of the airspeed sensor in comparison with a sensi- tive airspeed measurement system	133
5.14	Raw accelerometer readings around x,y,z axes during hover . .	135
5.15	Low-pass filtered accelerometer readings around x,y,z axes during hover	136
5.16	The raw and the filtered altitude measurements from sonar . .	137
5.17	Drift in the integrated gyro data	138
5.18	Kalman filter results in roll (a) and pitch (b) with hand motion	141
5.19	Kalman filter results in roll (a) and pitch (b) during flight . .	141
5.20	Atmel Atmega16 microcontroller with DIP package	142
5.21	Overall electronic control system	143
5.22	Gumstix Overo microcomputer with its onboard camera . . .	144
5.23	Low-level control circuit	146
5.24	I2C communication circuit structure	148
5.25	Servo pulse	149
5.26	Servo control pulses generated by the RC receiver	149

5.27	Pulse width capturing operation	150
6.1	Hovering performance with disturbance observer	153
6.2	Attitude performance with disturbance observer	153
6.3	Motor thrust forces with disturbance observer	154
6.4	Wind forces acting as disturbance	155
6.5	Estimated disturbance	155
6.6	Hovering performance with disturbance observer (motion in the horizontal plane)	156
6.7	Hovering performance without disturbance observer	156
6.8	Attitude performance without disturbance observer	157
6.9	Hovering performance without disturbance observer (motion in the horizontal plane)	158
6.10	Elliptic trajectory tracking performance	159
6.11	Position tracking performance	160
6.12	Attitude tracking performance	160
6.13	Cross track error	161
6.14	Along track speed	161
6.15	Thrust forces created by rotors	162
6.16	Wind forces acting as disturbance	163
6.17	Estimated disturbance	163
6.18	Square shaped trajectory tracking performance	164
6.19	SUQUAD test platform	165
6.20	Altitude stabilization using PID	166
6.21	Attitude stabilization using PID	166
6.22	Snapshots during a vertical flight	167
6.23	Outdoor hover test with SUAVI in helicopter field	169

6.24 Outdoor hover test with SUAVI in university campus 170
6.25 Outdoor hover test with SUAVI in university campus 171
6.26 Outdoor hover test with SUAVI in amphitheater 172
6.27 Horizontal flight snapshots of SUAVI 173
6.28 Horizontal flight snapshots of SUAVI 174

List of Tables

1.1	Examples of Fixed-Wing UAVs	8
1.2	Examples of Rotary-Wing UAVs	11
1.3	Examples of other than Fixed-Wing and Rotary-Wing UAVs .	14
2.1	Maximum thrust test results	35
2.2	Thrust test results for nominal hover flight thrust	36
2.3	Thrust test values for the effect of wing occlusion	41
2.4	Motor throttle PWM percentages, wing angle of attacks and current drawn by two motors for nominal flight	60
4.1	Modeling parameters	104
6.1	Implementation Parameters for Hovering Control	152
6.2	Implementation Parameters for Waypoint Navigation	158

Chapter 1

1 Introduction

Technological advances have always played a great role in human life throughout the history. Robots constitute a very important part of today's technology, changing our lives and the methods of production. With the advances in the computer, sensor, electronics and power generation technologies, they have evolved from simple teleoperators controlled by humans for manipulating dangerous materials from a distant place [1–3] to very complex robots, such as humanoids with walking, running, stair climbing abilities [4–7] and human mimics on the face [8–10], driver robots smart enough to drive cars in city roads and highways [11–13] and micro air vehicles flying on a given trajectory and transmitting images of the ground [14–16].

Autonomous mobile robots have been a very significant family of the robots both in research and the real world applications. These robots can be categorized in three main items, which are the unmanned ground vehicles, unmanned sea and underwater vehicles, and unmanned aerial vehicles. Unmanned ground vehicles, that are already in use, are mainly vehicles with predefined tracks on the roads, where the traffic system and priorities are well-defined. Some of these vehicles are automated forklifts [17, 18], automated people movers [19, 20], automated container trucks in the ports [21], Mars Rover robot [22, 23] and Foster-Miller TALON armed military robots

[24]. There are also competitions and research on fully autonomous ground vehicles to avoid the requirement for predefined tracks and allow the cars to go everywhere autonomously [11–13].

Unmanned sea and underwater vehicles are mainly automated boats and submarines. These vehicles are used in tasks such as sea mine hunting, sea bottom investigation, ship wreck searching even at impossible depths for manned submarines, ship bottom failure detection, harbor patrolling, underwater cable control and also serve as moving targets for military training [25, 26].

Unmanned aerial vehicles (UAV) are automated forms of already existing aircraft types, however there are also a rapidly increasing number of UAV types diverging from the ordinary air vehicle designs and having a variety of additional capabilities. UAVs are free to move nearly everywhere where air exists, so they are superior to the ground and sea vehicles in terms of functionality both in civilian and military surveillance tasks. UAVs have been attracting considerable interest due to their ability to perform air missions that are monotonous, dangerous, impractical or unnecessarily expensive to be performed by a human pilot [27, 28]. They even have the potential to perform some tasks that are impossible to be performed by other means.

UAVs can be utilized in a variety of civilian applications. They can constitute a forest patrolling team for early fire detection, alerting and extinguishing. They can constitute similar teams for continuous inspection of the ships against illegal refugee transportation and bilgewater discharge for coast guard, and the inspection of cars for law enforcement. They can be used as a surveillance and emergency materials deployment platform in disasters such as floods, landslides, earthquakes, avalanches, hill climber accidents, traffic

accidents and when a ship sinks.

UAVs can also perform tasks such as pipeline control, power line control and repair, harbor patrolling, earth surface, atmosphere and environment monitoring and mapping of earth surface and geomagnetic field variations [29, 30]. They can transmit photos and videos from car and sailing boat races both for broadcasting and refereeing, from an elevation above a place to give an idea about the sight of a building to be built there, from a film set for some scene of a movie, from the periphery of a strategic building for security and from the highway for traffic surveillance [28, 31–33]. They can chase a car to keep track of a person that escapes from the police and the birds that fly in the neighborhood of the airports causing bird strikes to the airplanes. They can even be used for agricultural pesticide spraying, imaging and sensor deployment in volcanos, explosive deployment into potential avalanche zones for preventive explosions, heavy lifting as a crane onto the top of skyscrapers and communication relaying [34].

Military applications are another field for the usage of UAVs. Such applications are intelligence, surveillance, target acquisition and reconnaissance [29, 35–39] as an information source. They can also be used for attacking a target with the bombs or missiles carried on-board. Small size UAVs are very low cost vehicles when compared with human controlled airplanes. When one military airplane gets hit, it is disabled from the fighting task at all, whereas a fleet of some ten UAVs with the same investment as that airplane is nearly invulnerable, since the rest of them would continue to attack. A military manned aircraft can carry several missiles that are designed to hit relatively large targets with generous heat sources and small numbers. When confronted by numerous small UAVs, such an aircraft cannot have great chance

to survive. This is also valid for military bases, ships and ground vehicles.

A fleet of UAVs for air support would also be a great problem for coastal enemy defences when a coastal landing operation is to be performed, since they can attack all these separate targets with that large number of units. For these reasons, there are debates on the necessity of F-22 Raptor and F-35 Lightning II airplanes, that are in fact very modern and technologically superior air vehicles. There are even debates on whether these aircrafts are the last manned fighters or not [40–46]. UAVs can also be used for mine detection at low clearances from the ground and can transfer loads between the ships in a navy fleet in a much more practical manner than the manned helicopters do.

From the examples expressed for already ongoing tasks and potential tasks for UAVs, it can be seen that these vehicles have tremendous potentials for altering the methods of various tasks. Probably the most important aspect of the usage of these vehicles is that they avoid the requirement for a trained pilot, very expensive and heavy systems that are safe enough to protect the pilot, a large place for the pilot in the air vehicle and a large and expensive propulsion system including the fuel to lift all these things. Hence, the need for spending big amount of money for carrying some camera, sensors or other kinds of payload is avoided for various aerial missions.

With the help of the emerging advanced electronic systems that are smaller, lighter, computationally powerful and able to communicate and navigate, building small size autonomous aircrafts with intelligent features has become possible. As a result, there have been studies to develop UAVs in many countries around the world to be independent from the others in this strategic technology. This led to the emergence of an extensive literature on

both the theory and applications of UAVs.

1.1 UAV Studies in the Literature

Although research on UAVs has attracted interest of various research groups and companies in the last couple of decades, building UAVs is an old idea extending back to the early 20th century, to the very early days of powered flight. The first aircraft designated as a UAV is the "Aerial Torpedo" built in 1916, which was essentially a manned airplane stabilized in the air by a gyroscope produced by Lawrence and Elmer Sperry [34]. The aim in this project was to load the airplane with a warhead, make it to fly to a distant place and dive onto some enemy target, which is a similar idea with today's missiles. Due to the frequent technical problems encountered at those times and disability to control remotely, usage of UAVs could not become practical even during the World War II [28, 34].

After 1950s, especially during the Vietnam War and the Cold War, the popularity of UAVs increased with the rise of advanced electronics for remote control and onboard stabilization. Ryan Firebee was a well-known UAV, which was essentially designed as a gun practice target for jet pilots and then also used for reconnaissance. However, the rapid increase in the number of UAVs is dated to 1990s, when modern long range communication systems, advanced electronic sensors for flight and computers for image acquisition and remote control became available. Since then, the level of autonomy and number of UAVs and UAV designs grew continuously. It is reported that the number of continuing UAV design projects reached 974 in 49 countries, 85 % of them being for military utilization [28, 47].

It is apparent that the military use is still the main motivation behind

the UAV projects. The main reason is obviously that the benefit of UAVs in battlefield is very promising both for reducing the number of casualties and for increasing the impact on the enemy [47]. UAVs, especially the small ones, are generally very cost effective when compared with the other weapons in the armies. They are also generally much simpler than manned fighter aircraft and advanced missiles, so the countries that cannot build their own military aircraft can afford designing their own UAVs to become independent of others in military technology. An important reason for the low civil usage ratio of UAVs is that these systems are still costly and not autonomous enough to be widely accepted in civil use. Also, there is still a lack of civil aviation regulations for UAVs on the entire world, so a UAV aimed for civil usage can hardly be commercialized. As a result, the civil usage of UAVs is still mainly in academic research projects.

With the emergence of advanced computer systems in compact sizes, there has been a broad research attempt both to automatize and miniaturize UAVs in the last couple of decades. These research attempts have branched out UAVs to the main categories, which are the fixed-wing, rotary-wing, and other designs. Research on fixed-wing UAVs has been the oldest among all these researches and these aircrafts have been commercialized the most among all the UAVs. Ranging from a couple of ten centimeters to a couple of ten meters in wing span, these machines have become important tools of reconnaissance and even attack departments of the armies [48]. They are mainly categorized in four size groups which are HALE (High altitude, long endurance), MALE (Medium altitude, long endurance), SUAV (Small UAV) and MAV (Micro UAV) [27, 28].

HALE group consists of UAVs that are capable of flying at altitudes more

than 30000 feet above sea level (MSL) with flight durations of more than 24 hours. This group includes very large UAVs like Northrop Grumman RQ-4 Global Hawk, NASA Helios, Pathfinder and Proteus and Lockheed Martin RQ-3 Darkstar. MALE group incorporates UAVs that can fly up to 30000 feet MSL with long endurance, some of them being TAI Anka, NASA Altus, Boeing X-45, General Atomics MQ-1 Predator and IAI Heron. HALE and MALE UAVs are able to takeoff and land only on runways due to their size and weights. SUAV group includes UAVs with altitude capabilities of up to 10000 feet MSL and nearly 2 hours of endurance. This group contains UAVs that utilize runways, launchers, parachutes or hand launching at the same time. Some examples for these machines can be given as AAI RQ-2 Pioneer, Boeing Scan Eagle, Integrated Dynamics Hornet and Luna X 2000. MAV group comprises the smallest UAVs such as Bayraktar Mini UAV, AeroVironment Wasp, Lockheed Martin Desert Hawk, MiTex Buster and EMT Aladin. Some examples of fixed-wing UAVs can be seen in Table 1.1.

The advantage of fixed-wing UAVs is that they are relatively simple to control, are useful for wide-area surveillance and tracking, and have better endurance [28]. Their disadvantages are their obligation for runway, launcher, net recovery or parachutes for takeoff and landing [49] and the disability to operate in urban areas and indoors due to flight speed requirements [50].

The literature of airplane design is filled by hundreds of books and papers, and generally the autonomous controls for such aircrafts have tremendous similarities with the already commercialized autopilot systems on commercial airplanes. Today's fixed wing UAVs are still generally controlled by a human pilot at the ground station through wireless connection and use the very

Table 1.1: Examples of Fixed-Wing UAVs

Category	Model	
HALE	Northrop Grumman RQ-4 Global Hawk	
	NASA Helios	
	NASA Pathfinder	
	NASA Proteus	
	Lockheed Martin Darkstar	
MALE	TAI Anka	
	NASA Altus	
	Boeing X-45	
	General Atomics MQ-1 Predator	
	IAI Heron	
SUAV & MAV	AAI RQ-2 Pioneer	
	Boeing Scan Eagle	
	Bayraktar MINI UAV	
	AeroVironment Wasp	
	Lockheed Martin Desert Hawk	

similar design and autopilot systems as manned airplanes. However, there are new control efforts to improve the path tracking qualities of such aircraft like the CLF-based and adaptive control based works [51–53], and to enable automatic landing on runways using [49, 54, 55] and ship boards [56]. In addition, there are new efforts to incorporate image processing based abilities into the flight. This second group of research consists of topics like vision assisted landing [57–59], vision based forced landing site detection [60, 61] and vision based detection and following of structures and moving vehicles [62–64].

Research on rotary-wing UAVs began with around 30 years of delay compared to fixed-wing UAVs due to the late emergence of lightweight yaw rate gyro, which is unconditionally required for autonomous flight of these vehicles [65]. Though, there is a large variety of these drones and research on them due to their ability to perform aerial tasks in urban areas and indoors.

Rotary-wing UAVs require only some space for takeoff and landing instead of a runway, do not require any forward speed to fly and are highly maneuverable at all flight speeds [28]. They are very advantageous in these areas at the expense of not having long flight endurance and high flight speeds due to the rotating rotor [66] and of generating severe vibration transmitted to the cameras [28]. Additionally, there is a large variety of off-the-shelf rotary-wing aircrafts available for conversion to UAVs.

Rotary-wing UAVs are mainly categorized based on the rotor number and configuration instead of size, since their function and control problems are affected mainly by the configuration, not the size. Some of these categories are conventional mono-rotor helicopters with tail rotor, coaxial contra rotor helicopters, and multiple rotor helicopters [66, 67].

Conventional mono-rotor UAVs are generally the large ones intended for outdoor utilization due to the fact that the main rotor needs to have a large diameter to carry reasonable payload consisting of the flight control electronics, cameras and adequate amount of fuel or batteries [68]. Some examples for this group of UAVs are Baykar Malazgirt, Yamaha R-Max, Zala 421-02, Schiebel S-100, Helion of National University of Singapore [69, 70], Dragon Warrior of US Naval Research Laboratories, Northrop Grumman MQ-8 Fire Scout and Boeing Hummingbird [50, 65].

Coaxial contra rotor UAVs have the advantage of not wasting energy for yaw-control and lifting useful payload at a more reasonable propeller diameter when compared with mono-rotor UAVs. For this reason, they can also be used in indoor applications. Some examples for this group of UAVs are the μ Flying Robot by Seiko-Epson and Chiba University weighing only 12.3 g with an onboard camera and radio link for image transmission to the ground station [34], EMT Fancopter [71] and Skybotix CoaX Autonomous UAV Micro Helicopter.

Multiple rotor helicopters constitute a large proportion of the UAV helicopters, especially in the academic research area. These UAVs have several, generally fixed-pitch airplane propellers, avoiding the requirement of mechanically complex swashplate and transmission structures [72] and the thrusts generated by the motors are changed through motor rotation speed changes. There are a variety of them having three tilting rotors [67], three rotors with only one tilting for yaw compensation [30], coaxial trirotors [47, 73], quadrotors [50, 74–78], hexa-rotors [79] and octo-rotors [80], the most popular ones being quad-rotors that are also commercially available. Some examples of fixed-wing UAVs can be seen in Table 1.2.

Table 1.2: Examples of Rotary-Wing UAVs

Category	Model	
Conventional mono-rotor	Baykar Malazgirt	
	Yamaha R-Max	
	Zala 421 – 02	
	Schiebel S-100	
	Helion of National University of Singapore	
Coaxial	EADS Sharc	
	Ezycopter EzyUAV	
	Seiko-Epson-Chiba University μ FRII	
	EMT Fancopter	
	Skybotix Coax	
Multi-rotor	Trirotor of Université de Technologie de Compiègne	
	Draganflyer X4	
	Microdrones MD4-1000	
	Quadrotor of Starmac Team	
	MikroKopter HexaKopter	

The research on these machines has been focused on their control and intelligent features rather than their mechanical and aerodynamic design, since helicopter design has already a well-established theory. Due to the difficult stability problem, the literature on rotary-wing UAVs is more focused on the modeling of the flight dynamics [81–88], control [77, 89–93] and intelligent autonomous flight tasks such as vision based tracking and fully autonomous indoor flight.

There are numerous control algorithm studies both to improve stability and maneuverability in all flight conditions and to improve autonomy through obviating sensor errors using sensor fusion. There have been efforts to add robustness against wind gusts using hierarchical back-stepping control and high-gain unknown input observer for disturbance estimation [94], and to improve stability using inertial measurement based Artificial Neural Network (ANN) [95], model-independent PD controller, and quaternion based PD^2 control with Coriolis force and gyroscopic torque compensation [76].

Full autonomous flight of rotary-wing UAVs is very vulnerable to sensor measurement errors, especially to the position and orientation measurement errors and small rotary wing UAVs generally use low cost sensors which can produce relatively high measurement errors. For this reason, there is still significant research on improving measurement qualities of the onboard sensors. There are studies on fusion algorithms between the data of gyroscopes and delayed orientation data from an off-board vision system [96], gyroscopes and accelerometers [97], gyroscopes and inclinometers [98], INS and stereo vision [95], GPS and INS [99–101], and optical flow sensor and GPS [80] to obviate the drift and measurement nonlinearities of one sensor utilizing another sensor’s data and studies to substitute some sensors with state observers [23].

There are also studies on intelligent autonomous flight tasks such as vision based tracking of a shape on the ground [102–107], vision based landing on a predefined stationary or moving target [108–115], vision based scanning of areas to identify injured people on the ground [116], vision based detection of places in hazardous terrain available for landing [117–120], and even vision based photogrammetry [121].

Various methods are applied for the path tracking ranging from linear SISO and PD control [85–87] to non-linear ones like back-stepping, H_∞ loop shaping, state dependent Riccati equation, neural-network based controls [88, 122–129]. There is even a new model and control attempt for an eight-rotor helicopter [130, 131], which has additional motors to separate the controls of each DOF. There are also efforts for mono-camera vision-based path tracking [15, 16, 132, 133] and stereo vision-based path tracking for more precise localization.

Research on UAVs other than the fixed-wing and rotary-wing vehicles has a wide-spread spectrum of designs. These UAVs are relatively new designs and are focused on combining vertical takeoff, landing and flight capabilities of rotary-wing vehicles with long range, high speed flight capabilities of fixed-wing vehicles [134]. The common strategy of this type of UAVs for combining these two separate flight types is operating motors vertically to use motor thrust as a lift source in vertical flight and operating motors as forward propulsion sources and wings as lift sources in horizontal flight. This strategy generally adds some mechanical complexity and control problems especially in transition between two flight modes, but combining these two flight modes is considerably useful, so these features are worth to the encountered problems. Some examples for this group of UAVs are given in Table

1.3.

Table 1.3: Examples of other than Fixed-Wing and Rotary-Wing UAVs

Category	Model	
Tilt-rotor	Bell Eagle Eye	
	Smart UAV of KARI	
	AVT Hammerhead	
Tail-sitter	AeroVironment SkyTote	
	Aurora Flight Sciences Goldeneye 80	
	T-Wing of University of Sydney	
Tilt-wing	HARVee of Arizona State University	
	QTW of Chiba University and G.H. Craft	
	Tilt-wing UAV of Universita di Bologna	

As seen in the table, some of these air vehicles are tilt rotors that only tilt the rotors for flight mode conversion, such as Bell Eagle Eye [135], Smart UAV of KARI [136], BIROTAN [137] and AVT Hammerhead, tail-sitters that takeoff and land pointing upwards and fly pointing forwards such as AeroVironment SkyTote, Aurora Flight Sciences Goldeneye 80 [30], T-Wing and Vertigo of University of Sydney [138–140], canard rotor wings that stop and fix the helicopter main rotor as a wing beyond sufficient horizontal flight

speed such as Boeing X-50 Dragonfly [66], and tilt-wings that tilt the wing-rotor groups for flight mode conversion, such as HARVee of Arizona State University [141], and QTW of Chiba University and G.H. Craft [34, 142]. There are also some examples of morphing wing UAVs that are not intended for vertical flight, instead are intended for optimizing the wings to a broad range of flight speeds and altitudes such as Lockheed Martin Cormorant with folding wings, NextGen Aeronautics MFX-1,MFX-2 with sweep changing wings, ILC Dover Apterion with inflatable wings [27].

1.2 Motivation

The development of UAVs is an exciting topic for research. It is both a very critical topic for national security and independence on this key technology and an area that has the potential to grow to very far extends in terms of market and technological jumps. Additionally, research on this topic leads to research on the operation, problems and solutions to the problems of various sensors, digital circuits, advanced control systems, vision based control approaches, codes in real-time systems, power sources, actuators, system integration, high technology materials with high endurance and low weight, aerodynamics and optimization. Even though it is difficult to handle all these aspects, study on this topic is a research on the entire focus of mechatronics.

In this thesis, the aim is to design, produce and fly an electric powered VTOL (Vertical Takeoff and Landing) UAV, that has high speed and long endurance capabilities. There have been several designs that could be implemented, some of them being fixed-wing with an additional vertical rotor for vertical flight, dual or quad tilt-rotor, tail-sitter and dual or quad tilt-wing.

Fixed-wing UAV with an additional vertical rotor has the advantage of

being a well-known airplane structure, however it requires a complex contra-rotating vertical rotor mechanism with cyclic control on the rotors for stable vertical flight. This design would not support a reasonable amount of batteries to be carried for reasonable flight durations. Dual tilt-rotor and tilt-wing would again require cyclic control on the rotors, which is a mechanically complex system and requires very long diameter propellers to carry reasonable amount of batteries. Tail-sitter has been a good choice due to its simplicity, however its body rotates for the transition and the image captured by the surveillance camera is affected from these motions.

The decision between quad tilt-rotor and quad tilt-wing is given in the favor of quad tilt-wing since the air flow produced by the rotors is blocked at a minimum level in tilt-wing structure. Quad tilt-wing also has the advantage of being a quad-rotor that does not require any cyclic control on the propellers, which makes it mechanically simple and reliable. Additionally, the body does not undergo rotations for the transition between the modes, which makes it appropriate for surveillance through a camera on the body.

Even though, quad tilt-wing UAV with the performance goals determined in this project is very challenging both in terms of design and control. Designing the body lightweight and stiff at the same time with the additional rotating mechanisms for the wings is very challenging. Determination of the type of the motors, propellers and batteries is another severe challenge. Since fixed-pitch propellers are used in both hovering at zero flight speed and at high speeds, and since the system needs to be somehow optimal in the entire speed range, motor propeller couples need to be investigated thoroughly. To meet the design weight specifications, Li-Po batteries are chosen among a variety of them to find the lowest weight/capacity battery type that is also

capable of flying this UAV.

Furthermore, designing the flight control electronics and its software, integrating it with the sensors, actuators and high level control computer in the supervisory control system, and developing the control methodology for achieving stable flight on a flight mode switching UAV is a challenge by itself. The model of the system and consequently the response of the system to the control efforts changes as the UAV changes its wing angles and horizontal speed and these changes are quite difficult to predict without experimental data acquired from the wind tunnel tests. As a result, the control variables keep up with the air speed of the UAV for stable and smooth flight in the entire speed range.

1.3 Thesis Organization and Contributions

In Chapter 2, the aerodynamic design and the result of wind tunnel tests are presented. The aerodynamic design is carried out to maximize the aerodynamic efficiency and determine safe flight characteristic of this new type of air vehicle. The propulsion system components and the power source are selected for low current consumption in the entire horizontal speed range and long flight duration. Also, the aerodynamic design of SUAVI is performed utilizing *Motocalc*[®] and NASA *FoilSim*[®] II, and running a series of *ANSYS*[®] CFD simulations.

In the wind tunnel tests, first, tests on one wing of SUAVI are conducted to verify results obtained in the tests by comparing with the ones existing in the literature. Additionally, the winglet design is optimized testing several shapes and sizes. After obtaining the optimal design for the winglet, nominal flight and pitching flight tests are conducted to obtain tabular data on the

wing angle of attacks and motor driver PWMs for both nominal flight and flight with nominal values except the pitching moment. These tests are repeated for 0-17 m/s air speeds.

In Chapter 3, the mechanical system design and the prototyping of SUAVI are detailed. In the mechanical system design, the material to be used in the prototype is determined and tested by carrying out mechanical tests in Universal Testing Machine. Also, the design is conducted taking the weight and strength requirements into account, and the placement of the parts are decided based on their functions in the air vehicle and their weights affecting the inertia and stability characteristics of SUAVI. The first prototype is produced, and after several flight tests, the mechanical system design is revised for better mechanical properties and increased utility. Also, the second prototype is produced for the usage in flight tests.

In Chapter 4, a dynamical model of the system is obtained using Newton-Euler formulation. A supervisory control system is designed with the high-level and low-level controllers. GPS based hovering and GPS based waypoint navigation are also considered along with low-level attitude and altitude controllers.

In Chapter 5, the design and production of low-level control circuit, its integration with the sensors and actuators, filters and sensor fusion algorithm used to obtain reliable orientation estimates are detailed. The overall flight control system is also discussed.

In Chapter 6, the flight tests of SUAVI with robust hover, vertical takeoff and landing, and horizontal flight are demonstrated. The performance of the SUAVI in these tests is evaluated.

Finally, in Chapter 7, the thesis is concluded with several remarks and

the future directions are indicated.

The contributions of the thesis can be summarized as follows:

- The conceptual design of a novel quad tilt-wing unmanned aerial vehicle (SUAVI: Sabancı University Unmanned Aerial VehIcle) is carried out taking the flight duration, flight speed, size, power source and missions to be achieved into account.
- The actuation system (motor, motor speed controller and propeller set) is determined to find the most optimal choice in the entire speed range, from hovering at zero flight speed up to the highest planned flight speed.
- The aerodynamic design is carried out to maximize the aerodynamic efficiency and to determine safe flight characteristics.
- The mechanical design of SUAVI is conducted to satisfy criteria such as strength, lightness and conformity to the missions to be realized.
- SUAVI is prototyped using carbon composite material.
- A half-body prototype of SUAVI is designed and produced for wind tunnel tests to determine SUAVI's aerodynamic characteristics.
- A full non-linear dynamical model which includes aerodynamic disturbances is obtained using Newton-Euler formulation.
- A supervisory control architecture is implemented on SUAVI, where a Gumstix microcomputer behaves as a supervisor which orchestrates switching of low-level controllers into the system. Supervisory control

is responsible for decision making, monitoring states of the vehicle and safety checks during the flight.

- The high-level controller generates attitude references for the low-level controllers using GPS data.
- PID controllers are implemented for both high-level and low-level control systems.
- A disturbance observer is utilized to estimate and compensate for the external disturbances acting on SUAVI.
- Various analog and digital filters are implemented to smooth out noisy sensor measurements.
- Extended Kalman filter is utilized to obtain reliable orientation information by fusing data from low-cost MEMS inertial sensors such as gyros, accelerometers and the compass.
- Real-time control software is developed for the whole flight control system.
- SUAVI can operate in a semi-autonomous flight mode by communicating with the ground station.
- A quadrotor test platform (SUQUAD: Sabanci University QUADrotor) is produced and used for the initial performance tests of the flight control system.
- Performance of the flight control system is verified by numerous simulations and real flight experiments. VTOL and horizontal flights are successfully realized.

1.4 Notes

This Ph.D. thesis work is carried out in the context of the TÜBİTAK (The Scientific & Technological Research Council of Turkey) project “Mechanical Design, Prototyping and Flight Control of an Unmanned Autonomous Aerial Vehicle” under the grant number 107M179. Five progress reports have been submitted to TÜBİTAK and all of them are evaluated as being successful. The project is in its final stage.

1.4.1 Journal Papers

- Design and Development of a Tilt-Wing UAV, **E. Cetinsoy**, E. Sirmoglu, K. T. Oner, C. Hancer, M. Unel, M. F. Aksit, İ. Kandemir, K. Gulez, *Turkish Journal of Electrical Engineering and Computer Sciences*, (forthcoming), 2011.
- Mathematical Modeling and Vertical Flight Control of a Tilt-Wing UAV, K. T. Oner, **E. Cetinsoy**, E. Sirmoglu, C. Hancer, M. Unel, M. F. Aksit, K. Gulez, İ. Kandemir, *Turkish Journal of Electrical Engineering and Computer Sciences*, (forthcoming), 2011.
- Aerodynamic Characterization of a Quad Tilt-Wing UAV via Wind Tunnel Tests (to be submitted)
- Mechanical and Aerodynamic Design of a Quad Tilt-Wing UAV (to be submitted)
- Hierarchical Control of a Quad Tilt-Wing UAV (to be submitted)

1.4.2 Published Conference Papers

- Robust Position Control of a Tilt-Wing Quadrotor, Cevdet Hancer, Kaan Oner, Efe Sirimoglu, **Ertugrul Cetinsoy**, Mustafa Unel, *49th IEEE Conference on Decision and Control*, Atlanta, GA, December 15-17, 2010.
- Robust Hovering Control of a Quad Tilt-Wing UAV, Cevdet Hancer, Kaan T. Oner, Efe Sirimoglu, **Ertugrul Cetinsoy**, Mustafa Unel, *36th Annual Conference of the IEEE Industrial Electronics Society (IECON-2010)*, Phoenix, Arizona, USA from November 7-10, 2010.
- Döner Kanatlı Quadrotorun Havada Asılı Kalmasını Sağlayan Gürbüz Pozisyon Denetleyici Tasarımı, C. Hançer, K. T. Öner, E. Sırımoglu, **E. Çetinsoy**, M. Ünel, *TOK'10: Otomatik Kontrol Ulusal Toplantısı*, İstanbul, September 21-23, 2010.
- LQR and SMC Stabilization of a New Unmanned Aerial Vehicle, K. T. Oner, **E. Cetinsoy**, E. Sirimoglu, C. Hancer, T. Ayken, M. Unel, *Proceedings of International Conference on Intelligent Control, Robotics, and Automation (ICICRA 2009)*, Venice, Italy, October 28-30, 2009.
- Döner-Kanat Mekanizmasına Sahip Yeni Bir İnsansız Hava Aracının (SUAVİ) Modellenmesi ve Kontrolü, K. T. Öner, **E. Çetinsoy**, E. Sırımoglu, T. Ayken, M. Ünel, M. F. Akşit, İ. Kandemir, K. Gülez, *TOK'09: Otomatik Kontrol Ulusal Toplantısı*, İstanbul, October 13-16, 2009.
- Yeni Bir İnsansız Hava Aracının (SUAVİ) Prototip Üretimi ve Algılayıcı-Eyleyici Entegrasyonu, **E. Çetinsoy**, E. Sırımoglu, K. T. Öner, T.

- Ayken, C. Hançer, M. Ünel, M. F. Akşit, İ. Kandemir, K. Gülez, *TOK'09: Otomatik Kontrol Ulusal Toplantısı*, İstanbul, October 13-16, 2009. (Best paper award)
- Dynamic Model and Control of a New Quadrotor Unmanned Aerial Vehicle with Tilt-Wing Mechanism, K. T. Oner, **E. Cetinsoy**, M. Unel, M. F. Akşit, I. Kandemir, K. Gulez, *Proceedings of International Conference on Control, Automation, Robotics and Vision (ICCARV'08)*, Paris, France, November 21-23, 2008.
 - İnsansız Hava Araçları için Test Düzenegi Tasarımı ve Üretimi, A. Eray Baran, Cevdet Hançer, Egemen Çalıkoglu, Emre Duman, **Ertugrul Cetinsoy**, Mustafa Ünel, Mahmut F. Akşit, *TOK'08: Otomatik Kontrol Ulusal Toplantısı*, İstanbul, November 13-15, 2008.
 - Yeni Bir İnsansız Hava Aracının (SUAVİ) Dikey Uçuş Kipi İçin Dinamik Modeli ve Yörünge Kontrolü, Kaan Taha Öner, **Ertugrul Cetinsoy**, Mustafa Ünel, İlyas Kandemir, M. F. Akşit, K. Gülez6, *TOK'08: Otomatik Kontrol Ulusal Toplantısı*, İstanbul, November 13-15, 2008.
 - Yeni Bir İnsansız Hava Aracının (SUAVİ) Mekanik ve Aerodinamik Tasarımı, **Ertugrul Cetinsoy**, Kaan T. Öner, İlyas Kandemir, Mahmut F. Akşit, Mustafa Ünel, Kayhan Gülez, *TOK'08: Otomatik Kontrol Ulusal Toplantısı*, İstanbul, November 13-15, 2008.

1.5 Nomenclature

Symbol	Description
a	total acceleration of the aerial vehicle
a_i	amplitude of the sinusoids in wind model
a_x	x component of the reference acceleration vector
a_y	y component of the reference acceleration vector
a_z	acceleration of the aerial vehicle along z axis
a_{xy}	reference acceleration vector
A	area of the wing
A_k	state transition matrix
b_g	bias in gyros
c_D	drag coefficient
c_L	lift coefficient
$C(\zeta)$	Coriolis-centripetal matrix
$D(\zeta, \xi)$	external disturbance vector
\dot{e}_{at}	along track error rate
e_{ct}	cross track error
\dot{e}_{ct}	derivative of cross track error
e_x	position error of the aerial vehicle along x axis
\dot{e}_x	derivative of position error along x axis
e_y	position error of the aerial vehicle along y axis
\dot{e}_y	derivative of position error along y axis
E	rotational velocity transformation matrix
$E(\xi)w^2$	system actuator vector
F_d	forces due to external disturbances
F_D	drag forces
F_g	gravity force
F_L	lift forces
F_t	total external force acting on the aerial vehicle
F_{th}	thrust force created by rotors
F_w	aerodynamic forces generated by the wings

Symbol	Description
G	gravity matrix
H_k	observation matrix
I_b	inertia matrix of the aerial vehicle in body fixed frame
I_{xx}	moment of inertia around x_b in body frame
I_{yy}	moment of inertia around y_b in body frame
I_{zz}	moment of inertia around z_b in body frame
J	Jacobian transformation between generalized vectors
J_{prop}	inertia of the propellers about their rotation axis
K_k	Kalman gain
K_{atp}	proportional gain for along track controller
K_{ati}	integral gain for along track controller
K_{ctp}	proportional gain for cross track controller
K_{ctd}	derivative gain for cross track controller
K_{cti}	integral gain for cross track controller
$K_{x,p}$	proportional gain for controller along x axis
$K_{x,d}$	derivative gain for controller along x axis
$K_{x,i}$	integral gain for controller along x axis
$K_{y,p}$	proportional gain for controller along y axis
$K_{y,d}$	derivative gain for controller along y axis
$K_{y,i}$	integral gain for controller along y axis
l_l	rotor distance to center of gravity along x_b in body frame
l_s	rotor distance to center of gravity along y_b in body frame
L_h	horizontal gust length scale
L_v	vertical gust length scale
m	mass of the aerial vehicle
M	inertia matrix
M_d	torques due to external disturbances
M_{gyro}	gyroscopic torques
M_{nom}	nominal inertia matrix
M_t	total torque acting on the aerial vehicle
M_{th}	rotor torques

Symbol	Description
M_w	aerodynamic torques due to lift/drag forces
\tilde{M}	difference between actual and nominal inertia matrices
n_i	unit normal vector perpendicular to path P
O_b	origin of body fixed frame
O_w	origin of inertial (world) frame
$O(\zeta)_w$	gyroscopic matrix
p	angular velocity of the aerial vehicle along x_b in body frame
P	reference path generated by waypoints
P_w	position of the aerial vehicle in inertial (world) frame
\dot{P}_w	linear velocity of the aerial vehicle in inertial (world) frame
$P_{k k-1}$	a priori error covariance matrix
$P_{k k}$	a posteriori error covariance matrix
q	angular velocity of the aerial vehicle along y_b in body frame
Q	process covariance matrix
r	angular velocity of the aerial vehicle along z_b in body frame
R	measurement covariance matrix
R_x	elementary rotation around x axis
R_y	elementary rotation around y axis
R_z	elementary rotation around z axis
R_{wb}	orientation of body frame wrt. the world frame
R_{bw}	orientation of world frame wrt. the earth frame
S_t	exponentially weighted moving average filtered sonar measurement at time t
S_{t-1}	exponentially weighted moving average filtered sonar measurement at time t-1
t_i	unit tangent vector along path P
T	sampling time
u_i	virtual control inputs
u^H	high-level input signal
u^L	low-level input signal
v_w	time dependent estimate of wind vector
v_w^0	static wind vector
v_x	linear velocity along x_b in body fixed frame

Symbol	Description
v_y	linear velocity along y_b in body fixed frame
v_z	linear velocity along z_b in body fixed frame
v_α	airstream velocity
V_w	linear velocity of the aerial vehicle in inertial (world) frame
V_b	linear velocity of the aerial vehicle in body fixed frame
w_i	propellers rotational speed
x_b	x axis of body fixed frame
x^d	desired reference position
x_i^d	waypoints of the path P
x_k	state of the system
$\hat{x}_{k k-1}$	a priori state estimate
$\hat{x}_{k k}$	a posteriori state estimate
x_n	unit vector along x_w in inertial (world) frame
$x(t)$	instantaneous position of aerial vehicle provided by GPS
x_w	x axis of inertial (world) frame
X	position of the aerial vehicle along x_w in inertial (world) frame
\dot{X}	linear velocity of the aerial vehicle along x_w in inertial (world) frame
y_b	y axis of body fixed frame
y^H	high-level output signal
y^L	low-level output signal
y_n	unit vector along y_w in inertial (world) frame
y_w	y axis of inertial (world) frame
Y	position of the aerial vehicle along y_w in inertial (world) frame
\dot{Y}	linear velocity of the aerial vehicle along y_w in inertial (world) frame
Y_{t-1}	raw sonar measurement at time (t-1)
z_b	z axis of body fixed frame
z^d	desired reference altitude
z_w	z axis of inertial (world) frame
Z	position of the aerial vehicle along z_w in inertial (world) frame
\dot{Z}	linear velocity of the aerial vehicle along z_w in inertial (world) frame
α	weighting scale in exponentially weighted moving average filter

Symbol	Description
α_w	attitude of the aerial vehicle in inertial (world) frame
α_i	effective angle of attack
$\dot{\alpha}_w$	time derivative of attitude in inertial (world) frame
β	weighting parameter
ΔS	difference between two consecutive sensor readings in exponentially weighted moving average filter
Ω_b	angular velocity of the aerial vehicle in body fixed frame
Ω_i	randomly selected frequency in wind model
Ω_w	time derivative of attitude in inertial (world) frame
ϕ	roll angle, angular position around x_w
ϕ_{ref}	reference roll angle
θ	pitch angle, angular position around y_w
θ_{ref}	reference pitch angle
ψ	yaw angle, angular position around z_w
$\dot{\phi}$	time derivative of angular position around x_w
$\dot{\theta}$	time derivative of angular position around y_w
$\dot{\psi}$	time derivative of angular position around z_w
θ_i	angle of attack for each wing
ρ	air density
λ_i	torque/force ratio
ζ	generalized velocity vector of the aerial vehicle
ξ	position and orientation of the aerial vehicle in inertial (world) frame
φ_i	phase shift in wind model
$\Phi_h(\Omega)$	power spectral density for horizontal winds
$\Phi_v(\Omega)$	power spectral density for vertical winds
σ_h	horizontal turbulence intensity
σ_v	vertical turbulence intensity
η_k	process noise
ν_k	measurement noise
τ_{dist}	total disturbance
$\hat{\tau}_{dist}$	estimated disturbance

Chapter 2

2 Aerodynamic Design and Wind Tunnel Tests

The design of SUAVI is shaped based on the tasks that it will perform. It is designed as a compact electric powered air vehicle for both outdoor and indoor applications. It has four tilting wings with the motors mounted on the mid-span leading edge of the wings. Thus, the wings occlude the rotor slipstream at the minimum level all the time. The wings are in vertical position during hovering, and vertical takeoff and landing. In this configuration, the rotors produce vertical thrust and steady flight is established using the control on thrusts generated by RPM control of constant pitch propellers. When forward motion is required, the wing angle of attacks are reduced based on the speed requirement and rotor thrusts are adjusted accordingly.

2.1 Aerodynamic Design

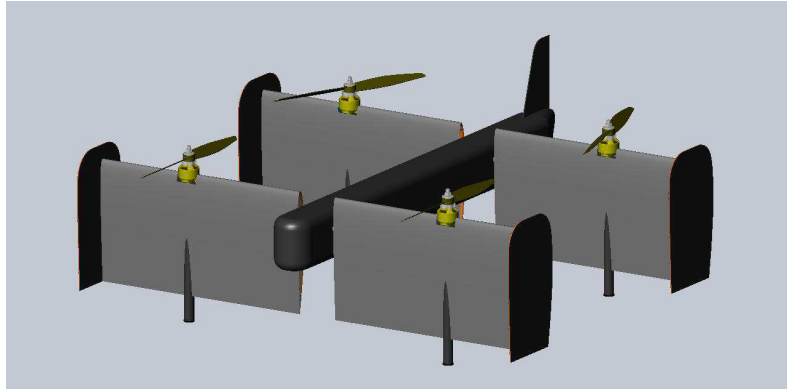
The aerodynamic design of SUAVI is made based on the operational requirements. The aircraft is aimed to operate in surveillance missions such as traffic control, security checks, and disasters including indoor-outdoor fires, floods, earthquakes. To satisfy the needs of these tasks, it is planned to take-off and land vertically, hover and fly in an airspeed range of 0-60 km/h both for stationary and in-motion surveillance.

It is also aimed to be compact for indoor surveillance and mechanically simple for operational reliability. To meet such flight capabilities with these features, SUAVI is designed as a quad tilt-wing air vehicle on which all four motors are mounted on the mid-span leading-edges of the wings and the wings are tilted in horizontal-vertical position range (Fig. 2.1).

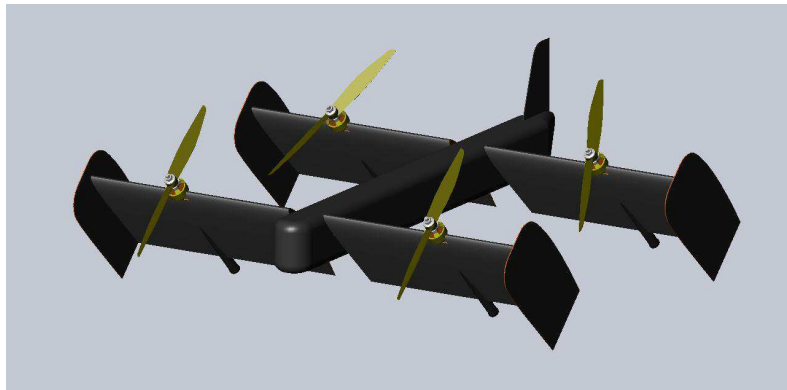
Motors rotate constant pitch propellers for mechanical simplicity, altering thrust through RPM change. In this design, wings are tilted to vertical position to form a quad-rotor helicopter using only motor thrusts for lift on vertical takeoff, landing and hovering.

When horizontal flight is required, wings are tilted gradually to the appropriate angles of the desired speed and motor thrusts are adjusted accordingly. At high speeds, wings are tilted to nearly-horizontal position to generate lift and motors generate forward thrust, forming a four motor tandem wing airplane. The design length and wingspan of the aircraft are both 1 m and the design weight is 4.5 kg.

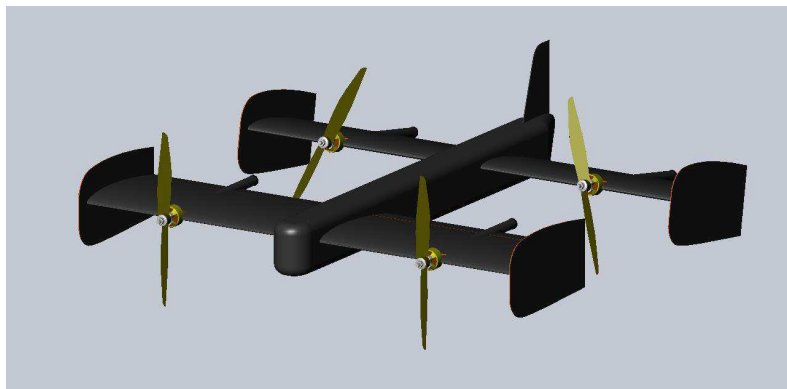
The energy source for the propulsion is determined as electric since electric motors do not produce any poisonous gases enabling indoor flight, are quieter, more reliable, easier to adapt to computerized control system and more responsive to instant control requirements for constant pitch propeller utilization. The vertical flight endurance of SUAVI is planned to reach half hour whereas its horizontal flight endurance is to exceed one hour. To satisfy such a demand using electric power, it is necessary both to have an energy-efficient propulsion system with high capacity Li-Po batteries and a body shape that is aerodynamically optimized for the task.



(a)



(b)



(c)

Figure 2.1: CAD model of SUAVI in vertical (a), transition (b) and horizontal (c) flight modes

2.1.1 Propulsion System Design

To have an energy-efficient propulsion system for long time endurance of SUAVI, motor-propeller couples are chosen to have high efficiencies in both static and dynamic thrust generations in the desired flight speed range.

First, the performances of the electric motor, motor drivers and propellers are investigated both comparing the technical features of these systems through the catalogs and using the MotoCalc program. Motocalc is both a database of electric propulsion equipment and an accurate suggestion software for electric powered radio controlled (RC) airplanes. This program has the additional feature of simulating the conditions with selected motor, motor driver, battery, propeller, transmission, air pressure and air temperature and delivering the air speed, current, voltage, output power, thrust, motor RPM, the relative speed of the slipstream of the propeller wrt. the airplane and efficiency of the system for various throttle settings.

In the selection of the motor type, the important criteria are decided as producing the required thrusts in both vertical and horizontal flights of the SUAVI drawing the least possible current, being durable in mechanical aspects lightweight, and having large air passages for effective cooling in every whether condition during the flight. The motors need to be capable of rotating the propellers at high RPMs to produce sufficient thrust at the highest target speed during the horizontal flight, so they need to have high output power. They are also to produce maximum thrust with some excess on $\frac{4.5}{4}(\frac{kg}{motor}) \times \sqrt{2} = 1.59 \frac{kg}{motor}$ to be able to carry SUAVI even without contribution of the wing lifts at 45° angle of attack. In this formula, $\sqrt{2}$ is the factor that converts the required vertical force component to the required motor thrust force that is inclined at an angle of 45° wrt. the horizontal.

The lift of the wings with commonly applied airfoil shapes begin to decrease beyond 15° angle of attack due to the separation, however it usually decreases up to 40-50 % at 45° angle of attack, depending on the preferred airfoil type [143]. When a motor with that amount of power is chosen, there is still excess power safe enough for stabilizing the UAV, which is inevitably required. Durability is a combined result of simplicity and high-quality manufacturing. To satisfy the durability requirement in an RC hobby type motor, direct drive motor with a quality brand is the most reasonable choice, which also increases the transmission efficiency.

Lightness is also an important issue that can be solved by reduction of the size and usage of lightweight materials. As a consequence of investigations done both in Motocalc and catalogs, Great Planes Rimfire 42-40-800 is chosen among a variety of RC aircraft electric motors, since it is a high efficiency direct drive brushless motor with strong Neodymium magnets and large hub diameter enabling high torque generation with relatively low current requirement. It has large cooling holes for effective cooling in long duration flights, and considerably low weight due to its aluminum body.

As a result of the high torque, this motor can utilize large diameter propellers increasing the propeller efficiency in the desired flight speed range. For controlling the motor speeds, Great Planes Electrify Silver Series 35 motor driver is preferred, which is capable of delivering up to 35 A continuously, which is already higher than the 32 A maximum allowed current of the chosen motor.

To determine the propeller type to be used on SUAVI, first a thrust test bench is designed and produced (Fig. 2.2). This thrust test bench is a system with a pivoted arm that is connected to the motor on one end and to a load

cell on the other end, both staying perpendicular to the arm. The motor shaft axis is perpendicular to the ground to be able to test the motor thrust both without any obstacle at back as in the horizontal flight and with an obstacle like ground as in the vertical flight especially at low altitudes.

The motor on the test bench can be powered both by a switching power supply with high current capability for motor thrust tests and by batteries for collecting data on the battery performance on the propulsion system. The motor power reference pulses are generated by an electric circuit with a microcontroller, that is also designed and produced in the project.



Figure 2.2: The motor test bench

For the decision on the propeller type to be used on SUAVI, a variety of APC electric motor propellers from size $11'' \times 8''$ to $16'' \times 5''$ (former number: diameter in inch, latter number: pitch in inch) are tested on the thrust test bench with the selected motor. This size range for the propellers is determined based on the suggested propeller size range in the technical specs of the motor and the simulations conducted in Motocalc.

For high static thrust efficiency at vertical flight large diameter low pitch propeller is preferred, whereas high pitch propeller or very high motor speed is required to generate sufficient thrust at high speeds. Since constant pitch

propellers are utilized, the propellers are selected among moderate pitch values. The motor-propeller couples are tested for maximum thrust (Table 2.1) and current for nominal thrust per motor during hover (Table 2.2). These tests are conducted using both 11.1 V and 14.8 V input voltages, which are the standard voltages of 3-cell and 4-cell in series Li-Po batteries, to determine which battery voltage is more preferable for powering the system.

Table 2.1: Maximum thrust test results

Prop size	11.1 V				14.8 V			
	Current (A)	Thrust (g)	Thrust/current (g/A)	Power (W)	Current (A)	Thrust (g)	Thrust/current (g/A)	Power (W)
11" × 8"	25.3	1260	49.8	280.8	32.0	1735	54.2	473.6
12" × 8"	31.5	1577	50.1	349.6	32.0	1860	58.1	473.6
13" × 6.5"	32.0	1812	56.6	355.2	32.0	2130	66.6	473.6
13" × 8"	32.0	1690	52.8	355.2	32.0	1955	61.1	473.6
14" × 7"	32.0	1876	58.6	355.2	32.0	2157	67.4	473.6
14" × 8.5"	32.0	1728	54.0	355.2	32.0	1964	61.4	473.6

As a result of these tests, the appropriate propeller size is chosen as 14" × 7", which is a moderate pitch propeller size, due to its superior performance compared with other sizes. The second best propeller with size of 13" × 6.5" has 4-5 % less performance in terms of maximum thrust and current consumption. Likewise, when the maximum speed potentials of these two propeller sizes are investigated in Motocalc, it is observed that 14" × 7" propeller is sufficient to deliver 221 g thrust per motor even at 70 km/h airspeed, while 13" × 6.5" propeller suffices to deliver nearly the same amount

Table 2.2: Thrust test results for nominal hover flight thrust

Prop size	11.1 V			14.8 V			Saving (%)
	Current (A)	Thrust/current (g/A)	Power (W)	Current (A)	Thrust/current (g/A)	Power (W)	
11" × 8"	21.4	52.6	237.5	16.2	69.4	239.8	1
12" × 8"	18.4	61.1	204.2	13.9	80.9	205.7	1
13" × 6.5"	14.6	77.0	162.0	11.4	98.7	168.7	4
13" × 8"	16.3	69.0	180.9	12.5	90.0	185.0	3
14" × 7"	13.9	80.9	154.3	10.8	104.2	160.0	4
14" × 8.5"	15.6	72.1	173.2	11.8	95.3	174.6	1

of thrust at 60 km/h.

For yaw balance in flight with high angle of attacks, both clockwise and counter-clockwise propellers with the selected size are coupled with motors. This also enables the control of yaw in vertical flight mode through motor RPM differentiation between clockwise and counter-clockwise rotating propellers. Additionally, the tests with these two input voltages revealed that using 11.1 V input voltage results in 4 % less power consumption from the batteries for the same thrust values.

Usage of 11.1 V is definitely more preferable also for the supply of the control system. The control system exploits additional energy from the same battery group and generally the components use either 3.3 V or 5 V. These low voltages are obtained through the linear regulators on the control system, which simply lower the voltages by converting the unneeded amount of voltage to heat and exhausting it to air. Even if the control system used only 5 V, with a current draw of 1 A by the control system, the heat generated on the voltage regulators would increase from 6.1 W to 9.8 W. This would

require larger and heavier heat sinks in the fuselage.

Consequently, 11.1 V is determined as the operating voltage for the motors, so 3-cell in series Li-Po batteries are used for energy storage. With this voltage, motor and propeller size combination, the static thrust for nominal vertical flight is generated through the consumption of 13.9 A current. This means that hypothetically $(13.9 \text{ A} \times 4) \times 0.5 \text{ h} = 27.8 \text{ Ah}$ battery capacity is enough to hover SUAVI for half hour.

However, due to the fact that battery voltage becomes less as its capacity is exploited, the current requirement increases slightly as time passes. The voltage drop profile is dependent on several factors like quality, age, inner impedance of the battery and even the humidity and temperature of the air. Due to the weight constraints for the batteries in SUAVI, a total of 30 Ah 11.1 V Li-Po battery could be integrated in the system, which constitutes nearly 2.4 kg (53 %) of the total flight weight. Though, 26 minute long vertical only flight with excess battery charge after the landing is successfully achieved. 30 minutes could also be tested, but this has not been the focus on the project at that level.

Utilizing the experimental data obtained from the motor performance tests, the generally observed linear relationship between the thrust and square of propeller angular velocity (ω^2) is verified (Fig. 2.3). This is especially important for the modeling of the system and implementation of model based control for flight.

2.1.2 Aerodynamic Design

Aerodynamic optimization of SUAVI begins with the decision that it is an unmanned aerial vehicle with four wings, two of them placed at front

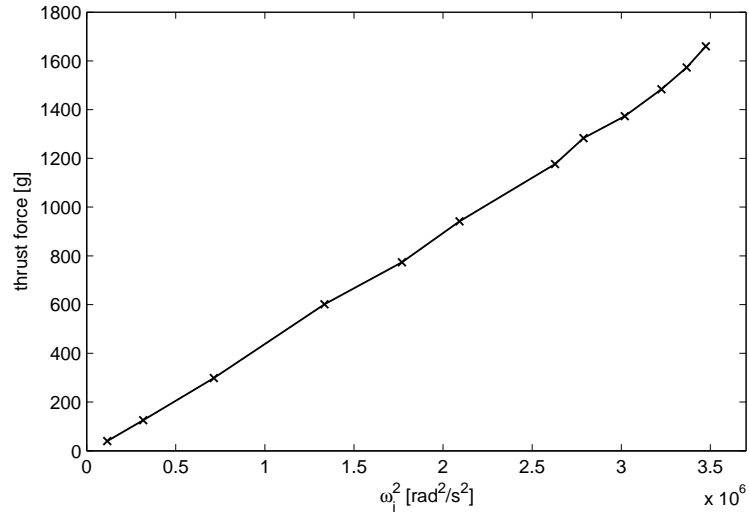


Figure 2.3: Relationship between the thrust and square of angular velocity for 14x7 propeller

and two of them placed at rear side of the fuselage. The aim of the aerodynamic optimization is to minimize air drag while generating sufficient lift for flight and achieving this goal with the least complicated and most lightweight structure.

The aerodynamic design of the fuselage is focused on reducing the drag coefficient (C_D) of the fuselage, improving the aerodynamic interaction between the fuselage and the wings, and reducing the cross section.

The fuselage is designed as a rectangular prism with rounded nose section and a back section with gradually decreasing thickness for high aerodynamic efficiency. When looked from the top of the air vehicle, the fuselage resembles a symmetrical wing with long straight sides (Fig. 2.4 a). This shape has two main aerodynamic advantages. The first one is the low drag coefficient due to this shapes resemblance to water drop, that reduces the turbulence at the front and the back.

The second one is the behavior of the straight sides as a flow boundary to prevent additional loss. The fuselage sides behave as spanwise air flow boundaries at wing roots for up to 20° angle of attack with the help of high placement of the wings. The straight sides extend from the leading edge of the front wing to the trailing edge of the rear wing at 0° angle of attack (Fig. 2.4 b).

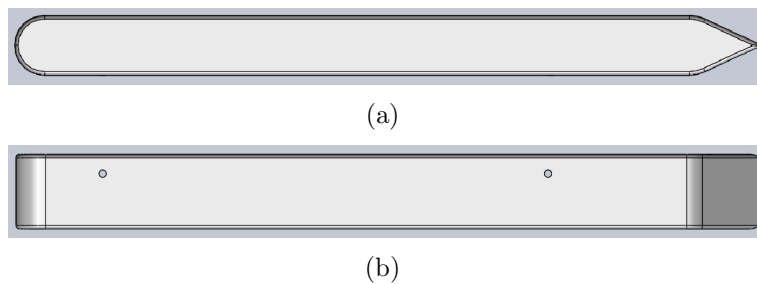


Figure 2.4: Top (a) and side (b) views of the fuselage

This prevents the rise of additional induced drag due to spanwise vortices on the wing roots. Additionally, the fuselage dimensions are chosen to be as small as possible, which is 8 cm wide and 10 cm high, that is just enough to make room for electronic control systems, onboard camera and the high torque wing tilting servo motors. There is also a vertical stabilizer at the back of the fuselage for yaw stabilization.

The shape of the wings is decided taking the speed range, wing span limitation and efficiency into consideration. First, the wing angle of attacks are planned to be 3° , which is the most efficient angle of attack for a wing in terms of lift to drag ratio [144], at the maximum target speed to make that speed easily reachable. Second, for deciding on the chord length, camber ratio and the thickness requirements of the airfoil, various airfoil simulations are run for a wide range of angle of attacks, flight speeds and atmospheric

conditions utilizing NASA Foilsim II and Motocalc's lift and drag coefficient estimator.

Consequently, an airfoil with 25 cm chord length, 12 % thickness and 4 % camber value, which resembles to NACA 4412 wing profile, is determined as a starting point of the wing design for the further simulations that are to be conducted in ANSYS environment. It is obvious that these results may most probably not reflect the final shape at all, since they are the considerations without the effect of additional air flow generated by the motors and are based on 2D wing model, that takes the advantage of the infinite wing assumption. However, there is always the problem of initial values to manipulate during the iterations, and this airfoil design has been a good starting point.

For the preliminary tests, a full scale wing with the determined airfoil shape is produced using carbon composite tubes and depron. An important experiment, in which the test wing is utilized, is the measurement of additional lift and the loss of the thrust due to the wing occlusion on the slipstream of the motor (Fig. 2.5).

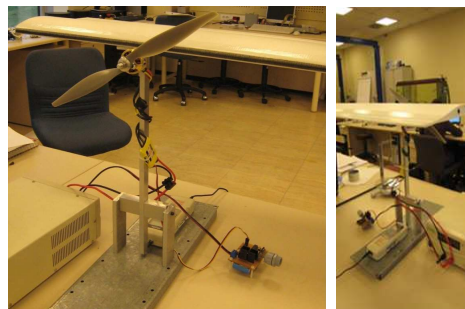


Figure 2.5: The test system for the effect of wing occlusion on the slipstream

This experiment is performed by adding a precision balance to measure the instant weight of the wing and measuring the motor current to produce the hovering nominal thrust (Table 2.3). Wing weight during the running

of the motor with several choices of both the propeller-leading edge distance and the spanwise distance of wing occlusion behind the propeller is also measured.

Table 2.3: Thrust test values for the effect of wing occlusion

Propeller-leading edge distance (cm)	Wing occlusion behind the propeller (cm)	Current for nominal vertical flight (A)
4	17.5	13.9
4	22.5	14.3
4	27.5	14.1
4	32.5	14.1
4	37.5	14.3
8	17.5	14.3
8	22.5	14.2
8	27.5	14.2
8	32.5	14.2
8	37.5	14.2

In Table 2.3, it is observed that occluding the propeller slipstream by the wing fully has a factor of at most 3 % on the motor current, which can be neglected when the benefit of delaying the air separation on the wing to far higher angle of attacks is taken into consideration.

It is also understood that setting the propeller-leading edge distance as 4 cm or 8 cm does not have a great effect on the performance. Hence, it is decided to keep this value as 4 cm to simplify the mechanical design and save some weight of the linkage parts between the motor and the wing. During these tests, it is also noted that the measurement of the wing weight is decreased for around 80 g when the motor runs, which means that the wings have some tendency to pull SUAVI backwards during hovering with a total of around 3.2 N.

To have a more complete insight on the lift and drag forces, torsion and bending moments generated by the wings, the performance of the vortex decreasing winglets at the wing tips and the effects of the consecutively running motors with contra rotation directions, and to find the optimum wing shape iteratively, ANSYS air flow simulations are also performed for various angle of attacks, throttle settings and wind speed. In these tests, the slipstream backward linear velocity and rotational velocity are taken from the the estimations of the Motocalc program, that has proven to have reasonably accurate estimations when compared with the thrust test bench measurements.

To conduct these simulations, the coordinate data of the airfoil shape are obtained from the *JavaFoil*[®] program (Fig. 2.6).

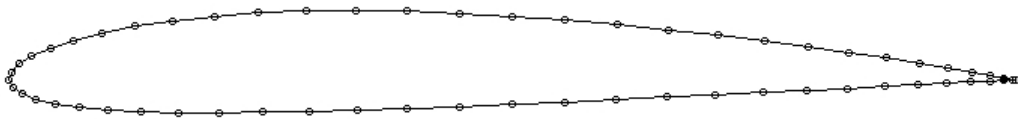


Figure 2.6: NACA 2410 wing profile

The wings with the determined chord length, wing span and shape, and the fuselage with a shape providing reasonable aerodynamic features, feasibility of production and sufficient room for the designed electronic control system and wing tilting mechanisms are drawn in *SolidWorks*[®] (Fig. 2.10). The 3D CAD model of SUAVI is imported into the ANSYS air flow simulation environment, an air flow closed volume is defined for the simulation and meshing is applied.

The boundaries for the simulation are defined as symmetry at the plane, which cuts the fuselage vertically into two equal parts, zero air speed on the surfaces of the UAV due to the stiction, tested air speed at the incoming

side of the closed volume and ambient air pressure at the outgoing side of the closed volume. Finally, the solver is run to obtain the results of the simulations.

As a consequence of all of these simulations, it is observed that using relatively long chord length with large winglet instead of high wing thickness is more preferable to increase efficiency. This is due to the facts that at high angle of attacks large chord length supplies large inclined surface against the air flow and at high speeds thicker wing causes more drag. In the literature, it is known that thinner and less cambered wings suffer from leading edge separation at lower angle of attacks, which causes stall [145]. However, wings of SUAVI are nearly fully submerged in the slipstream of the propellers and the high speed slipstream prevents the air separation even at high angle of attacks and supplies additional lift.

In the simulations, it is revealed that NACA 4412 airfoil generates more than necessary lift at the expense of additional drag due to the additional airspeed of 25-36 km/h on the wings caused by the propeller slipstreams. Hence, the simulations are repeated with NACA 2410 airfoil and this airfoil shape with 25 cm chord length is selected to be sufficient both for generating the required lift and for constraining the air drag at a considerable level (Fig. 2.7). This airfoil has a maximum camber line to mean line distance of 4 % of the chord length at a 40 % chord length distance behind the leading edge and a maximum thickness of 10 % chord length.

Due to the low aspect ratio ($AR=4$) and rectangular planform that minimizes wing loading through maximizing the area for the limited wing span, the wings of the air vehicle have tendency to have severe spanwise air flow, especially at high angle of attacks (Fig. 2.8).

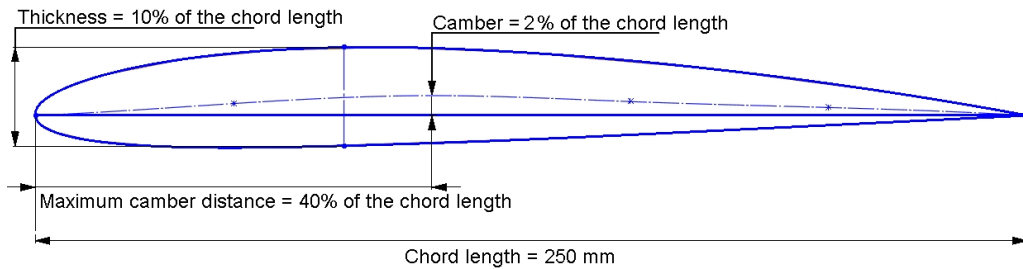


Figure 2.7: NACA 2410 airfoil

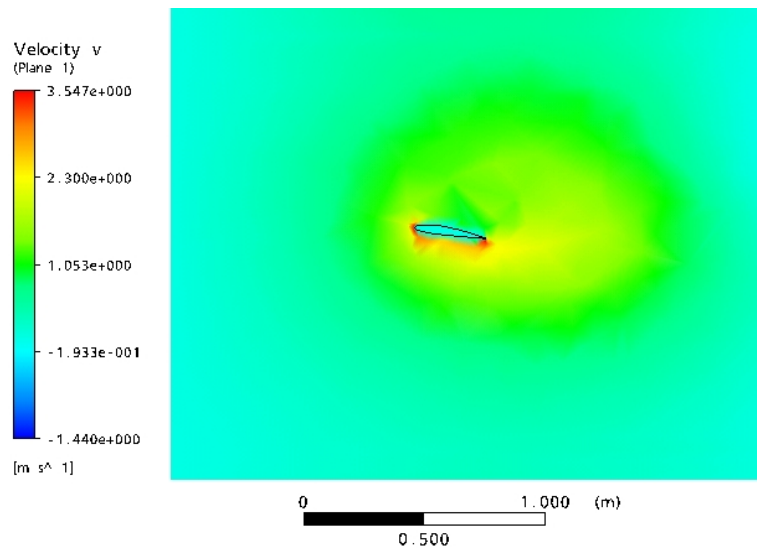


Figure 2.8: Spanwise air flow on wings with high angle of attack

This spanwise air flow reduces the efficiency of the wings by generating wing tip vortex and reducing pressure difference between the upper and lower surfaces. This is remarked in the ANSYS simulations, however using elliptical planform to form lift distribution yielding minimum induced drag [143, 146] would be impractical due to the very limited wing span and wide usage of high angle of attacks in the entire speed range. Instead, large winglets are joined to the wing tips (Fig. 2.9) that also reduce the necessary angle of

attacks for stable flight for 1° - 2° in the simulations.

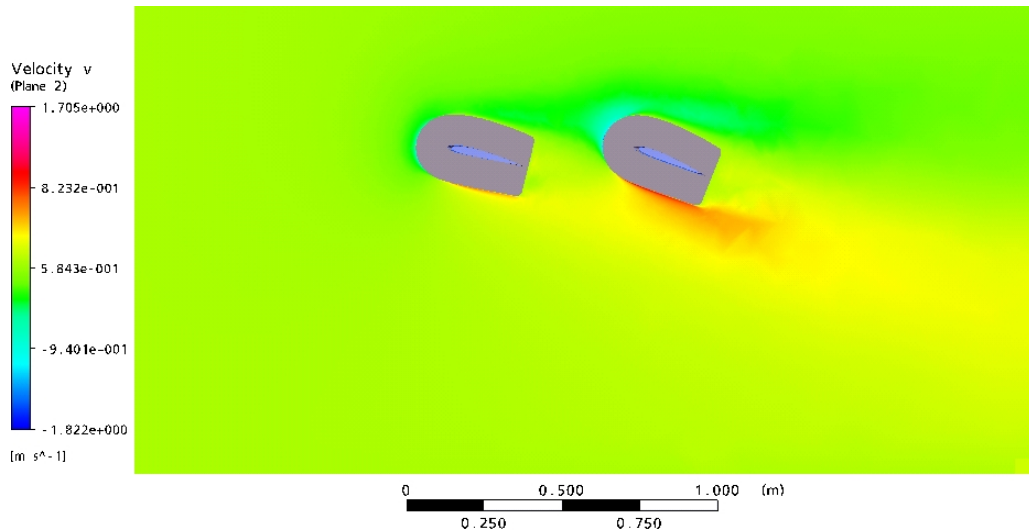


Figure 2.9: Reduction of the spanwise air flow by winglets

The final shape of the wings with the NACA 2410 airfoil, 25 cm chord length, 1 m wing span, the selected motor and the winglet is as in Fig. 2.10.

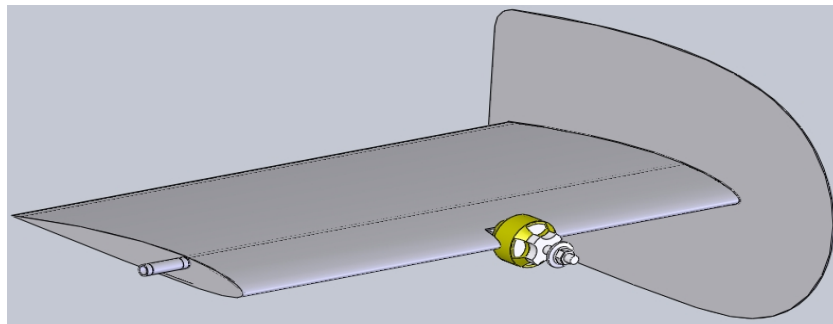


Figure 2.10: Aerodynamic design of the wing

From the ANSYS air flow simulations of the air vehicle with consecutive wings, it is noticed that the lift of rear wings is negatively affected by the downwash produced by the front wings (Fig. 2.11). This downwash makes the rear wings to behave like flying with less angle of attack in the air due to

the downwash angle, that increases with the angles of the front wings [145–147]. There are mainly three possible solutions to equalize the lifts of front and rear wings, that are increasing the rear wing area or thickness, placing rear wings at a higher place on the air vehicle and using rear wings with higher angle of attack.

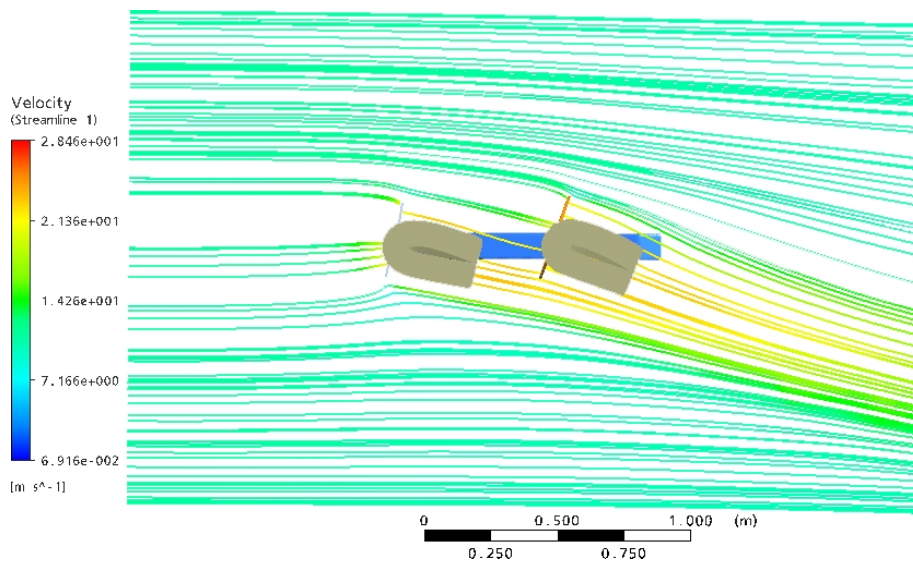


Figure 2.11: Streamlines showing the downwash and its effect on the rear wing

Increasing the wing area requires extension of the wing span which is already limited by the compactness requirements or increasing the chord length, which is not so desirable due to the excessive decrease in aspect ratio.

Increasing the thickness of the wing can solve the problem with considerable thickness increase, which also adds up to the drag, especially at high speeds. Placing rear wings at a higher place on the fuselage is a solution tested in ANSYS simulations, however the results showed that more than one chord length vertical distance is necessary to equalize the lifts of front

and rear wings as also stated in the literature [143, 145, 148]. To achieve this, the fuselage is needed to be built larger in vertical direction leading to a heavier structure, so this choice conflicts with the weight constraint for the air vehicle.

To make both the design and production less complicated, the front and rear wings are determined to be located at the same vertical level and the rear wings are used with higher angle of attack. In fact, this solution is very reasonable, since it directly attacks the source of the problem.

According to the simulations, SUAVI can fly most economically at around 40 km/h air speed with 10.5° front wing angle of attack and 12.5° rear wing angle of attack, while it can speed up to 68 km/h with 2° front wing angle of attack and 3.7° rear wing angle of attack. At 40 km/h, without any propeller slipstream, the risk of separation exists. However, the slipstream of the motors increases the airspeed on the wings with additional parallel to chord air flow and suppresses the risk of any separation on the wings.

2.2 Wind Tunnel Tests

To verify the aerodynamic design of SUAVI and measure the aerodynamic forces and moments generated in a variety of wing angle of attacks and power settings, wind tunnel tests are conducted. These tests are performed on a half-model of SUAVI in Istanbul Technical University's Gümüşsuyu closed circuit wind tunnel.

2.2.1 Wind Tunnel Test Facility

The low speed wind tunnel used in the experiments has a rectangular cross section with 1.1 m width and 0.8 m height. In the case of testing full

model of the aircraft having 1 m wingspan, there would be only 5 cm gap between the wing tips and the wind tunnel walls. As a result, wall effect would prevent realistic observation of the effects caused by the flows on the wing tips, which are highly effective on the efficiency of the wings.

A half model of SUAVI is designed and produced, which is just one half of the air vehicle cut on the longitudinal axis of the body through the vertical plane. Using half model is a common approach in wind tunnels, exploiting the fact that air flows on two symmetric halves of a body are also symmetric. Since the wings on the air vehicle are not affected by this division, the wings that are the same with the wings on the prototype are used. The half body is designed in CAD environment (Fig. 2.12) with all the connection parts for the sensor and CNC machined from bulk aluminum with the same outer shape, but with modifications in the inner shape for strength and connection to the force sensor (Fig. 2.13).

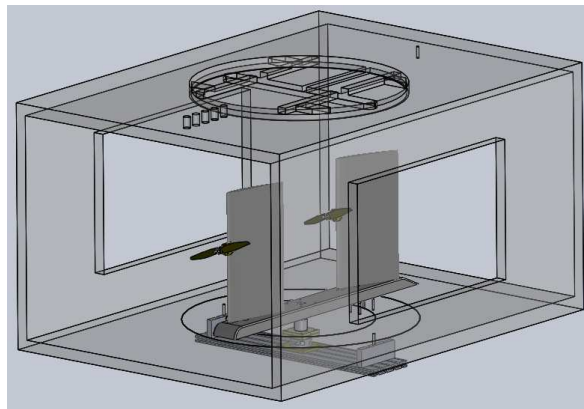


Figure 2.12: CAD drawing of the wind tunnel and the half model

The carbon composite fuselage has enough strength against bending and other loads due to its box structure and the wing tilt bearing parts, which extend from one side wall to the other and apply only lift and forward acting

forces on the fuselage. In the case of using half body, however, the U shaped structure cannot effectively withstand torsion on the longitudinal axis and the bearing parts only have one side to attach, which is not enough to prevent transmission of the bending moment due to the lift force on the wall.

The aluminum half fuselage is designed to prevent any deflection on the test model. There are angular scales for simple control of angle of attack on the sides of the fuselage (Fig. 2.13 a) and the same servo motors with the ones on the prototype to test the performance of the servos in real operating conditions. The half fuselage has double roller bearing supports for the tilting wings to prevent backlash and undesired friction on the wing roots (Fig. 2.13 b).

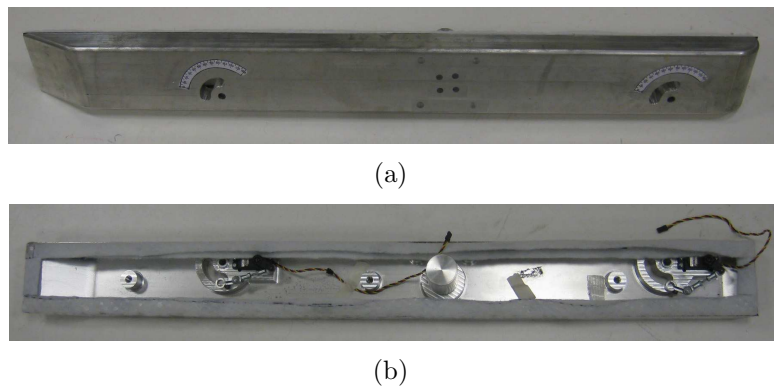


Figure 2.13: Outer (a) and inner (b) view of aluminum half body

An ATI Gamma series SI-130-10 6-DOF load cell is connected to the ground of the wind tunnel test room and the half model (Fig. 2.14) is connected to the sensor such that the half body is 3 mm above the ground. This gap prevents any incorrect measurement due to contact of body and ground, but may cause parasitic flows despite the boundary layer above the ground. To avoid these parasitic flows, soft acrylic felt is stuck on the walls at the

ground side of the half body, so there is a conformal material on this gap (Fig. 2.13 b).



Figure 2.14: Half model in the wind tunnel

2.2.2 Aerodynamic Tests

The aerodynamic tests in the wind tunnel are conducted in two main stages. First, lift and drag measurements on a single wing without any motor revolution are obtained. These measurements are performed to acquire the knowledge about the strength of the wing, about the sufficiency of the wing tilting servo torques to hold the wings at the desired angle of attack and to verify the wing profile features and measurement method through comparisons with the literature.

Second, lift, drag and pitch moment measurements on the complete half model are obtained to determine the optimum wing tip shape and to acquire information on both the necessary motor inputs and wing angles wrt. the body for the steady flight in the full range of flight speeds. These measurements are repeated for several input voltages to understand by how much the currents and the required motor power control pulses need to be changed for obtaining the same flight performance when the battery voltage decreases.

Lift and Drag Measurements on the Half Model with Single Wing

The initial aerodynamic tests are performed on the half model with only the front wing and without the rotor action (Fig. 2.15). These tests are conducted with straight cut wing tips. The emphasis on these tests is on the validation of the measurement method through the comparison of results with the literature, the strength of the wings in the high speed air flow and the accuracy of wing tilting servo positioning. Hence, air speeds up to 20 m/s (72 km/h) overshooting the target maximum speed are applied.



Figure 2.15: Half model with single wing in the wind tunnel

When the obtained data on the wing lift (Fig. 2.16) and drag (Fig. 2.17) coefficients vs. angle of attack are compared with the published data in the literature, it is seen that the measured values are consistent [146, 148–150]. The measured lift coefficient values, that are corrected for the aspect ratio of 4 without any vortex reducing device at the wing tip, become near to the section lift coefficients [145].

In Fig. 2.18, it is observed that the drag coefficient has a nearly vertical trend after the highest lift coefficient area and becomes very large with lower lift coefficients. This happens due to the fact that the lift coefficient becomes lower and drag coefficient increases rapidly as angle of attack is increased

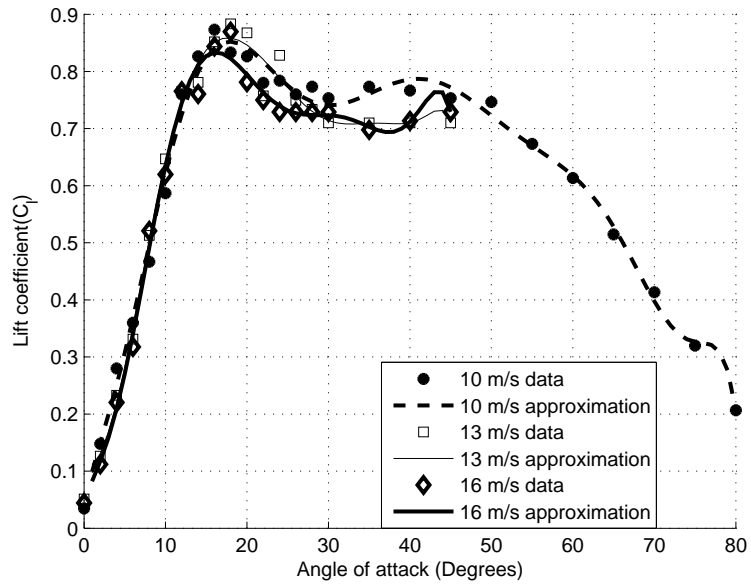


Figure 2.16: Lift coefficient vs angle of attack graph for one wing

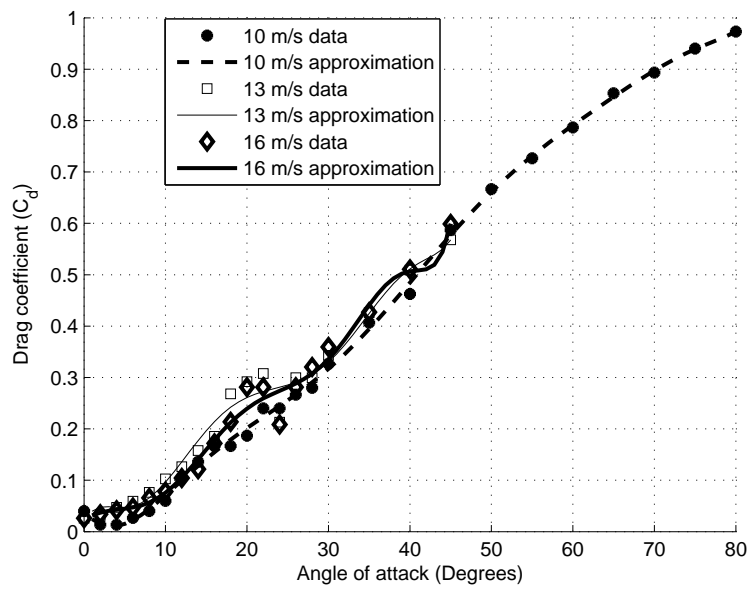


Figure 2.17: Drag coefficient vs angle of attack graph for one wing

further beyond the rise of separation. In the wing characteristic charts, this is generally not evident since these charts do not cover large angle of attacks, that are not useful for most fixed wing aircrafts.

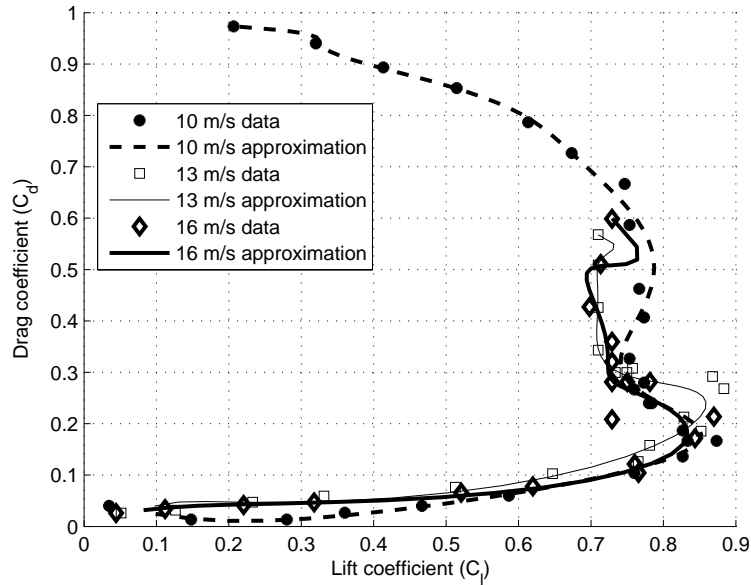


Figure 2.18: Drag coefficient vs lift coefficient graph for one wing

In the literature the lift and drag forces are modeled as

$$F_L = \frac{1}{2}\rho V^2 S C_L \quad (2.1)$$

$$F_D = \frac{1}{2}\rho V^2 S C_D \quad (2.2)$$

where ρ is the air density, V is the air speed, S is the plan area of the wing, F_L and F_D are the lift and the drag forces, and C_L and C_D are the lift and the drag coefficients, [145, 146, 148, 149]. For 10° , 13° and 16° angle of attacks the lift and drag vs air speed graphs can be seen in Fig. 2.19-2.20. As speed

increases with constant angle of attack, ρ , S , C_L and C_D do not change, so lift and drag forces are proportional with the square of the speed. This is apparent for lift force as in Fig. 2.19. In Fig. 2.20, the curvature of the curve fitting is not easily seen due to the low signal-to-noise ratio of the obtained measurement data on the measurement system.

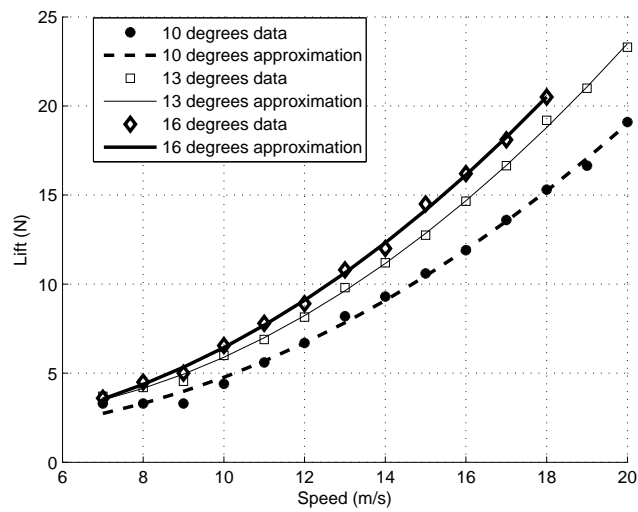


Figure 2.19: Lift vs speed graph for one wing

Besides validating the measurement method through comparison with available data in the literature, control of strength is also an important issue on the wind tunnel test. The wing is tested with 12° angle of attack in 20 m/s air speed generating 2.28 kg lift and 0.32 kg drag, where it is normally loaded with 1.125 kg lift.

Additionally, the wing tilting servos do not have any evident angle change while coping with the torque load on the wing axis as the speed is increased, even at very high angle of attacks like 70° and 75° at 11 m/s air speed. The wing is pivoted on the quarter-chord length behind its leading edge, so a

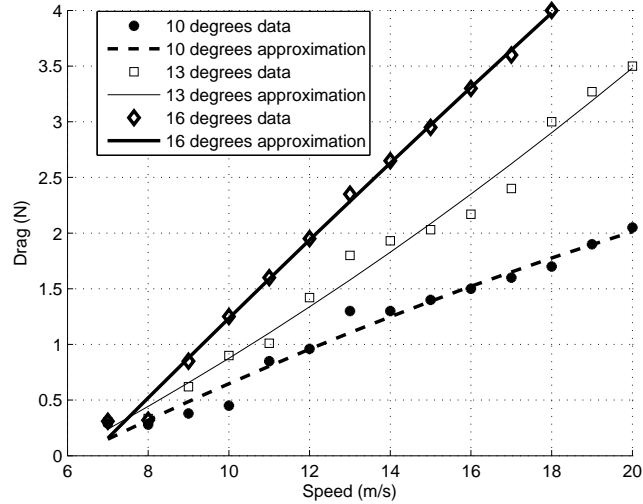


Figure 2.20: Drag vs speed graph for one wing

large moment on the tilting axis due to the area near the trailing edge needs to be balanced by the servos when abused.

Lift and Drag Measurements on the Complete Half Model

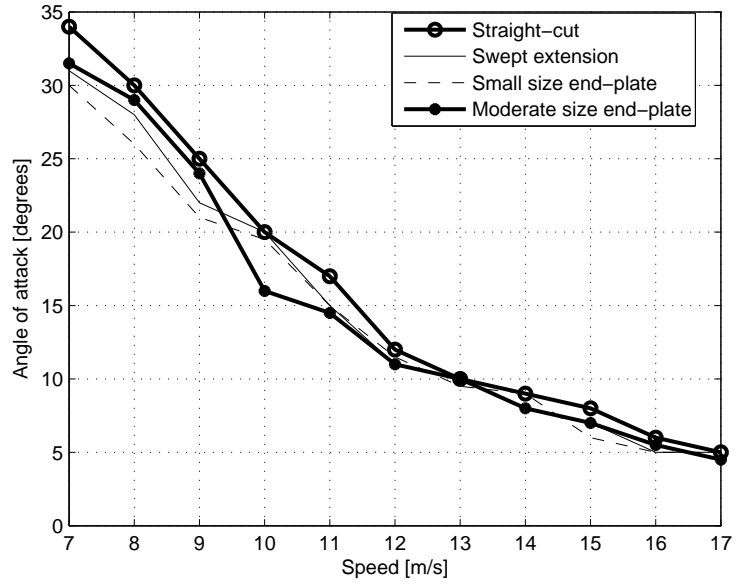
The first stage of the lift, drag and pitch moment measurements on the complete half model is performed to determine the optimum wing tip shape and size. To test the air vehicle power consumption for steady flight at the desired speed range, the wing angle of attacks and motor PWMs are adjusted such that the drag force on the half model is 0 N, pitch moment is 0 Nm and the lift is 22 N for balancing the half weight of SUAVI. The wing tip design is an important factor that can reduce the angle of attack and motor power requirements on SUAVI, that is an air vehicle with low aspect ratio wings. For this reason, a series of wing tip shapes and sizes are examined through nominal flight tests for the wing angle of attack (Fig. 2.21), motor PWM

(Fig. 2.22) and current consumption (Fig. 2.23). These wing tip shapes include straight-cut wing tip, short swept-wing alike wing extension and two different sizes of end-plates.

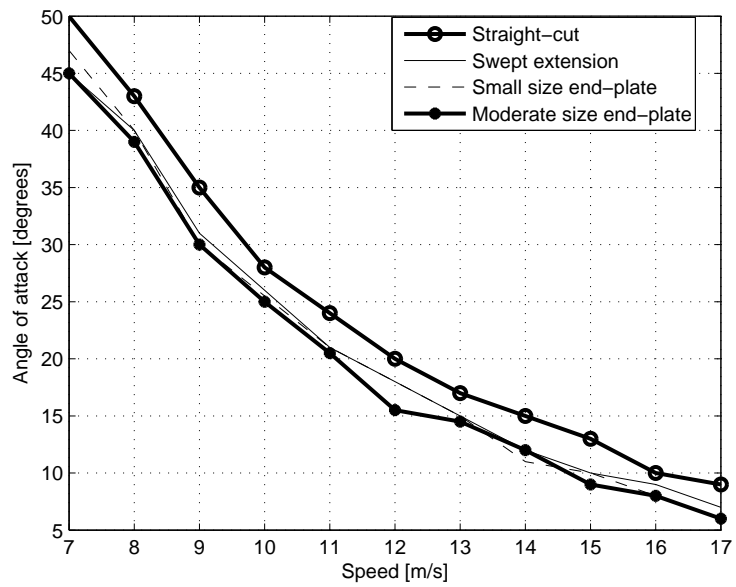
In the test results, it is observed that the utilization of moderate size end-plate leads to generally the least values for wing angle of attack, motor PWM requirements and current consumption.

A wing tip end-plate operates mainly by blocking the spanwise flow of high pressure air at the lower surface of the wing towards the tip and by blocking the spanwise flow from the outside into the low pressure area at the upper surface of the wing. By doing this, it prevents the reduction of favorable pressure difference that lifts the air vehicle and the increase of induced drag, especially for an air vehicle that often uses high angles of attack [144, 146]. Since this favorable pressure difference is generated by consuming energy for propulsion, using winglets increases the flight range of the air vehicle.

During the wind tunnel tests of the SUAVI, it is observed that severe spanwise air flows occur on both upper and lower sides of the wing at up to 80 mm vertical distance from the chord line. For this reason, the effect of short swept-wing alike wing extension, which does not extend vertically to the spanwise flow area is not significant. Using a large end-plate with size 420 mm x 440 mm to prevent the effect of these spanwise flows results with the current draw of 11.2 A for two motors with the expense of carrying giant wall at the wing tips. On the other hand, using winglet with size 165 mm x 280 mm causes only 0.4 A more for two motors with much less weight and size. Further reducing the size of the winglets increases the current requirement with a higher tendency, so this size is determined as an optimum solution,

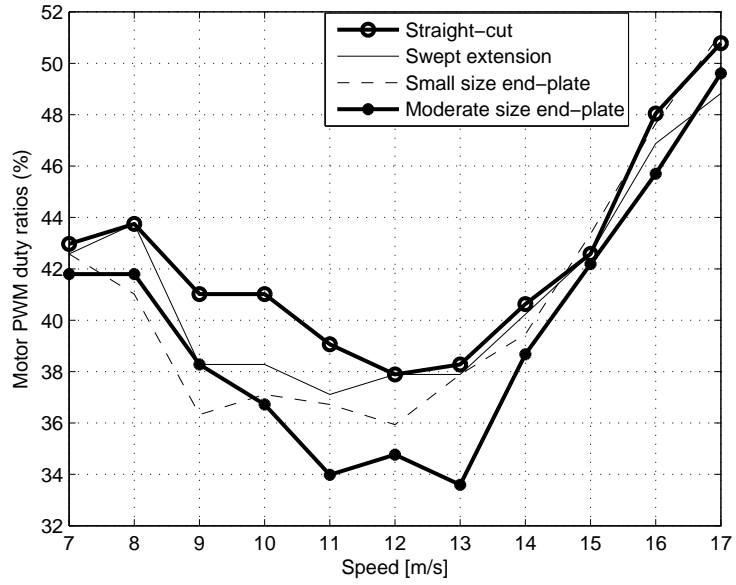


(a)

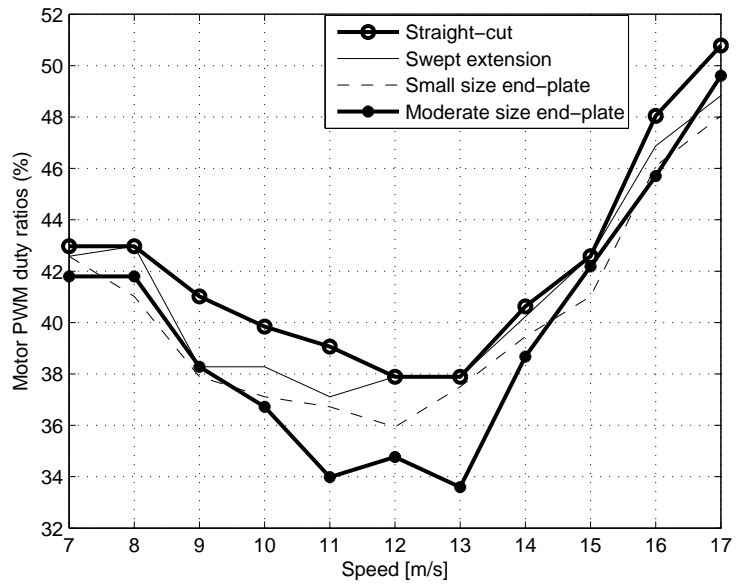


(b)

Figure 2.21: Front (a) and rear (b) wing angle of attacks in the tests of some of the wing tip choices



(a)



(b)

Figure 2.22: Front (a) and rear (b) motor PWM duty ratios in the tests of some of the wing tip choices

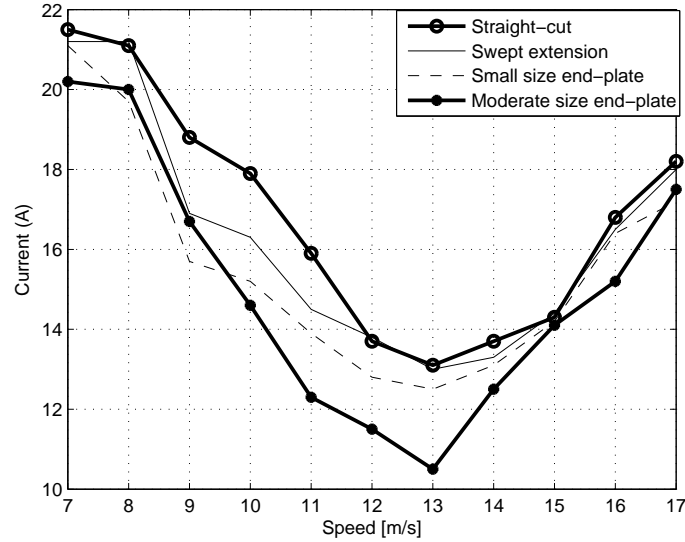


Figure 2.23: Current drawn by two motors for various wing tip choices

regarding both the winglet performance and weight.

The determined winglet is placed such that its back side is coincident with the trailing edge of the wing, since it is observed that the further horizontal extension beyond the trailing edge of the wing does not have evident effect on the performance. Additionally, the winglet's horizontal midline is 10 mm lower than the chord line of the wing, since the thickness of spanwise flow at the bottom of the wing extends more especially at high angle of attacks.

Front side of the winglet is rounded to further decrease the weight and increase the aerodynamic efficiency of the winglets. Through the utilization of this winglet, it is calculated that the air vehicle will be able to consume up to nearly 15 % less energy, increasing the flight duration up to 10-12 minutes.

With the final shape of the winglet, the wing angle of attacks, motor PWMs and current requirements of the half model are as listed numerically in Table 2.4 and as depicted in Fig. 2.24-Fig. 2.26.

Table 2.4: Motor throttle PWM percentages, wing angle of attacks and current drawn by two motors for nominal flight

Air speed (m/s)	Front motor (%)	Rear motor (%)	Front wing angle (°)	Rear wing angle (°)	Current (A)
0	62.5	62.5	90.0	90.0	32.0
1	62.5	62.5	88.0	88.0	32.4
2	62.5	62.5	86.0	86.0	32.4
3	54.3	59.0	76.0	86.0	30.8
4	46.9	53.5	68.0	82.0	27.0
5	41.0	46.1	54.0	71.0	22.8
6	41.8	41.8	41.0	51.0	21.0
7	41.8	41.8	31.5	45.0	20.2
8	41.8	41.8	29.0	39.0	20.0
9	38.3	38.3	24.0	30.0	16.7
10	36.7	36.7	16.0	25.0	14.6
11	34.0	34.0	14.5	20.5	12.3
12	34.8	34.8	11.0	15.5	11.9
13	33.6	33.6	10.0	14.5	10.5
14	38.7	38.7	8.0	12.0	12.5
15	42.2	42.2	7.0	9.0	14.1
16	45.7	45.7	5.5	8.0	15.2
17	49.6	49.6	4.5	6.0	17.5

From the nominal flight tests, it is observed that the wing angles (Fig. 2.24) are similar in shape with motor PWM requirements (Fig. 2.25) up to the airspeed of 6 m/s and beyond that speed the motor PWMs become nearly the same. At 11-14 m/s air speeds, the PWM values are at the lowest level, but as the speed further increases the required PWM values become larger to cope with the increased parasite drag on the air vehicle at high speeds,

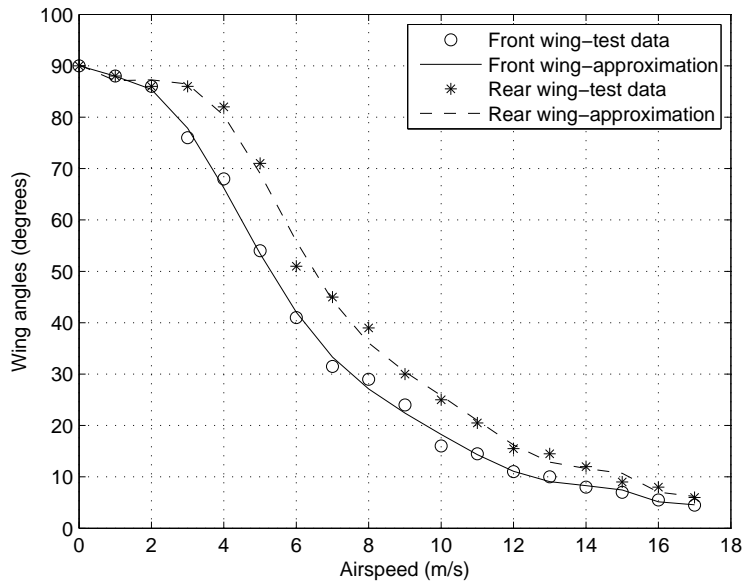


Figure 2.24: Wing angle of attacks for steady flight at various speeds

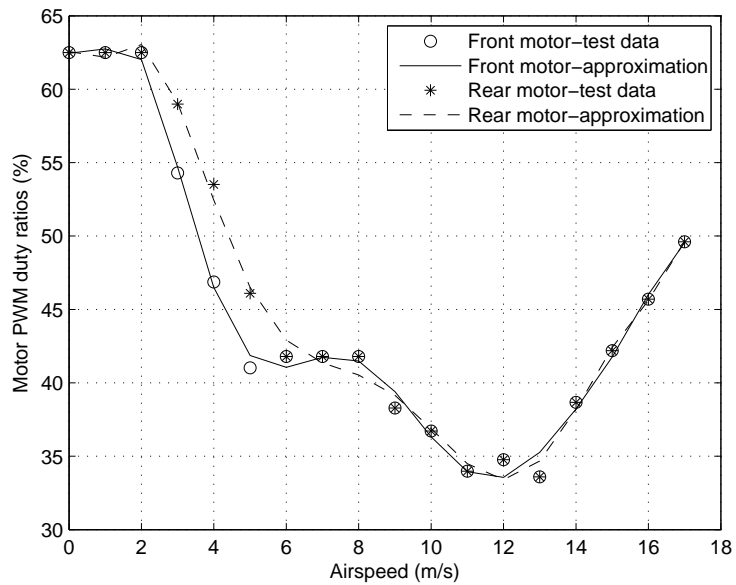


Figure 2.25: Motor PWM duty ratios for steady flight at various speeds

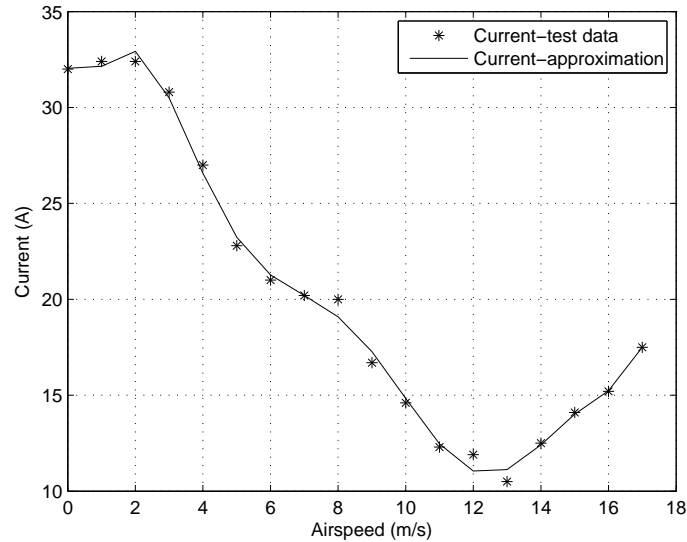


Figure 2.26: Current drawn by the half model for steady flight at various speeds

despite the continuous decrease in induced drag due to the decrease in wing angles [147].

From the angle of attack vs. speed graph (Fig. 2.24) it is noted that up to 2 m/s air speed, the front and rear wing angles are the same because of the relatively insignificant effect of the air flow. However beyond that speed, there is a difference between the wing angles making the rear wing angle higher up to 10° at low speeds. This result is expected due to the fact that the rear wing operates in the downwash and wake of the front wing and the lift difference becomes very crucial at low speeds due to the larger wake of the front wing at high angle of attack.

The current graph (Fig. 2.26) is similar to the average of the front and rear motor PWM results. The lowest power consumption air speed range is 12-13 m/s, where the wing angle of attacks are near to the stall angles for the

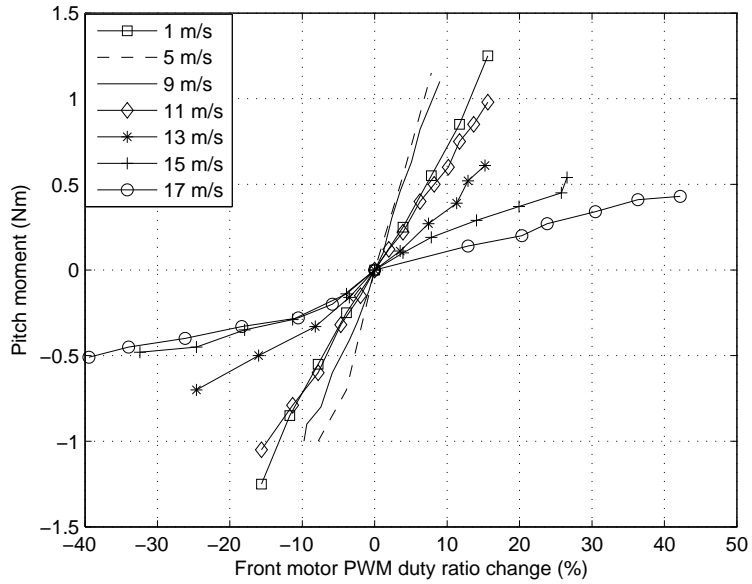
wings, which are the limits for linear increase in both lift and drag. Further reduction of the airspeed by increasing the wing angles reduces the lift and exponentially increases the drag, therefore at lower speeds additional motor thrust is required. Further increase of the airspeed leads to the reduction of wing angles, but the overall drag on the air vehicle increases with the square of the speed, therefore at higher speeds additional motor power is required.

During the flight of SUAVI, pitch control is definitely necessary at the entire speed range. To have a model of pitch moment responses wrt. both motor power changes and wing angle changes, aerodynamic tests are conducted in the wind tunnel.

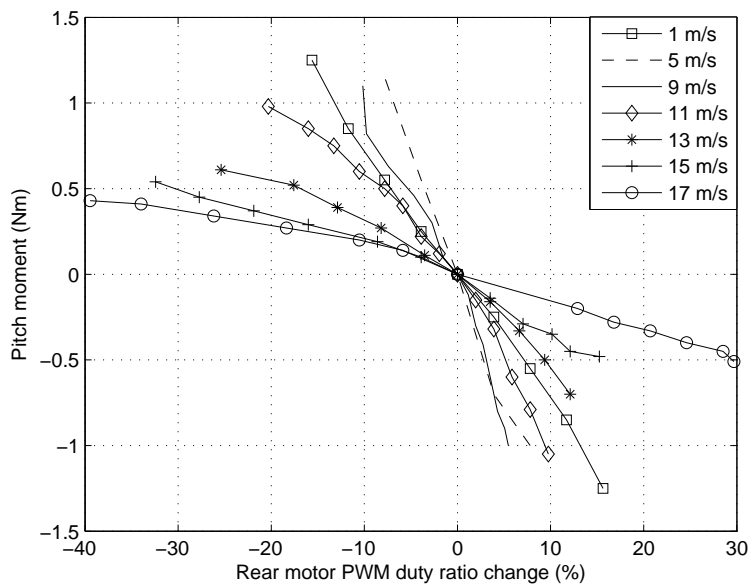
In the first step of these tests, the half model is adjusted to the steady flight configurations at each air speed sample and the front motor PWM is increased, while the rear motor PWM is decreased to generate positive pitch moment and vice versa. By doing this, the propeller slipstream speed on each wing is changed, so the pressure difference that provides the lift on each wing is affected.

Additionally, the angle of attack of each wing causes the existence of a vertical force component due to each motor thrust. In the results of this first test step (Fig. 2.27), it is observed that 1 Nm pitch moment can be generated through only motor PWM differentiation at up to 11 m/s air speed and the maximum pitch moment generated through this method declines to around 0.4 Nm gradually.

In the second step of these tests, the half model is adjusted to the steady flight configurations at each air speed sample, but this time, the front wing angle is increased, while the rear wing angle is decreased to generate positive pitch moment and vice versa. By doing this, the lift of each wing is altered



(a)



(b)

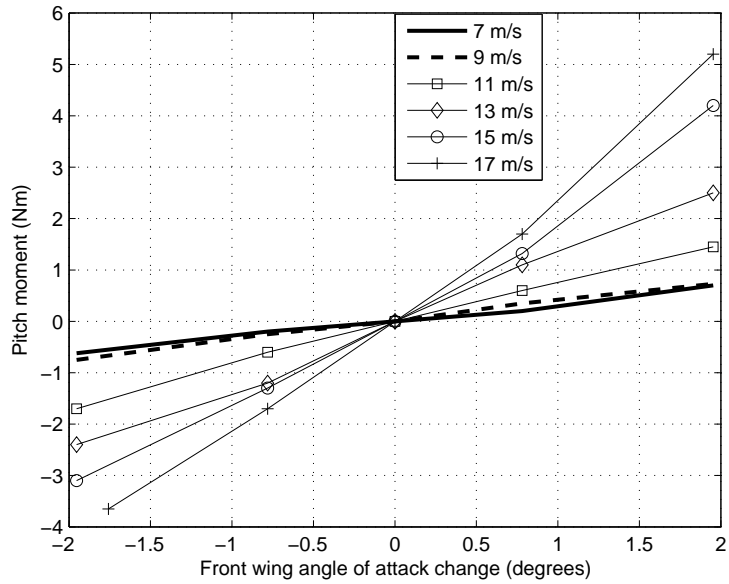
Figure 2.27: Pitch moment generated at steady flight wrt. front motor (a) and rear motor (b) combined PWM changes

through the change of angle of attack. In these tests (Fig. 2.28) it is observed that even with 2° differentiation on both wings, it is possible to generate pitch moments from 0.6 Nm up to 5.2 Nm depending on the air speed.

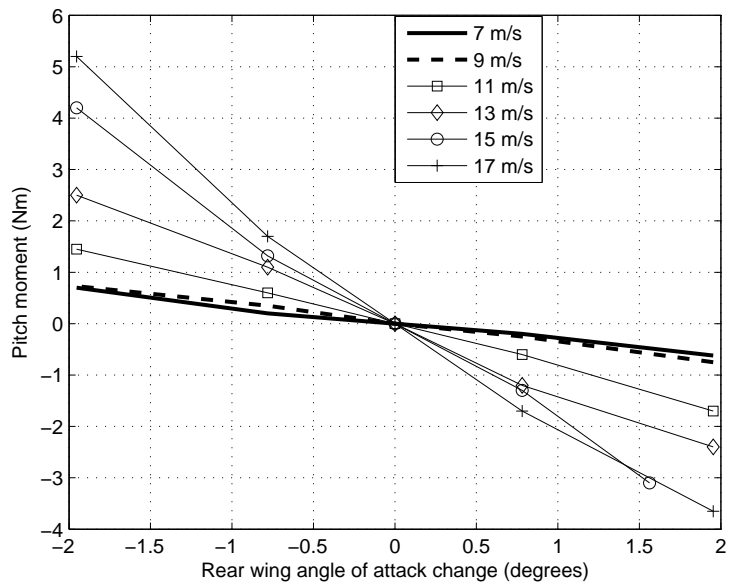
It is remarkable that pitch control by only motor PWM differentiation diminishes as the air speed increases, while pitch control by only wing angle change becomes very effective in the same circumstance. This is due to the facts that at high air speeds the thrusts of the engines inevitably become lower, the vertical thrust component on the lift decreases due to low angle of attack and change on wing angle of attack influences the lifts dramatically. It is expected that even 0.5 Nm pitch moment will be sufficient to stabilize the air vehicle in most cases based on the estimated pitch inertia of 0.4 kgm^2 . For the roll, yaw controls and additional pitch control at high speeds, the elevons and rudder on the tail will serve as control surfaces.

SUAVI is an electric air vehicle that relies on the on-board battery power. Since the voltage of the batteries decreases as time elapses during the flight, it is necessary to measure the effect of battery voltage change on the controls of the air vehicle and compensate for this effect. To develop a method for compensating this, the stable flight conditions for the entire speed range are set for a series of power supply voltages (Fig. 2.29).

Since, this is mainly a problem caused by motor power loss, motor PWM values are updated, instead of making any wing angle change. The current drawn by the motors on the half model is depicted in Fig. 2.29 b. In these tests it is observed that the change in consumed power is negligibly small, so there is an option to regulate the mean values of the motor PWMs in accordance with the measured current of the motors.

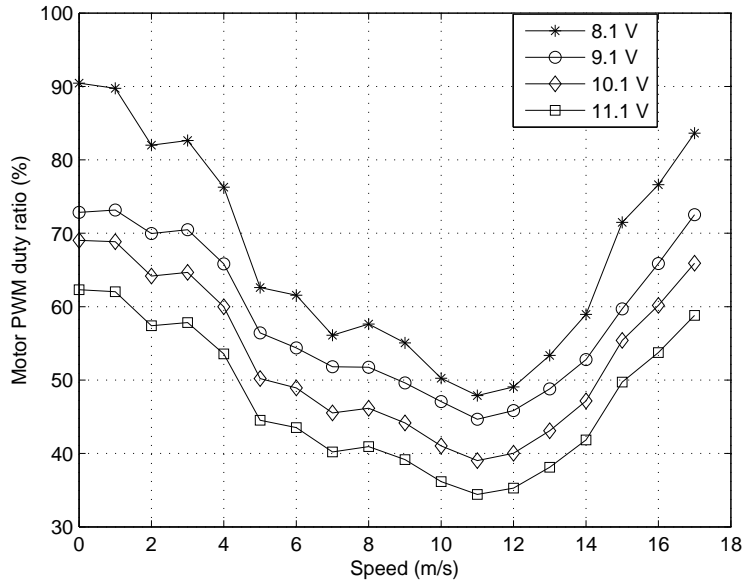


(a)

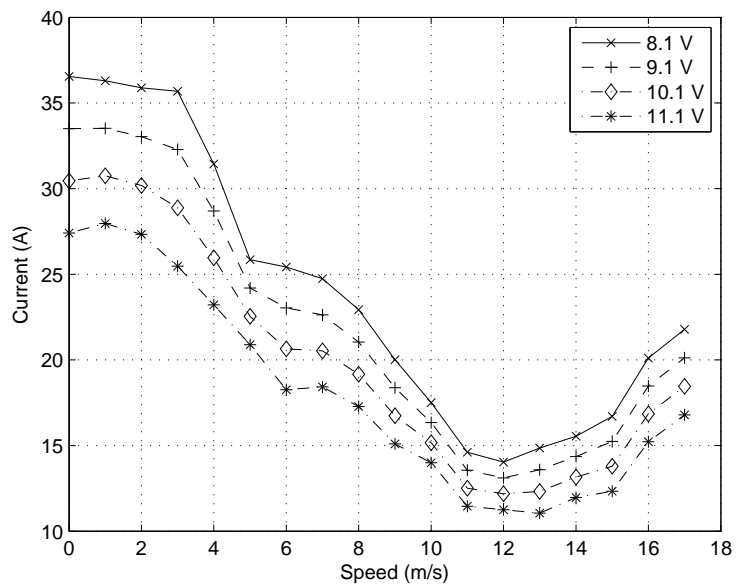


(b)

Figure 2.28: Pitch moment generated at steady flight wrt. front wing (a) and rear wing (b) combined angle of attack changes



(a)



(b)

Figure 2.29: Front, rear motor PWMs (a) and the current drawn by two motors (b) for steady flight at various speeds under several motor voltages

Chapter 3

3 Mechanical Design and Prototyping

The main goal of the mechanical design of SUAVI is to obtain the most lightweight structure that is capable of withstanding the possible loadings in vertical, horizontal and transition flight modes. To achieve this, carbon fiber reinforced plastic, which is a material to be known as the best in terms of strength/weight ratio, is determined to be the production material of SUAVI. To improve the durability in compression loading, usage of sandwich structure on the entire body is preferred. In this sandwich structure, lightweight core material is surrounded by carbon fiber cloth on both sides. This structure makes the skins of the UAV to perform like an I-beam, in which the strong material is kept at outer sides to increase the second moment of inertia and low-density material is kept inside just to keep the outer sides parallel to and apart from each other. By this way, the skins of the UAV can be produced lightweight and still strong, even against bending and compression.

There are two mechanical designs and prototypes of SUAVI, that have very similar aerodynamic designs. The first flight tests on SUAVI, especially the VTOL flights, are mostly conducted on the first prototype, whereas the second prototype is designed as a much stiffer, lighter and more useful structure with the tremendous help of experiences gained on both the production and the flight tests of the first prototype.

3.1 Mechanical Design and Production of the First Prototype

The mechanical design and production of the first prototype of SUAVI can be seen as a trial stage for the prototyping of the aerial vehicle. There has been shortage of experience on building a UAV with such small dimensions and such strict weight limits. The available core material has been balsa wood with 1 mm thickness and the shape of both the fuselage and wing skins have been simplified to simplify the production and to observe the behavior of the materials utilized in the design. However, the production and flight tests of this first prototype have provided valuable experiences for the design of the second prototype.

3.1.1 Mechanical Design of the First Prototype

The fuselage in the first prototype is designed to be produced in one mold as two symmetrical sides and have relatively simple shapes at front and back of the fuselage. This is due to the lack of knowledge on how the vacuum bagging method and plain woven carbon fiber cloth complies to the shape of the 3D fuselage at the time this design is made. The fuselage is designed to be a symmetrical wing with vertical orientation, very long chord length and comparably very small wing span. This form is relatively less complicated for the production and it also offers low air drag coefficient. The fuselage consists of two main parts, that are the flat cover on the top of the fuselage for accessing the electronic system inside and the lower part that is the backbone of the prototype with U-shaped crosssection. It is obvious that this design can be weak against torsion on the fuselage, since the upper side

of the fuselage is a separate part and the box structure cannot be satisfied. To fight against this weakness, additional ribs are designed to be placed into the fuselage (Fig. 3.1).

The wings in the first prototype are designed to have upper and lower skins that encapsulate a pultrusion carbon composite tube wing spar and small wood parts. These wood parts act as interfaces between the spar and the wing skins. The inner thickness of the wings at quarter chord length, where the spars are connected to the wings for the lifting at the lift center, are 20 mm and the diameter of the wing spars are 10 mm, so these wood parts fill the gap inbetween to provide homogenous contact (Fig. 3.1).

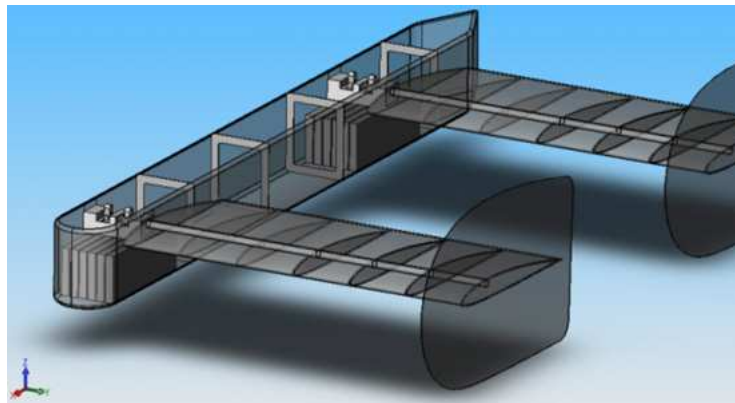


Figure 3.1: Mechanical design of SUAVI

The wing tilting mechanism is designed to be supported by a delrin block that is machined to carry the high torque servos of the system and to act as a bearing for the tube shaped wing spars (Fig. 3.2). The material is selected to be delrin due to its low friction surfaces for smooth rotation of the wings, even at high loads transmitted by the wings. These delrin parts are designed to be produced as one part and fixed to the inner sides of both side skins. The wings produce large bending moments at the roots and transmit these

bending moments to the delrin blocks. These delrin blocks transfer only the lifting and friction forces to the fuselage skins through shear forces on the glued interfaces. If these bending moments are transmitted directly to the fuselage's thin skins, these skins cannot survive even in the presence of small forces applied by the wings.

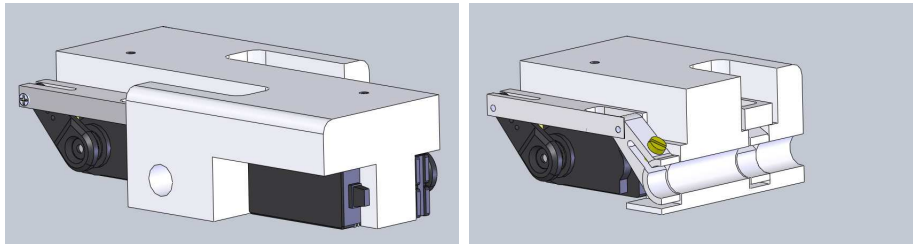


Figure 3.2: Mechanical design of the wing tilting mechanism

Additionally, the batteries on the first prototype are planned to be placed just under the delrin blocks (Fig. 3.1). This place is chosen to improve the static stability of SUAVI using the weight of the batteries, that is a large proportion of the total flight weight. Another important reason is that carrying the batteries as near to the wings as possible minimizes the bending moments on the fuselage, which are caused again due to the weight of the batteries.

In the aerodynamic analysis of SUAVI performed in ANSYS Fluid Flow simulation environment, the aerodynamic pressure distributions on the wings can also be obtained. When these distributions are fed into the ANSYS Mechanical Analysis environment, the stresses generated on the wings are estimated. For the worst case scenario on the wing loadings, 68 km/h air speed with 10° angle of attack is chosen (Fig. 3.3). Normally, wing angle of attacks at such high speeds is around $2-3^\circ$ and at 10° angle of attack both the lift and drag forces on the wings become 2.5-3 times the nominal values.

As a consequence, the maximum stress on the wings is estimated as 36.4 MPa, that is observed on the carbon tube at wing root instead of the wing skin. The mechanical safety factor becomes 8, even with the 292 MPa tensile stress of the wet lay-up carbon fiber, that is the lowest among the values for the carbon tube production. The stresses on the wing skins are found to be very small to mention.

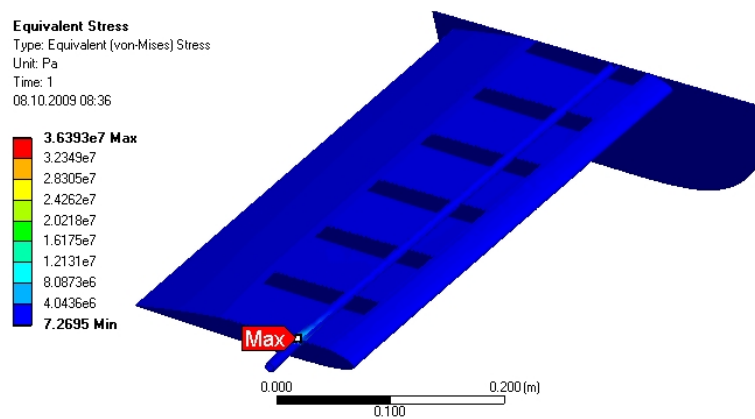


Figure 3.3: Stress analysis of the wing for the worst case scenario

The mechanical analysis for the fuselage of SUAVI are also performed at 2.5 g vertical acceleration (Fig. 3.4). Consequently, the maximum stress on the fuselage is found to be 4 MPa.

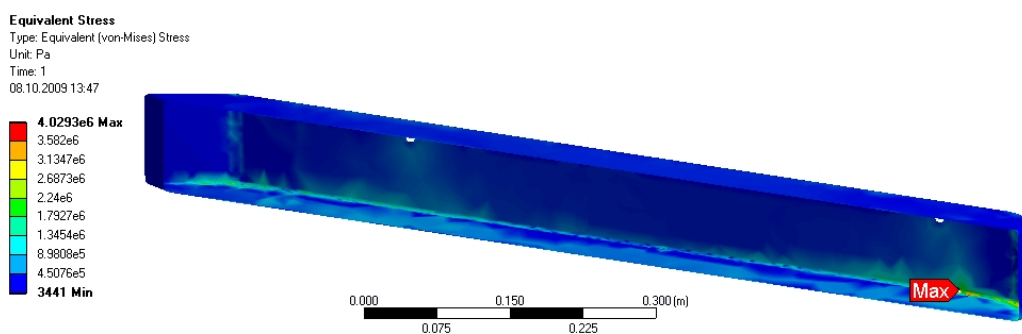


Figure 3.4: Stress analysis of the fuselage under 2.5 g vertical acceleration

In the tensile tests, that are conducted in the Universal Testing Machine, the maximum stress that the sandwich structured carbon composite material with balsa wood core, which was the candidate material for the production of the first SUAVI prototype, can withstand is found to be approximately 95 MPa. Accordingly, the mechanical design of the fuselage is found to have a safety factor of approximately 24.

3.1.2 Production of the First Prototype

The production of the first prototype begins with the production of the molds for the composite manufacturing. The molds are milled from cast aluminum in a CNC milling machine (Fig. 3.5 a, b) and become ready for composite production with additional sanding (Fig. 3.5 c-e).

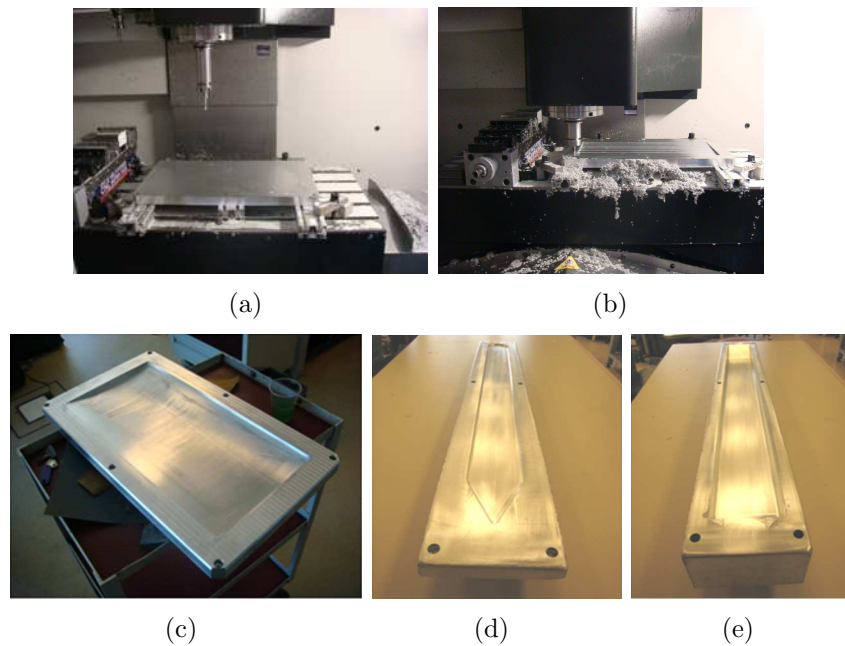


Figure 3.5: Production of the molds (a, b), finished mold of the wings (c) and the molds of the fuselage (d, e)

The SolidWorks part files are exported into CAM environment, where the cutting method is defined and the G code is generated, and the G code is fed into the milling machine or lathe. The CNC machines complete the rest of the task automatically when the position of the material is introduced to the machine properly.

In the production of the first prototype, sandwich structured carbon composite material with balsa wood core is used. Balsa is a very lightweight wood that is also widely used in RC model airplane production. This material is preferred, due to its low-density, conformity onto the curved shapes of the wings and availability in the market. The carbon fiber material that surrounds the honeycomb is a 0-90 plain wave carbon cloth. The reason for using woven carbon fiber is to provide sufficient strength against stresses in every possible direction. The carbon fiber cloth that is used in the production has a density of 90 g/m^2 , which is the lowest available in the market.

The composite parts are fabricated by hand lay-up process on the described molds with vacuum bagging technique applied in the curing phase for higher fiber to resin ratio and better fiber wet-out [151, 152]. This process is performed by laying up and wetting the outer carbon layer on the mold with epoxy resin, placing the balsa plates, laying the second carbon layer and wetting it also with epoxy resin (Fig. 3.6 a, b).

The perforated film is then laid to prevent the resin absorber from sticking to the carbon cloth and then the resin absorber is laid on the top both to soak still existing excess resin (Fig. 3.6 c) and to provide the air flow even from a distant place on the mold from the vacuum pump's pipe. Thereafter, the sealant tape is applied to the outer boundaries of the mold and the vacuum film is covered on the top to provide a vacuum zone (Fig. 3.6 d).

When air is evacuated from the mold surface, the vacuum film presses on this multi layer structure and during the curing, the carbon cloths stick to the core material in a rigid manner (Fig. 3.6 d, e). When curing is completed after 8 hours, the vacuum film, resin absorber and perforated film are removed, and the composite part is revealed (Fig. 3.6 f, g). After the removal of the unwanted excess parts, the composite wing skins become ready for assembly to constitute the wings (Fig. 3.6 g, h). The carbon fuselage skins are produced similarly.

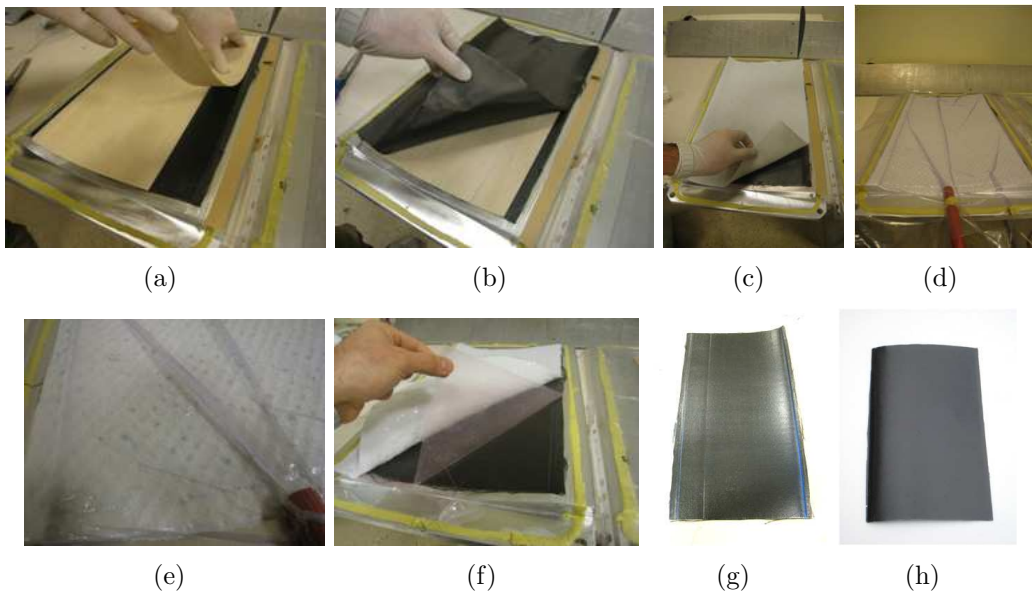


Figure 3.6: Hand lay-up (a, b), vacuum bagging processes (c, d, e, f), cured skin (g) and finished skin (h)

For the assembly of the wings, first, the wood parts, which act as interface between the carbon composite spar and the wing skins, are glued on the wing skin (Fig. 3.7 a). Then the near sides of the wings are glued at the near ends of the wings (Fig. 3.7 b). The carbon composite spar is fixed on its place (Fig. 3.7 c) and the other wing skin is joined to form the wing (Fig.

3.7 d). With the assembly of motor (Fig. 3.7 e), the wing becomes ready to be assembled on the prototype (Fig. 3.7 f).

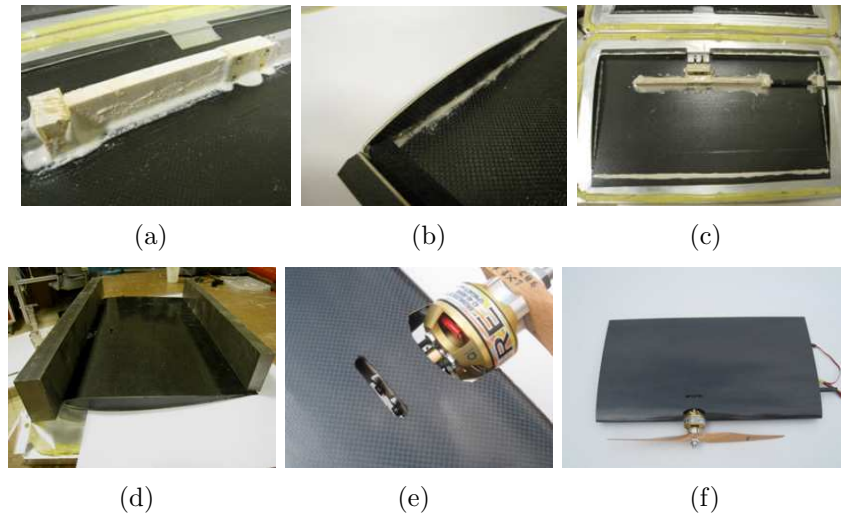


Figure 3.7: Wood interface parts being attached to the lower wing skin (a), near sides of the wings being glued (b), carbon composite spar being fixed to the wing (c), upper skin joining the lower skin (d), motor joining the wing (e) and the finished wing

The assembly of the fuselage begins with the assembly of the two side halves. These parts are first matched with each other (Fig. 3.8 a) and joined using impregnated carbon cloth to form the similar carbon composite structure also at the joining line (Fig. 3.8 b). The wing tilting mechanism is prepared through the milling of delrin block and the servo connection arms, the assembly of the high torque servos and their connection arms (Fig. 3.8 c). The wing tilting mechanisms are attached on the carbon composite fuselage (Fig. 3.8 d). The prototype becomes ready for flight with the addition of the electronic control system, wirings and batteries (Fig. 3.8 e).

The ready for flight weight of the prototype is measured to be 4619 g, in which a battery group with only 19.2 Ah capacity can be placed. The

produced SUAVI prototype can be seen in (Fig. 3.9).

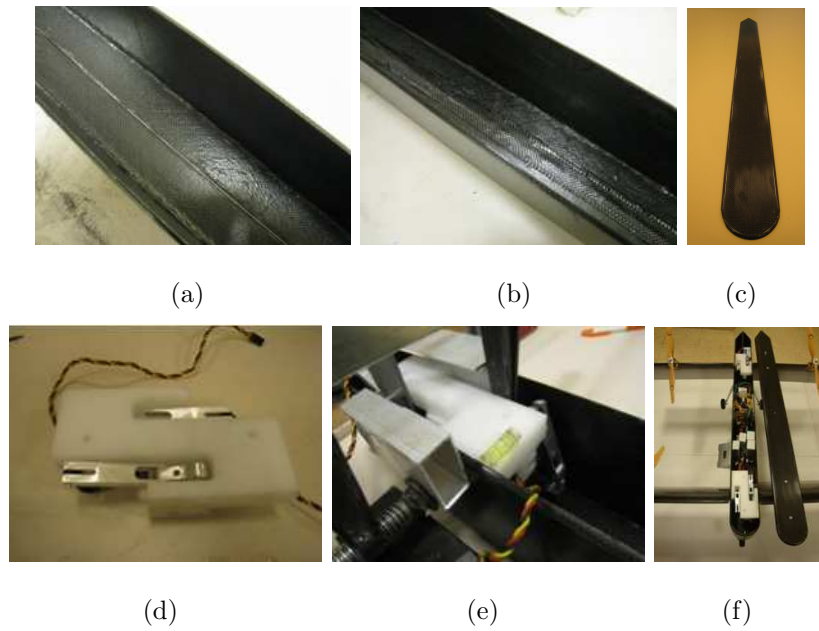


Figure 3.8: Matching (a) and joining of the two halves of the fuselage (b), the cover (c), assembly of the wing tilting mechanism (d), attachment of the wing tilting mechanism on the fuselage (e) and the final assembly (f)



Figure 3.9: SUAVI prototype in horizontal (a) and vertical (b) flight modes

3.2 Mechanical Design and Prototyping of the Second Prototype

During the flight tests of the first prototype of SUAVI, several problems both in terms of structure and placement of components are observed. For instance, the weight of the delrin blocks (660 g), the landing gear set and the carbon composite skin that is not light enough, caused a reduction in battery capacity. Utilization of less number of batteries than planned to handle even more energy consumption to lift the heavier than planned prototype resulted in short flight durations.

Additionally, due to the productional limits, the ribs designed for the installation into the fuselage could not be placed and to solve the torsion problem, an aluminum profile was placed between the delrin blocks, which added more weight on the prototype. The placement of the batteries into the fuselage caused the rolling inertia of the UAV to be very low, which made the aircraft less stable in rolling motion.

Most importantly, the separate wing tilting between right and left wings, and the backlash in the bearings of the wing spars made the accurate wing angle control of SUAVI impossible. This prevented the trials of horizontal flight on the first prototype of SUAVI. To solve these problems, a new SUAVI prototype with lighter and stronger structure, increased battery capacity and accurate wing angle tilting system is designed.

3.2.1 Mechanical Design of the Second Prototype

For the reduction of weight of the prototype, the reduction of the composite body weight is an important factor. Hence, the method of carbon composite

skin production is revised and some commercially available core materials, which are also used in composite aircraft production, are experimented for the contribution in terms of strength and weight.

For the experimentation of skin strength, several trials in the breaking tests with Universal Testing Machine (UTM) are conducted according to the standards for three point bending tests [153]. In these tests, carbon composite specimens of 20 mm x 100 mm size with Aramid honeycomb, balsa and Aeromat cores are placed on the UTM with the distance between supports set as 50 mm (Fig. 3.10).

The measurements are taken using 10 kN strain gauge and the bending speed is set as 2 mm/min as the standards dictate (Fig. 3.11). In the three point bending tests, it is observed that the specimen with Aramid honeycomb core fails at 24.09 N, whereas the one with Aeromat fails at 18.52 N and with balsa fails at 16.43 N. The specimen with Aramid honeycomb core have performed better since it is not layered parallel to the skin material, so it protects the integrity of the sandwich material even in the existence of reasonable bending forces.

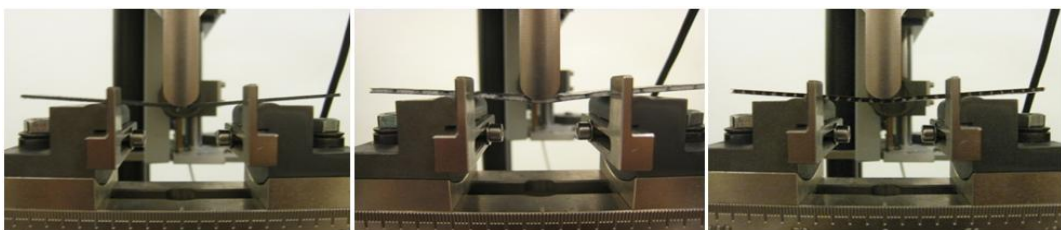


Figure 3.10: Balsa (a), Aero-mat (b) and Aramid honeycomb (c) in flexure test

As another advantage, Aramid honeycomb is a lightweight material because it only consists of thin strips bound together to form the honeycomb



Figure 3.11: Specimens with balsa (a), Aero-mat (b) and Aramid honeycomb (c) core material

shape and the air inbetween, whereas balsa, which is the lightest wood known, and Aeromat are materials without any air gap to become further lighter. The weight per area for the produced specimens with Aramid honeycomb is 350 g/m^2 , whereas it is 450 g/m^2 for balsa and 550 g/m^2 for Aeromat.

The sandwich structure that carries the stresses on the wings, transmits the generated forces to the carbon composite tube wing spars. Likewise, the aluminum elbow connection parts connect the landing arms and the electric motors to the spars to transmit the landing impact and motor thrusts to the fuselage through a durable and stiff chassis. The spars are attached to the inner walls of both the upper and lower wing surfaces, providing nearly all stresses on the wing surfaces to be in tension and transmitted continuously to the spars (Fig. 3.12 a).

The motors are mounted nearly at the mid-span of the wings and the landing arms are placed directly behind the motors to minimize possible bending moments observed at touchdown instants. There are tail-fin alike extensions designed for the tips of the landing arms to prevent the failing of wing tilting servos to keep the wings vertical during possible problematic touchdowns with some forward motion. The winglets are only fixed to the spanwise ends of the wing surfaces, since they are not to encounter massive forces (Fig. 3.12 b).

Additionally, the Li-Po batteries are located in the wings just behind the wing spars near to the wing root, where the longer side of the batteries is in spanwise direction (Fig. 3.12). The reason for such a placement is to keep the rolling inertia near to pitching inertia and at a reasonable level for better stability characteristics. The rotational inertia becomes larger as the dominant weights are placed farther from the rotation center and as the rotational inertia becomes larger, the effect of a moment on rotational acceleration becomes lower. Batteries could also be placed at the center of gravity of the UAV, however this would result in very low rotational inertia causing the UAV to rotate due to even very small disturbances, which is very undesirable. Placement of the batteries on the wings also helps reducing the critical bending moments on the wing roots and the forces on the wing tilting mechanism, which consequently adds to the reliability of the system.

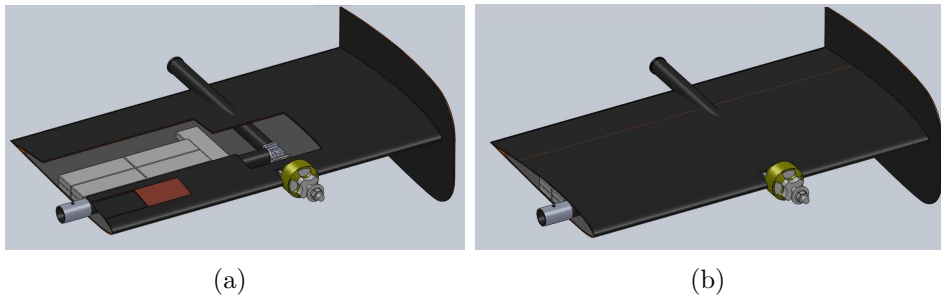


Figure 3.12: CAD model of the wing with regionally cut upper skin to reveal the details (a) and with its final shape (b)

To support the stiffness and lightness of the mechanical structure, carbon composite tubes, which are produced by wrapping woven carbon cloth with epoxy resin, are utilized as the backbone. These tubes have 20 mm of diameter and far more resistance against torsion, bending and crushing when compared with the pultrusion carbon tubes.

There are three main reasons for this. Increase of the diameter from 10 mm to 20 mm with 1 mm material thickness reduces the maximum stress at the surface of the material for approximately 18 times.

Additionally, with the increase of the diameter to 20 mm, the carbon tubes can be fixed in the wing without any interfacing part, directly to the inner surface of the wing skins.

Finally, it is useful to pass the cabling between the wings and the fuselage through the carbon composite spars and the rotating shafts in the wing tilting mechanism (See Fig. 3.19 a in Section 3.2.2). Otherwise, these cables are damaged by the carbon composite skin of the fuselage after several numbers of vertical-horizontal transitions during the operation of SUAVI.

To keep the fuselage both lightweight and stiff against bending and torsion, the front and rear wing tilting mechanisms are also connected through the same type carbon composite tube (Fig. 3.13 a-c). This tube ends at the front wing tilting mechanism, whereas it extends further beyond the rear wing tilting mechanism to provide a stiff support for the vertical stabilizer of the aerial vehicle. This tube is fixed to the outer static structure of the wing-tilting mechanism (Fig. 3.13 b, c). This outer static structure is charged to carry the high torque servo near to the rotating shaft and the needle bearings on which the shaft is rotating, transmit forces from the wings to the body, and carry the aerodynamic cover.

The servo rotates the shaft, on which the wing spars are fixed, through a parallel mechanism with around 100° tilting range. The wing spars are inserted into the shaft and then screwed to it on matching holes with setscrews to keep the wings at correct place and angle. An important detail on this system is the thin rings stuck on the tips of the wing spars. The outer diameter

of the carbon composite tubes vary in the order of some 0.1 mm's.

To prevent the emergence of severe backlash in the wing-shaft joint and to standardize the wing spar-shaft conformity, the tips of the carbon composite tubes are covered with thin aluminum rings having well-known outer diameters. These rings also help preventing crack formation and propagation at the tips of the wing spars that are caused by two point contact loadings between the inner surface of the shaft and outer surface of the wing spars. There are also four aerodynamic cover parts produced from sandwich structured carbon composite material with aramid honeycomb core: the nose, the stern, the lower mid part and the upper mid part.

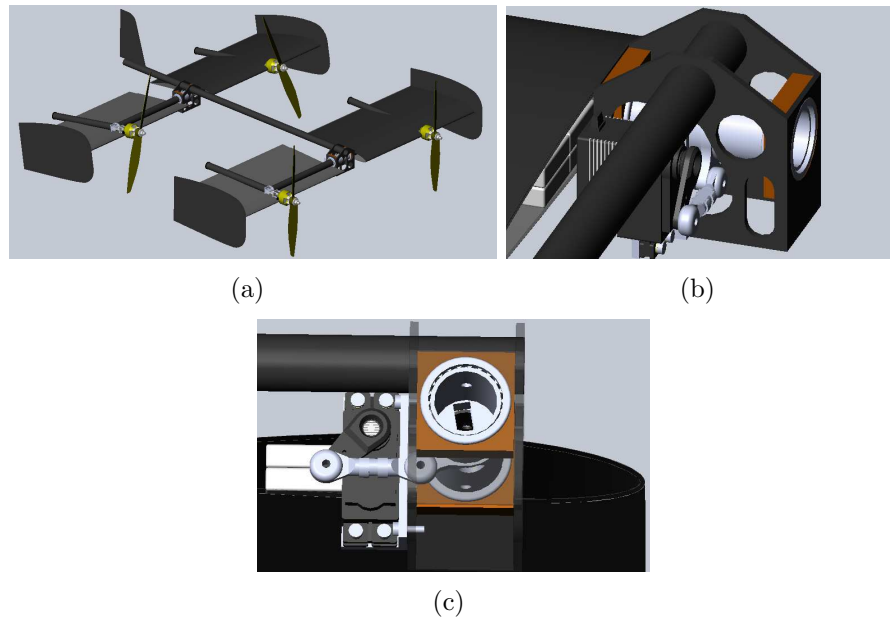


Figure 3.13: CAD model of the body without covering (a), wing-tilting mechanism-carbon pipe connection (b) and the wing-tilting mechanism detail with transparent outer static structure (c)

The CAD model of the improved SUAVI prototype can be seen in (Fig. 3.14).

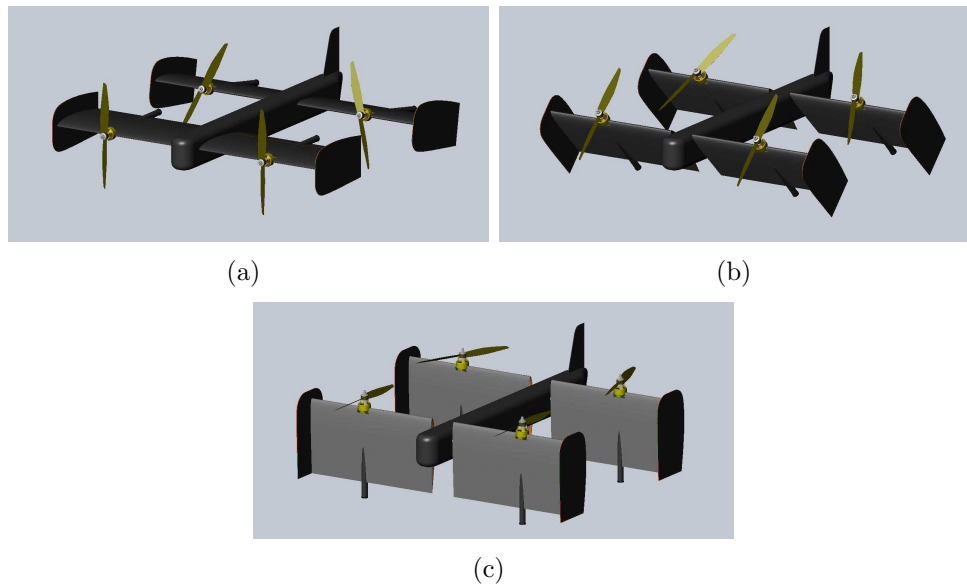


Figure 3.14: CAD model of SUAVI in horizontal (a), transition (b) and vertical (c) flight modes

3.2.2 Production of the Second Prototype

The prototyping first begins with the production of the molds and the aluminum inner parts of SUAVI. The molds are milled from cast aluminum in a CNC milling machine (Fig. 3.15 a, c, d), whereas the inner parts are either milled in the milling machine or lathed in CNC lathe depending on the shape of the parts (Fig. 3.15 b).

For the production of the prototype, sandwich structured carbon composite material with Aramid honeycomb core is utilized. This material is preferred to fulfill the required strength and weight criteria. The carbon fiber material that surrounds the honeycomb is 0-90 plain wave carbon cloth as in the first prototype. The application of the hand lay-up technique is changed slightly to reduce the weight of the carbon composite skins. This process begins with the lay up and wetting of the outer carbon layer on the

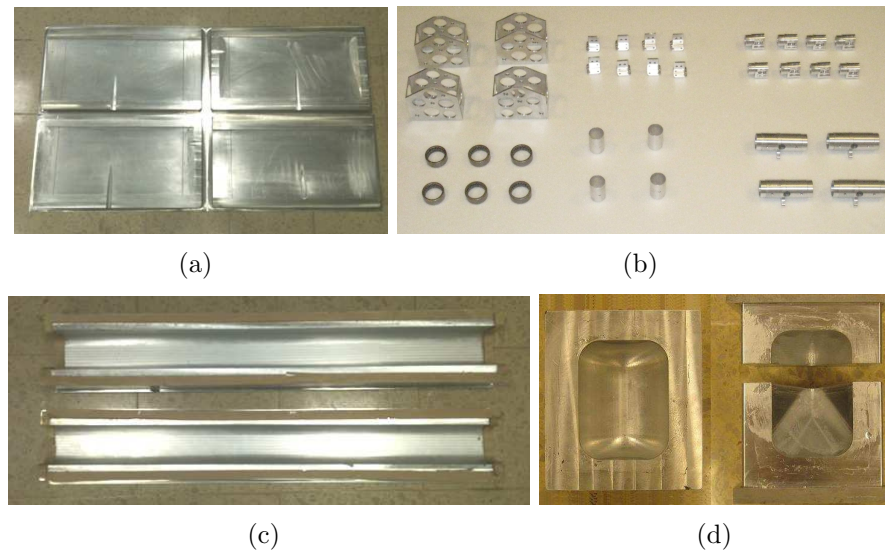


Figure 3.15: Finished molds and inner parts of the wings (a, b) and the molds of the fuselage (c, d)

mold, and then soaking the excess resin, which is a useless weight, using a paper towel. Thereafter, the honeycomb is laid on the outer carbon layer and the second wet carbon layer, that is also cleansed from excess resin is laid on the honeycomb (Fig. 3.16 a). The rest of the vacuum bagging process is the same with the vacuum bagging of the parts in the first prototype.

When curing is completed after 8 hours, the composite part is revealed (Fig. 3.16 b). After the removal of the unwanted parts that are marked using some epoxy resin that cures in the grooves on the molds (Fig. 3.16 c, d), the composite wing skins become ready for assembly to constitute the wings and the fuselage skins become ready for flight.

For the assembly of the wings, a preassembled wing spar, elbow connector and landing arm group with the flight-ready cabling of motor throttle pulse and battery power transmission is fixed on the lower wing skin on the mold with epoxy (Fig. 3.17 a) and supported through epoxy-glass bubble mixture

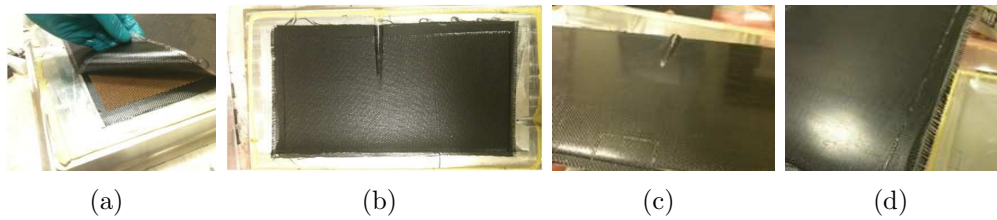


Figure 3.16: Hand lay-up (a), cured skin (c) and lower and the cutting marks on the skins (d, e)

near the tangential connection of the wing skin inner surface (Fig. 3.17 b). Glass bubble is a kind of very tiny glass sphere with around 400 kg/m^3 density that is mixed with some epoxy resin to add some volume to the resin for reducing the density. By applying the epoxy glass bubble mixture, additional strength at the tangential connection is provided through surface increase.

There are two inserts on the wing molds for the precise positioning of these inner parts into the wings. For this reason, the assembly is performed on the molds. Thereafter, the wing spar is drilled on the milling machine again with the wing on the mold (Fig. 3.17 c). The positioning of this drilling operation is crucial, since it determines whether the right and left wings are parallel or not. They must be precisely parallel to prevent any unwanted rotations during the flight due to the geometrical faults. The assembly of the wing is concluded with the joining of the upper skin of the wing (Fig. 3.17 d), the aluminum ring on the wing spar root (Fig. 3.17 e) and the winglet (Fig. 3.17 f).

The assembly of the fuselage begins with the assembly of the wing tilting mechanisms. The shaft that tilts the wings is inserted in the outer static structure through the needle bearings at both sides.

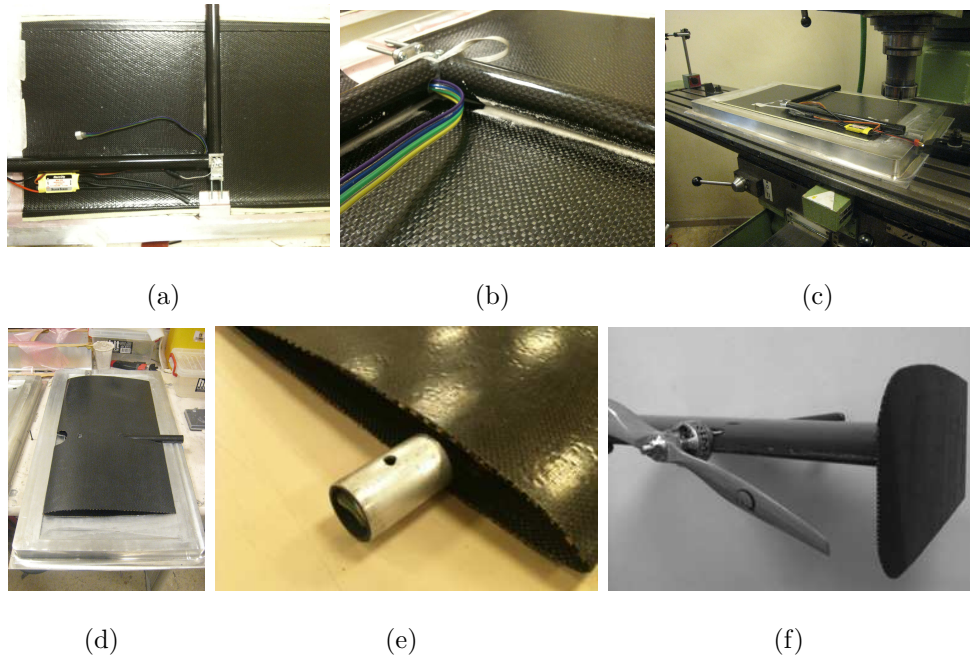


Figure 3.17: Inner parts being attached to the lower wing skin (a), glass-bubble epoxy mixture support (b), drilling of the wing spar root for connection to the wing tilting mechanism (c), joining of the upper skin onto the wing (d), addition of aluminum ring (e) and joining of the winglet (f)

The needle bearings are joined to the outer static structure both using shrink-fit metal-metal connection and gluing small wood parts to widen the connection surface. The high torque wing tilting servo is then assembled on the outer static structure and connected to the shaft via the pushrod (Fig. 3.18 a).

The wing tilting mechanisms are assembled to the carbon composite tube using shrink-fit connection and gluing to constitute the skeleton of the fuselage (Fig. 3.18 a, b). Also the vertical stabilizer is mounted at the back of the fuselage onto the carbon composite tube for strength. At that stage, the fuselage becomes ready for final assembly (Fig. 3.18 c).

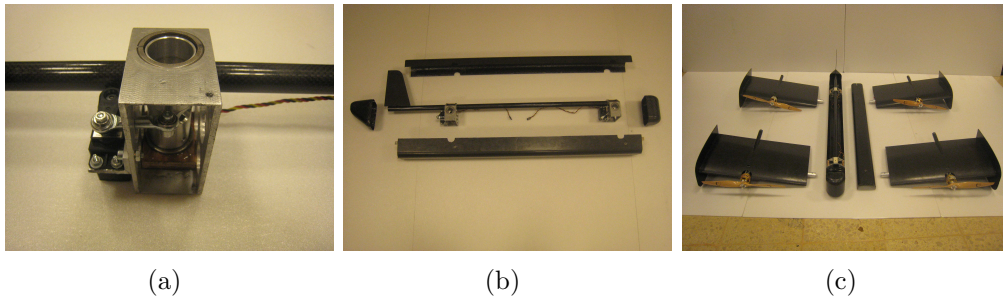


Figure 3.18: Wing tilting mechanism (a), the assembly of the fuselage skeleton (b), final assembly of the fuselage and the wings (c)

With the addition of the electronic control system, sensors and batteries, SUAVI becomes ready for flight (Fig. 3.19 b).

The ready for flight weight of the prototype is 4460 g, in which the body without electronic systems, batteries and motors weighs only 626 g, which is an impressive value when the size, rigidity and the weight of the aluminum mechanisms are taken into account (Fig. 3.20 a, b). It is remarkable that the second prototype is approximately 160 gr lighter than the first one, while incorporating improved strength, more practicality and increased battery capacity to allow longer flight durations.

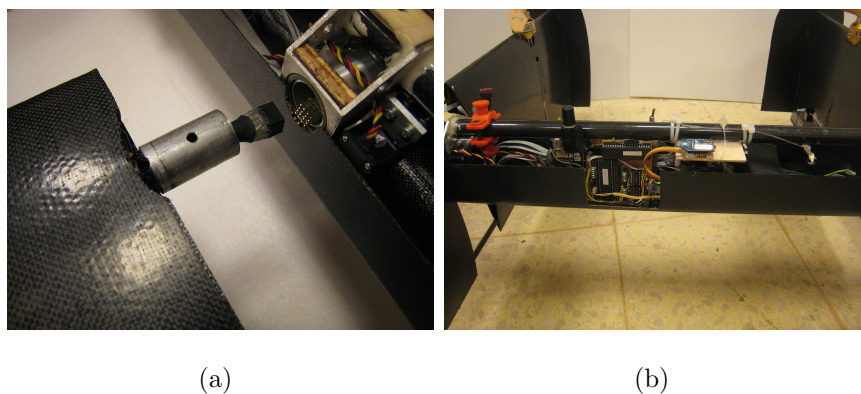
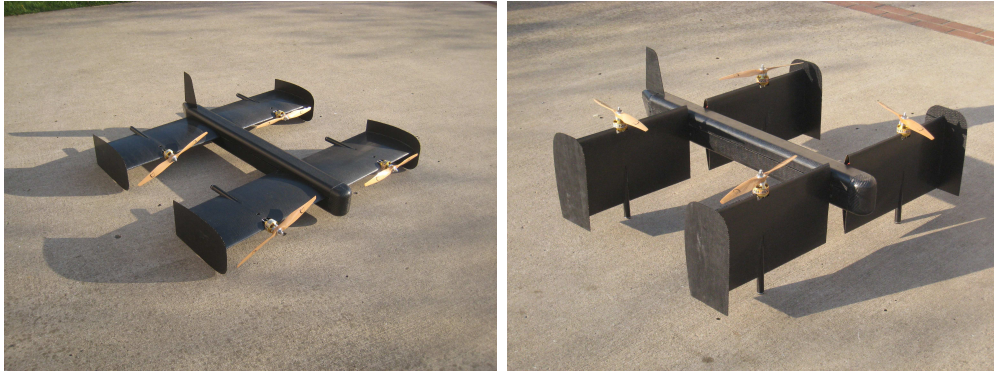


Figure 3.19: Cable connections during the assembly (a) and addition of electronic control system and batteries (b)



(a)

(b)

Figure 3.20: SUAVI prototype in horizontal (a) and vertical (b) flight modes

Chapter 4

4 Dynamical Model and Supervisory Control

Control of a physical system usually starts with some modeling effort. First principles are often used to develop dynamical system models. Models are useful for a variety of reasons. Once a model is developed, it can be simulated to see the response of the system to various input signals. Efficient control system designs can be based on such dynamical models. An automatic control system is required to fly the air vehicle in fully or semi autonomous mode. To achieve accurate trajectory tracking, first a full dynamical model of the aerial vehicle is derived that covers the effects of the aerodynamic forces, disturbances, and the propulsion system. A supervisory control system incorporating both high-level and low-level control is developed.

4.1 Dynamical Model

SUAVI is a highly coupled nonlinear system that changes the flight mode to change the horizontal flight speed. This also alters the control laws and the model significantly due to the fact that the reactions of the air vehicle to motor thrusts and control surface deflections, and the forces and moments on the air vehicle change dramatically with the flight mode.

To develop and test the flight control system in simulation environment without damaging the air vehicle, the dynamical model of the system needs to be developed. Through simulations, the response of the system to various control inputs can be estimated in a more effective manner. Additionally, various control methods can be tested in both linear and nonlinear frameworks.

4.1.1 Hybrid Frame

For the derivation of the dynamical models for air vehicles, it is a common practice to express positional dynamics wrt. a fixed world coordinate frame and the rotational dynamics wrt. a body fixed frame attached to the vehicle. This is called hybrid frame [154].

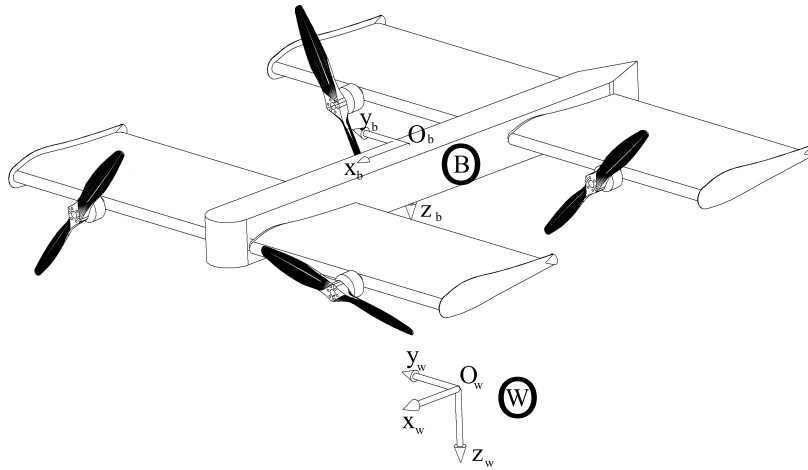


Figure 4.1: Coordinate frames of the aerial vehicle

Two reference frames are utilized in the mathematical modeling of the aerial vehicle, that are also depicted in Fig. 4.1. They are

- Earth frame $W : (O_w, x_w, y_w, z_w)$
- Body frame $B : (O_b, x_b, y_b, z_b)$

In the earth fixed inertial reference frame (world frame) x_w is directed northwards, y_w is directed eastwards, z_w is directed downwards and O_w is the origin of the world frame. Similarly, in the body frame, x_b is directed to the front of the vehicle, y_b is directed to the right of the vehicle, z_b is directed downwards and O_b is the origin on the center of mass of the aerial vehicle.

The position and linear velocity of the vehicle's center of mass in the world frame are expressed as

$$P_w = [X, Y, Z]^T, \quad V_w = \dot{P}_w = [\dot{X}, \dot{Y}, \dot{Z}]^T \quad (4.1)$$

Vehicle's attitude and its time derivative in the world frame are defined as

$$\alpha_w = [\phi, \theta, \psi]^T, \quad \Omega_w = \dot{\alpha}_w = [\dot{\phi}, \dot{\theta}, \dot{\psi}]^T \quad (4.2)$$

ϕ , θ and ψ are named roll, pitch and yaw angles, respectively. The orientation of the body frame wrt. the world frame is expressed by the rotation matrix

$$R_{wb}(\phi, \theta, \psi) = R_z(\psi)R_y(\theta)R_x(\phi) = \begin{bmatrix} c_\psi c_\theta & s_\phi s_\theta c_\psi - c_\phi s_\psi & c_\phi s_\theta c_\psi + s_\phi s_\psi \\ s_\psi c_\theta & s_\phi s_\theta s_\psi + c_\phi c_\psi & c_\phi s_\theta s_\psi - s_\phi c_\psi \\ -s_\theta & s_\phi c_\theta & c_\phi c_\theta \end{bmatrix} \quad (4.3)$$

The transformation of linear velocities between world and body frames is

formulated as

$$V_b = \begin{bmatrix} v_x \\ v_y \\ v_z \end{bmatrix} = R_{wb}^T(\phi, \theta, \psi) \cdot V_w = R_{bw}(\phi, \theta, \psi) \cdot V_w \quad (4.4)$$

The relation between the angular velocity of the vehicle and the time derivative of the attitude angles is given by the following transformation

$$\Omega_b = \begin{bmatrix} p \\ q \\ r \end{bmatrix} = E(\phi, \theta) \cdot \Omega_w \quad (4.5)$$

where E is the velocity transformation matrix and defined as

$$E(\phi, \theta) = \begin{bmatrix} 1 & 0 & -s_\theta \\ 0 & c_\phi & s_\phi c_\theta \\ 0 & -s_\phi & c_\phi c_\theta \end{bmatrix} \quad (4.6)$$

4.1.2 Newton-Euler Formulation

The equations of a 6 DOF rigid body can be derived by several methods. Newton-Euler formulation is utilized to derive the full mathematical model of SUAVI.

Considering the aerial vehicle as a rigid body and employing a hybrid frame, the dynamics of an aerial vehicle can be formed as

$$\begin{bmatrix} mI_{3 \times 3} & 0_{3 \times 3} \\ 0_{3 \times 3} & I_b \end{bmatrix} \begin{bmatrix} \dot{V}_w \\ \dot{\Omega}_b \end{bmatrix} + \begin{bmatrix} 0 \\ \Omega_b \times (I_b \Omega_b) \end{bmatrix} = \begin{bmatrix} F_t \\ M_t \end{bmatrix} \quad (4.7)$$

where the subscripts w and b express the vector and matrix quantities in world and body frames, respectively. m denotes the mass and I_b denotes the vehicle's inertia matrix expressed in body frame. $I_{3 \times 3}$ and $0_{3 \times 3}$ matrices indicate 3×3 identity and zero matrices respectively. The left hand side of Eqn. (4.7) is standard for many aerial vehicle types, however total force and moment terms, F_t and M_t , differ for different aerial vehicle types.

Note that for a quad tilt-wing aerial vehicle, the terms F_t and M_t are functions of the motor thrusts, forces on the wings and the fuselage, and also the wing angle of attacks and they act on the vehicle's center of gravity. These forces and torques are depicted as in Fig. 4.2.

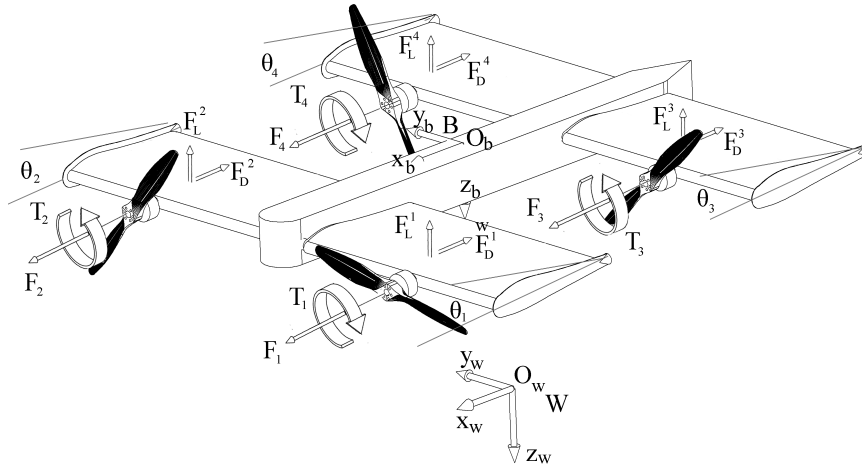


Figure 4.2: External forces and torques acting on the vehicle

The total external force F_t consists of the motor thrusts F_{th} , aerodynamic forces on the wings F_w , gravity force on the vehicle F_g and external disturbances such as winds and gusts F_d . These forces are expressed in the body frame and have to be transformed by R_{wb} to be expressed in the world frame

as follows

$$F_t = R_{wb}(F_{th} + F_w + F_g + F_d) \quad (4.8)$$

where

$$F_{th} = \begin{bmatrix} c_{\theta_1} & c_{\theta_2} & c_{\theta_3} & c_{\theta_4} \\ 0 & 0 & 0 & 0 \\ -s_{\theta_1} & -s_{\theta_2} & -s_{\theta_3} & -s_{\theta_4} \end{bmatrix} \begin{bmatrix} k\omega_1^2 \\ k\omega_2^2 \\ k\omega_3^2 \\ k\omega_4^2 \end{bmatrix}$$

$$F_w = \begin{bmatrix} (F_D^1(\theta_1, v_x, v_z) + F_D^2(\theta_2, v_x, v_z) + F_D^3(\theta_3, v_x, v_z) + F_D^4(\theta_4, v_x, v_z)) \\ 0 \\ (F_L^1(\theta_1, v_x, v_z) + F_L^2(\theta_2, v_x, v_z) + F_L^3(\theta_3, v_x, v_z) + F_L^4(\theta_4, v_x, v_z)) \end{bmatrix}$$

and

$$F_g = \begin{bmatrix} -s_\theta \\ s_\phi c_\theta \\ c_\phi c_\theta \end{bmatrix} mg$$

In all these equations, s_β and c_β are abbreviations for $\sin(\beta)$ and $\cos(\beta)$ respectively and θ_i denotes wing angles wrt. the body. Note that the motor thrusts are modeled as

$$F_i = k\omega_i^2 \quad (4.9)$$

where ω_i is the rotor rotational speed [155] and this relation is also experimentally verified in Fig. 2.3.

To simplify the design of the aerial vehicle, left and right wings both at the back and at the front are tilted together, leading to the relations $\theta_1 = \theta_2$ and $\theta_3 = \theta_4$. The lift forces $F_L^i(\theta_i, v_x, v_z)$ and the drag forces $F_D^i(\theta_i, v_x, v_z)$ are functions of linear velocities v_x and v_z , and the wing angle of attacks θ_i ,

namely

$$\begin{bmatrix} F_D^i \\ 0 \\ F_L^i \end{bmatrix} = R(\theta_i - \alpha_i) \begin{bmatrix} -\frac{1}{2}c_D(\alpha_i)\rho Av_\alpha^2 \\ 0 \\ -\frac{1}{2}c_L(\alpha_i)\rho Av_\alpha^2 \end{bmatrix} \quad (4.10)$$

where

$$v_\alpha = \sqrt{v_x^2 + v_z^2}$$

$$\alpha_i = \theta_i - (-\text{atan2}(v_z, v_x))$$

In these equations, ρ is the air density, A is the wing planform area, v_α is the air flow velocity and α_i is the effective angle of attack of the wing wrt. the air flow as depicted in Fig. 4.3.

$R(\theta_i - \alpha_i)$ is the rotation matrix for the rotation around y axis that decomposes the forces on the wings to the body axes. (4.10). The lift coefficient $c_L(\alpha_i)$ and drag coefficient $c_D(\alpha_i)$ are obtained from airfoil models [149, 150]. (see [156] for details)

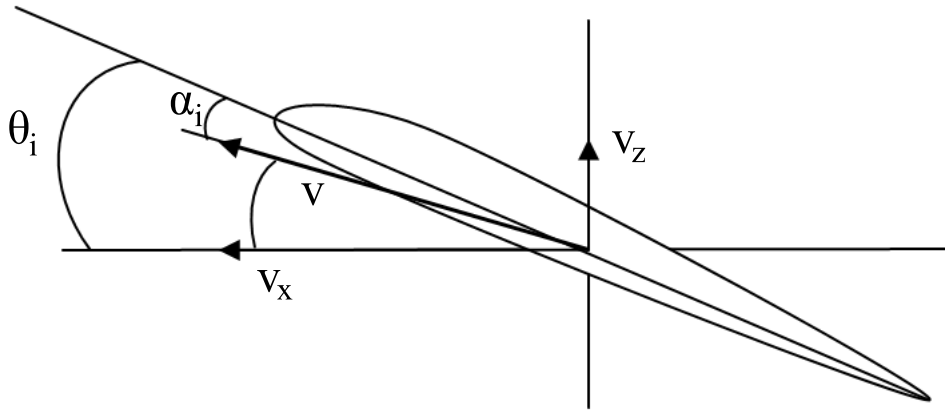


Figure 4.3: Effective angle of attack α_i

The total torque M_t consists of the torques created by the rotors M_{th} ,

torques created by the aerodynamic forces produced by the wings M_w , torques created by the gyroscopic effects of the propellers M_{gyro} and torques due to the external disturbances M_d , namely

$$M_t = M_{th} + M_w + M_{gyro} + M_d \quad (4.11)$$

where

$$M_{th} = \begin{bmatrix} l_s s_{\theta_1} - c_{\theta_1} \lambda_1 & -l_s s_{\theta_2} - c_{\theta_2} \lambda_2 & l_s s_{\theta_3} - c_{\theta_3} \lambda_3 & -l_s s_{\theta_4} - c_{\theta_4} \lambda_4 \\ l_l s_{\theta_1} & l_l s_{\theta_2} & -l_l s_{\theta_3} & -l_l s_{\theta_4} \\ l_s c_{\theta_1} + s_{\theta_1} \lambda_1 & -l_s c_{\theta_2} + s_{\theta_2} \lambda_2 & l_s c_{\theta_3} + s_{\theta_3} \lambda_3 & -l_s c_{\theta_4} + s_{\theta_4} \lambda_4 \end{bmatrix} \begin{bmatrix} k\omega_1^2 \\ k\omega_2^2 \\ k\omega_3^2 \\ k\omega_4^2 \end{bmatrix},$$

$$M_w = \begin{bmatrix} l_s(F_L^1(\theta_1, v_x, v_z) - F_L^2(\theta_2, v_x, v_z) + F_L^3(\theta_3, v_x, v_z) - F_L^4(\theta_4, v_x, v_z)) \\ l_l(F_L^1(\theta_1, v_x, v_z) + F_L^2(\theta_2, v_x, v_z) - F_L^3(\theta_3, v_x, v_z) - F_L^4(\theta_4, v_x, v_z)) \\ l_s(-F_D^1(\theta_1, v_x, v_z) + F_D^2(\theta_2, v_x, v_z) - F_D^3(\theta_3, v_x, v_z) + F_D^4(\theta_4, v_x, v_z)) \end{bmatrix}$$

and

$$M_{gyro} = \sum_{i=1}^4 J_{prop} [\eta_i \Omega_b \times \begin{bmatrix} c_{\theta_i} \\ 0 \\ -s_{\theta_i} \end{bmatrix} \omega_i]$$

In these expressions, l_s and l_l denote the spanwise and longitudinal distances between the rotors and the center of mass of the vehicle, respectively. J_{prop} is the rotational inertia of the rotors about their rotation axes and $\eta_{(1,2,3,4)} = 1, -1, -1, 1$. The rotor torques are modeled as

$$T_i = \lambda_i k \omega_i^2 \quad (4.12)$$

where λ_i are torque/force ratios. For clockwise rotating propellers, $\lambda_{2,3} = -\lambda$ whereas for counterclockwise rotating propellers $\lambda_{1,4} = \lambda$. In the literature it is reported that λ for such kind of propellers are 0.01-0.05 [154].

Note that the sum of torques created by the rotors result in a roll moment in horizontal flight mode ($\theta_{1,2,3,4} = 0$) and in a yaw moment in vertical flight mode ($\theta_{1,2,3,4} = \pi/2$).

Utilizing vector-matrix notation and including external disturbances, the dynamics of SUAVI can be rewritten in a more compact form as

$$M\dot{\zeta} + C(\zeta)\zeta = G + O(\zeta)\omega + E(\xi)\omega^2 + W(\zeta) + D(\zeta, \xi) \quad (4.13)$$

where $\zeta = [\dot{X}, \dot{Y}, \dot{Z}, p, q, r]^T$ is the generalized velocity vector and the vector $\xi = [X, Y, Z, \phi, \theta, \psi]^T$ states the position and the orientation of the vehicle expressed in the world frame. The relation between ζ and ξ can be formulated as

$$\dot{\xi} = J\zeta \Rightarrow \begin{bmatrix} \dot{X} \\ \dot{Y} \\ \dot{Z} \\ \dot{\phi} \\ \dot{\theta} \\ \dot{\psi} \end{bmatrix} = \begin{bmatrix} 1 & 0 & 0 & 0 & 0 & 0 \\ 0 & 1 & 0 & 0 & 0 & 0 \\ 0 & 0 & 1 & 0 & 0 & 0 \\ 0 & 0 & 0 & 1 & s_\phi t_\theta & c_\phi t_\theta \\ 0 & 0 & 0 & 0 & c_\phi & -s_\phi \\ 0 & 0 & 0 & 0 & s_\phi/c_\theta & c_\phi/c_\theta \end{bmatrix} \begin{bmatrix} \dot{X} \\ \dot{Y} \\ \dot{Z} \\ p \\ q \\ r \end{bmatrix} \quad (4.14)$$

It is worth to note that the lower-right hand side 3×3 part of this Jacobian matrix is the inverse of the E matrix, that is defined in Eqn. 4.6.

The inertia matrix M , the Coriolis-centripetal matrix $C(\zeta)$, the gravity

term G , and the gyroscopic term $O(\zeta)\omega$, are defined as

$$M = \begin{bmatrix} mI_{3 \times 3} & 0_{3 \times 3} \\ 0_{3 \times 3} & \text{diag}(I_{xx}, I_{yy}, I_{zz}) \end{bmatrix} \quad (4.15)$$

$$C(\zeta) = \begin{bmatrix} 0 & 0 & 0 & 0 & 0 & 0 \\ 0 & 0 & 0 & 0 & 0 & 0 \\ 0 & 0 & 0 & 0 & 0 & 0 \\ 0 & 0 & 0 & 0 & I_{zz}r & -I_{yy}q \\ 0 & 0 & 0 & -I_{zz}r & 0 & I_{xx}p \\ 0 & 0 & 0 & I_{yy}q & -I_{xx}p & 0 \end{bmatrix} \quad (4.16)$$

$$G = [0, 0, mg, 0, 0, 0]^T \quad (4.17)$$

$$O(\zeta)\omega = J_{prop} \left(\begin{array}{c} 0_{3 \times 1} \\ \sum_{i=1}^4 [\eta_i \Omega_b \times \begin{bmatrix} c_{\theta_i} \\ 0 \\ -s_{\theta_i} \end{bmatrix} \omega_i] \end{array} \right) \quad (4.18)$$

where I_{xx} , I_{yy} and I_{zz} are the moments of inertia of the aerial vehicle around its body frame axes.

System actuator vector, $E(\xi)\omega^2$, is assigned as

$$E(\xi)\omega^2 = \begin{bmatrix} R_{wb}F_{th} \\ M_{th} \end{bmatrix} = \begin{bmatrix} (c_\phi s_\theta c_\psi + s_\phi s_\psi)u_v + c_\psi c_\theta u_h \\ (c_\phi s_\theta s_\psi - s_\phi c_\psi)u_v + s_\psi c_\theta u_h \\ c_\phi c_\theta u_v - s_\theta u_h \\ (l_s s_{\theta_f} - c_{\theta_f} \lambda)u_{f_{dif}} + (l_s s_{\theta_r} + c_{\theta_r} \lambda)u_{r_{dif}} \\ [s_{\theta_f} u_{f_{sum}} - s_{\theta_r} u_{r_{sum}}]l_l \\ (l_s c_{\theta_f} + s_{\theta_f} \lambda)u_{f_{dif}} + (l_s c_{\theta_r} - s_{\theta_r} \lambda)u_{r_{dif}} \end{bmatrix} \quad (4.19)$$

where $u_{f_{dif}} = k(\omega_1^2 - \omega_2^2)$, $u_{r_{dif}} = k(\omega_3^2 - \omega_4^2)$, $u_{f_{sum}} = k(\omega_1^2 + \omega_2^2)$, $u_{r_{sum}} = k(\omega_3^2 + \omega_4^2)$, $u_v = -s_{\theta_f}u_{f_{sum}} - s_{\theta_r}u_{r_{sum}}$, $u_h = c_{\theta_f}u_{f_{sum}} + c_{\theta_r}u_{r_{sum}}$, $\theta_f = \theta_1 = \theta_2$ and $\theta_r = \theta_3 = \theta_4$.

Lift and drag forces that are generated by the wings and the resulting moments due to these forces are defined as

$$W(\zeta) = \begin{bmatrix} R_{wb} \begin{bmatrix} F_D^1 + F_D^2 + F_D^3 + F_D^4 \\ 0 \\ F_L^1 + F_L^2 + F_L^3 + F_L^4 \end{bmatrix} \\ l_s(F_L^1 - F_L^2 + F_L^3 - F_L^4) \\ l_l(F_L^1 + F_L^2 - F_L^3 - F_L^4) \\ l_s(-F_D^1 + F_D^2 - F_D^3 + F_D^4) \end{bmatrix} \quad (4.20)$$

The model of SUAVI becomes a quadrotor model when $(\theta_{1,2,3,4} = \pi/2)$. The inertia matrix M , the Coriolis-centripetal matrix $C(\zeta)$ and the gravity vector G are irrelevant with the wing angles, so they remain inert. However, when the wings are tilted vertically, some items in the gyroscopic term $O(\zeta)\omega$, system actuator vector $E(\xi)\omega^2$, and aerodynamic force vector $W(\zeta)$ drop.

In this configuration, the wings do not generate any lift force but generate severe drag forces. The motor thrusts behave as lift sources only due to their downward slipstream in vertical mode. The resulting dynamic model written for the vertical flight mode of SUAVI is similar to the quadrotor models existing in the literature ([154]).

For the vertical flight mode of SUAVI, the *sin* and *cos* terms cause the gyroscopic term $O(\zeta)\omega$ in Eqn. (4.18), the system actuator vector $E(\xi)\omega^2$ in Eqn. (4.19) and the aerodynamic force vector $W(\zeta)$ in Eqn. (4.20) to be

simplified as

$$O(\zeta)\omega = J_{prop} \left(\begin{array}{c} 0_{3 \times 1} \\ \sum_{i=1}^4 [\eta_i \Omega_b \times \begin{bmatrix} 0 \\ 0 \\ -1 \end{bmatrix} \omega_i] \end{array} \right) = \begin{bmatrix} 0 & 0 & 0 & 0 \\ 0 & 0 & 0 & 0 \\ 0 & 0 & 0 & 0 \\ -q & q & -q & q \\ p & -p & p & -p \\ 0 & 0 & 0 & 0 \end{bmatrix} \begin{bmatrix} \omega_1 \\ \omega_2 \\ \omega_3 \\ \omega_4 \end{bmatrix} \quad (4.21)$$

$$E(\xi)\omega^2 = \begin{bmatrix} (-c_\phi s_\theta c_\psi - s_\phi s_\psi)u_1 \\ (-c_\phi s_\theta s_\psi + s_\phi c_\psi)u_1 \\ -c_\phi c_\theta u_1 \\ u_2 \\ u_3 \\ u_4 \end{bmatrix} \quad (4.22)$$

$$W(\zeta) = \begin{bmatrix} R_{wb} \begin{bmatrix} F_D^1 + F_D^2 + F_D^3 + F_D^4 \\ 0 \\ 0 \\ 0 \\ 0 \end{bmatrix} \\ l_s(-F_D^1 + F_D^2 - F_D^3 + F_D^4) \end{bmatrix} \quad (4.23)$$

where u_i are the virtual control inputs and can be defined as

$$u_1 = k(\omega_1^2 + \omega_2^2 + \omega_3^2 + \omega_4^2) \quad (4.24)$$

$$u_2 = l_s k((\omega_1^2 + \omega_3^2) - (\omega_2^2 + \omega_4^2)) \quad (4.25)$$

$$u_3 = l_l k((\omega_1^2 + \omega_2^2) - (\omega_3^2 + \omega_4^2)) \quad (4.26)$$

$$u_4 = k\lambda(\omega_1^2 - \omega_2^2 - \omega_3^2 + \omega_4^2) \quad (4.27)$$

Consequently, position and attitude dynamics of the aerial vehicle in quadrotor mode are expressed as follows:

$$\ddot{X} = (-c_\phi s_\theta c_\psi - s_\phi s_\psi)u_1 + c_\psi c_\theta(F_D^1 + F_D^2 + F_D^3 + F_D^4)$$

$$\ddot{Y} = (-c_\phi s_\theta s_\psi + s_\phi c_\psi)u_1 + s_\psi c_\theta(F_D^1 + F_D^2 + F_D^3 + F_D^4)$$

$$\ddot{Z} = -c_\phi c_\theta u_1 + g - s_\theta(F_D^1 + F_D^2 + F_D^3 + F_D^4)$$

$$\dot{p} = \frac{u_2}{I_{xx}} + \frac{I_{yy} - I_{zz}}{I_{xx}}qr - \frac{J_{prop}}{I_{xx}}q\omega_p$$

$$\dot{q} = \frac{u_3}{I_{yy}} + \frac{I_{zz} - I_{xx}}{I_{yy}}pr + \frac{J_{prop}}{I_{yy}}p\omega_p$$

$$\dot{r} = \frac{u_4}{I_{zz}} + \frac{I_{xx} - I_{yy}}{I_{zz}}pq + \frac{J_{prop}}{I_{zz}}r\omega_p + l_s(-F_D^1 + F_D^2 - F_D^3 + F_D^4) \quad (4.28)$$

The last three rows of the dynamics of SUAVI in quadrotor mode can be expressed in the earth frame. To this end, Eqn. (4.5) and its time derivative can be employed, i.e.

$$\Omega_b = E(\phi, \theta) \cdot \Omega_w \Rightarrow \dot{\Omega}_b = \dot{E}\Omega_w + E\dot{\Omega}_w \quad (4.29)$$

In steady hover conditions, the following assumptions are valid:

$$\phi, \theta, \psi \rightarrow 0 \Rightarrow E(\phi, \theta) = \begin{bmatrix} 1 & 0 & -s_\theta \\ 0 & c_\phi & s_\phi c_\theta \\ 0 & -s_\phi & c_\phi c_\theta \end{bmatrix} = I \quad (4.30)$$

$$\dot{\phi}, \dot{\theta}, \dot{\psi} \rightarrow 0 \Rightarrow \begin{bmatrix} \dot{\phi} \\ \dot{\theta} \\ \dot{\psi} \end{bmatrix} = \begin{bmatrix} 0 \\ 0 \\ 0 \end{bmatrix} \quad (4.31)$$

As a result,

$$\begin{bmatrix} \dot{p} \\ \dot{q} \\ \dot{r} \end{bmatrix} = \dot{E} \begin{bmatrix} \dot{\phi} \\ \dot{\theta} \\ \dot{\psi} \end{bmatrix} + I \begin{bmatrix} \ddot{\phi} \\ \ddot{\theta} \\ \ddot{\psi} \end{bmatrix} \Rightarrow \begin{bmatrix} \dot{p} \\ \dot{q} \\ \dot{r} \end{bmatrix} \approx \begin{bmatrix} \ddot{\phi} \\ \ddot{\theta} \\ \ddot{\psi} \end{bmatrix} \quad (4.32)$$

The term $l_s(-F_D^1 + F_D^2 - F_D^3 + F_D^4)$ in the last equation of (4.28) can be dropped due to the symmetry of the vehicle. Consequently, in steady hover conditions the last three rows of Eqn. (4.28) can also be expressed as

$$\begin{aligned} \ddot{\phi} &= \frac{u_2}{I_{xx}} + \frac{I_{yy} - I_{zz}}{I_{xx}} qr - \frac{J_{prop}}{I_{xx}} q\omega_p \\ \ddot{\theta} &= \frac{u_3}{I_{yy}} + \frac{I_{zz} - I_{xx}}{I_{yy}} pr + \frac{J_{prop}}{I_{yy}} p\omega_p \\ \ddot{\psi} &= \frac{u_4}{I_{zz}} + \frac{I_{xx} - I_{yy}}{I_{zz}} pq + \frac{J_{prop}}{I_{zz}} r\omega_p \end{aligned} \quad (4.33)$$

The parameters of the vehicle used in mathematical modeling are revealed in Table 4.1.

4.2 Disturbance Modeling

The effect of aerodynamic disturbances such as winds on the aerial vehicle flight control can be significant, leading to instabilities. The effects of wind can be modeled and the generalized wind forces can be estimated to reject these external disturbances. In this way, the robustness of the positioning against the disturbances can be improved.

Table 4.1: Modeling parameters

Symbol	Description	Dimensions/Magnitude
m	mass	4.5 kg
l_s	rotor distance to cog along y axis	0.3 m
l_l	rotor distance to cog along x axis	0.3 m
I_{xx}	moment of inertia along x axis	0.405 kgm^2
I_{yy}	moment of inertia along y axis	0.405 kgm^2
I_{zz}	moment of inertia along z axis	0.72 kgm^2
$\lambda_{1,4}$	torque/force ratio	0.01 Nm/N
$\lambda_{2,3}$	torque/force ratio	-0.01 Nm/N

For the modeling of the wind, Dryden wind-gust model is utilized [157]. This model defines the wind and gusts as a summation of sinusoidal excitations as

$$v_\omega(t) = v_\omega^0 + \sum_{i=1}^n a_i \sin(\Omega_i t + \varphi_i) \quad (4.34)$$

where $v_\omega(t)$ is the time dependent wind vector, Ω_i are randomly selected frequencies in the range of 0.1 to 1.5 rad/s , φ_i are phase shifts, n is the number of sinusoids, a_i are the amplitudes of these sinusoids and v_ω^0 is the static wind vector.

a_i are defined as $a_i = \sqrt{\Delta\Omega_i \Phi(\Omega_i)}$ where $\Delta\Omega_i$ are the frequency intervals and $\Phi(\Omega_i)$ are the power spectral densities. The power spectral density for vertical and horizontal winds are different and expressed as

$$\Phi_h(\Omega) = \sigma_h^2 \frac{2L_h}{\pi} \frac{1}{1 + (L_h\Omega)^2} \quad (4.35)$$

$$\Phi_v(\Omega) = \sigma_v^2 \frac{2L_v}{\pi} \frac{1 + 3(L_v\Omega)^2}{(1 + (L_v\Omega)^2)^2} \quad (4.36)$$

where σ_h and σ_v are horizontal and vertical turbulence intensities respectively. L_h and L_v are horizontal and vertical gust length scales. These expressions are valid for altitudes up to 1000 feet above sea level [30].

The relations between L_h and L_v , and σ_h and σ_v are dependent on the altitude as observed in the following equations:

$$\frac{L_h}{L_v} = \frac{1}{(0.177 + 0.000823Z)^{1.2}} \quad (4.37)$$

$$\frac{\sigma_h}{\sigma_v} = \frac{1}{(0.177 + 0.000823Z)^{0.4}} \quad (4.38)$$

Generalized disturbance forces are calculated by multiplying the square of these wind velocities with the corresponding aerodynamic drag coefficients and integrated into the dynamic model in Eqn. (4.13) as external disturbances $D(\zeta, \xi)$.

4.3 Disturbance Observer

For the control system, a disturbance observer [158] is designed to estimate the total disturbance acting on SUAVI, that incorporates the external disturbances, nonlinear terms and parametric uncertainties in the dynamics.

The inertia matrix of the aerial vehicle can be written as,

$$M = M_{nom} + \tilde{M}$$

where M_{nom} is the nominal inertia matrix defined as $M_{nom} = \text{diag}(m, m, m, I_{xx}, I_{yy}, I_{zz})$ and (\tilde{M}) is the variation of the actual inertia matrix from the nominal values.

The compact form of the dynamics of SUAVI in Eqn. (4.13) can be rewritten in terms of the nominal inertia matrix as

$$M_{nom}\dot{\zeta} = f + \tau_{dist} \quad (4.39)$$

where f presents the actuator inputs and τ_{dist} refers to the total disturbance as

$$f = E(\xi)\omega^2$$

$$\tau_{dist} = -\tilde{M}\dot{\zeta} - C(\zeta)\zeta + G + O(\zeta)\Omega + W(\zeta) + D(\zeta, \xi) \quad (4.40)$$

Note that τ_{dist} contains nonlinear terms and the parametric uncertainties in the dynamics in addition to the external disturbances like winds.

Equation (4.39) incorporates first order differential equations of the form

$$M_{nom_i}\dot{\zeta}_i = f_i + \tau_{dist_i}, \quad i = 1, \dots, 6 \quad (4.41)$$

Taking the Laplace transform these equations become

$$M_{nom_i}s\zeta_i(s) = f_i(s) + \tau_{dist_i}(s) \quad (4.42)$$

and τ_{dist_i} can be extracted as

$$\tau_{dist_i}(s) = M_{nom_i}s\zeta_i(s) - f_i(s) \quad (4.43)$$

For the $s\zeta_i(s)$ term in Eqn. (4.43), future values of ζ are required, which are not available in practice. Therefore, this equation is not applicable. However, both sides of this equation can be low-pass filtered by multiplying

with $G(s) = \frac{g}{s+g}$ as

$$G(s)\tau_{dist_i}(s) = M_{nom_i}sG(s)\zeta_i(s) - G(s)f_i(s) \quad (4.44)$$

where $sG(s)$ can be manipulated as

$$sG(s) = s\frac{g}{s+g} = g\left(1 - \frac{g}{s+g}\right) = g(1 - G(s)) \quad (4.45)$$

The term $G(s)\tau_{dist_i}(s)$ can be denoted by $\hat{\tau}_{dist_i}(s)$, which becomes the estimated disturbance. Finally, Eqn. (4.43) becomes

$$\hat{\tau}_{dist_i}(s) = -G(s)f_i(s) - gM_{nom}G(s)\zeta_i(s) + gM_{nom}\zeta_i(s) \quad (4.46)$$

which is applicable. When this estimated disturbance is subtracted from the input term, Eqn. (4.42) becomes

$$M_{nom_i}s\zeta_i(s) = f_i(s) + (1 - G(s))\tau_{dist_i}(s) \quad (4.47)$$

In Eqn. (4.47), at low frequencies $G(s) \approx 1$ and the total disturbance on the system is omitted. Hence, the full dynamics of the aerial vehicle in Eqn. (4.13) is reduced to a linear model defined in terms of nominal parameters as follows:

$$M_{nom_i}\dot{\zeta}_i = f_i \quad (4.48)$$

To estimate the total disturbance, a closed-loop disturbance observer is implemented utilizing Eqn. (4.46). The block diagram of the dynamical model of the aerial vehicle with the implemented disturbance observer is depicted in Fig. 4.4.

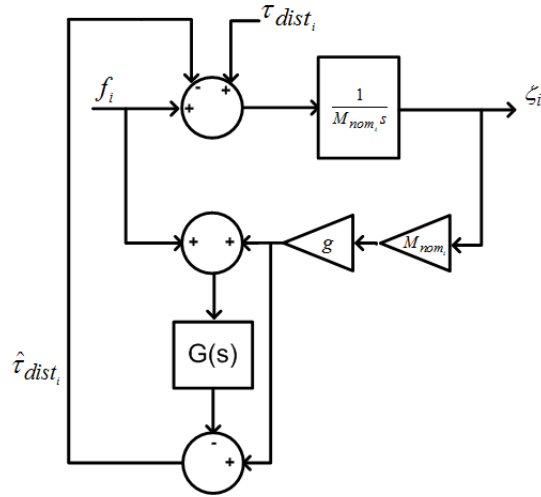


Figure 4.4: Block diagram of the closed loop disturbance observer

4.4 Supervisory Flight Control System

Complexity is a very common problem in control systems. To cope with this problem, decomposition of complex missions into subtasks and combination of individual solutions through hierarchical control is very crucial. SUAVI is a complex multiple-input multiple-output (MIMO) system that suffers from internal and external uncertainties during flight and is designed to perform complex missions in a safe and efficient manner using a variety of sensors and actuators.

The supervisory control system is developed that consists of a high-level controller for GPS and/or vision based position control and low-level controllers for attitude stabilization. (Fig. 4.5).

SUAVI has two fundamental flight modes, which are the vertical and horizontal flights. The wings are vertical during takeoff, hovering and landing and tilted when forward motion is required. The tilt angle is determined based on the requirements of the present flight speed. The control system

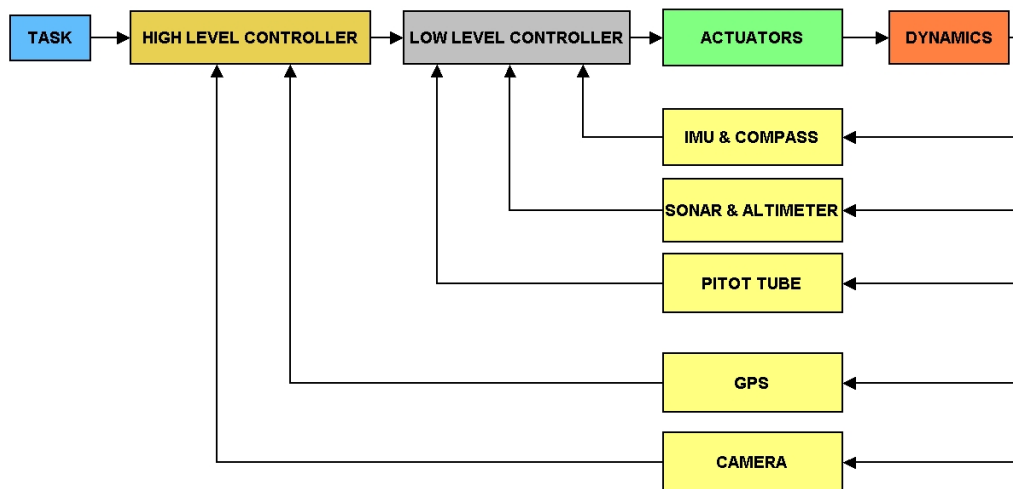


Figure 4.5: Supervisory control architecture

needs to handle all of these factors for accomplishing the stable flight and successful reference tracking (Fig. 4.6).

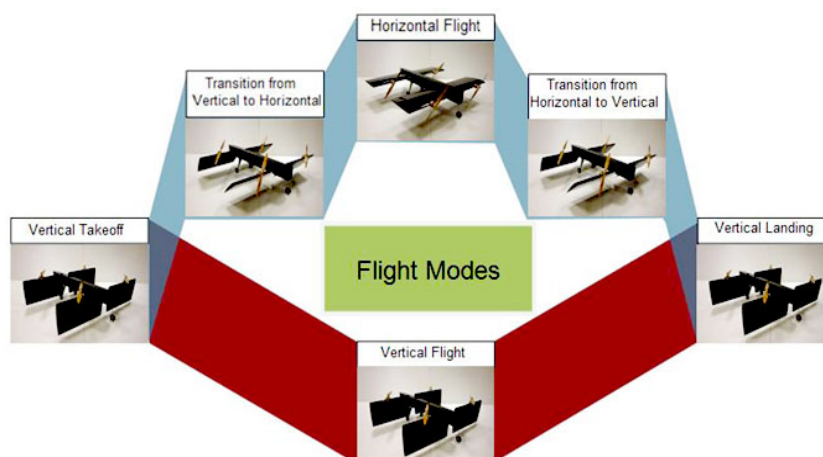


Figure 4.6: Different flight modes of SUAVI

The supervisory control system of SUAVI utilizes PID controllers both in high and low-level controls. The reason for the utilization of PID controllers is the simplicity and satisfactory performance on linear systems. SUAVI is

not a totally linear system, however its model can be linearized near some operating points and corresponding linear control algorithms can be utilized by switching the control parameters on the appropriate values.

A PID controller is mathematically formulated as (Fig. 4.7),

$$u(t) = K_p e(t) + K_i \int_0^t e(\tau) d\tau + K_d \frac{de(t)}{dt} \quad (4.49)$$

where K_p , K_i and K_d are the tuning parameters for the weights of proportional, integral and derivative control respectively and the error $e(t)$ is defined as

$$e(t) = X_{ref} - X(t) \quad (4.50)$$

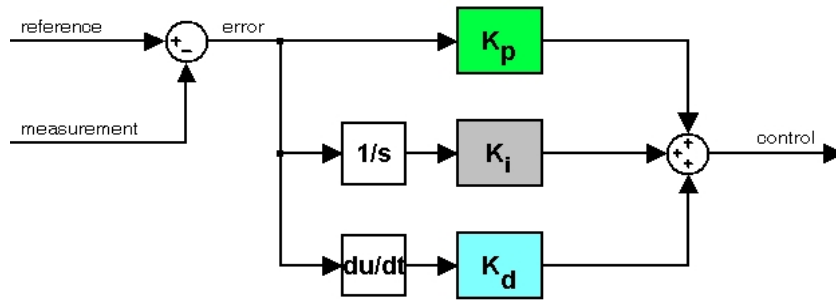


Figure 4.7: PID controller

This control formulation is discretized for its implementation in digital control system as

$$u_r[k] = K_{p,r} e[k] + K_{i,r} \sum_{i=0}^k e[i] T + K_{d,r} \frac{e_r[k] - e_r[k-1]}{T} \quad (4.51)$$

where $r = Z, \phi, \theta$ and ψ .

K_p tunes the direct effect of the error. It can make the system unstable if set to a very large value, whereas it may be ineffective if set to a very low

value. K_i is a weight for the integration of the error over time. It is mainly used for reducing the steady-state error of the system. It can however raise oscillations on the system if tuned to a value that is more than necessary due to the fact that it is highly dependent on the data from the past. K_d is used as a damping coefficient on the control system, that reduces the magnitude of the overshoots and increases the overall stability of the control.

4.4.1 The High-level Controller

The high-level control system is responsible for the generation of feasible trajectories and corresponding attitude references for the low-level controllers, for the switching of the low-level controllers into the system depending on the flight mode requirements, forming the communication link with the ground station and performing all controls including the security control.

It performs estimations of the state variables utilizing the measurements obtained from the onboard sensors, detects visual objects to track, obtains the way points for the navigation and generates control signals for the actuators to follow the attitude and trajectory references.

The high-level controller in the supervisory control system of SUAVI is implemented in a *Gumstix*[®] microcomputer. As the high-level controller, Gumstix utilizes data from the GPS and the camera that is connected to the camera port of OMAP3530 processor. The image processing based operations are performed utilizing the OpenCV library. The DSP core on the microcomputer allows the computations of image processing algorithms at higher speeds. Such a computation would be impossible without such a computationally powerful computer.

The communication with ground station is achieved via an XBee long

range RF communication module that has a carrier frequency of 900 MHz. The microcomputer is connected to the XBee and to the low-level control system via its UART ports (Fig. 4.8).

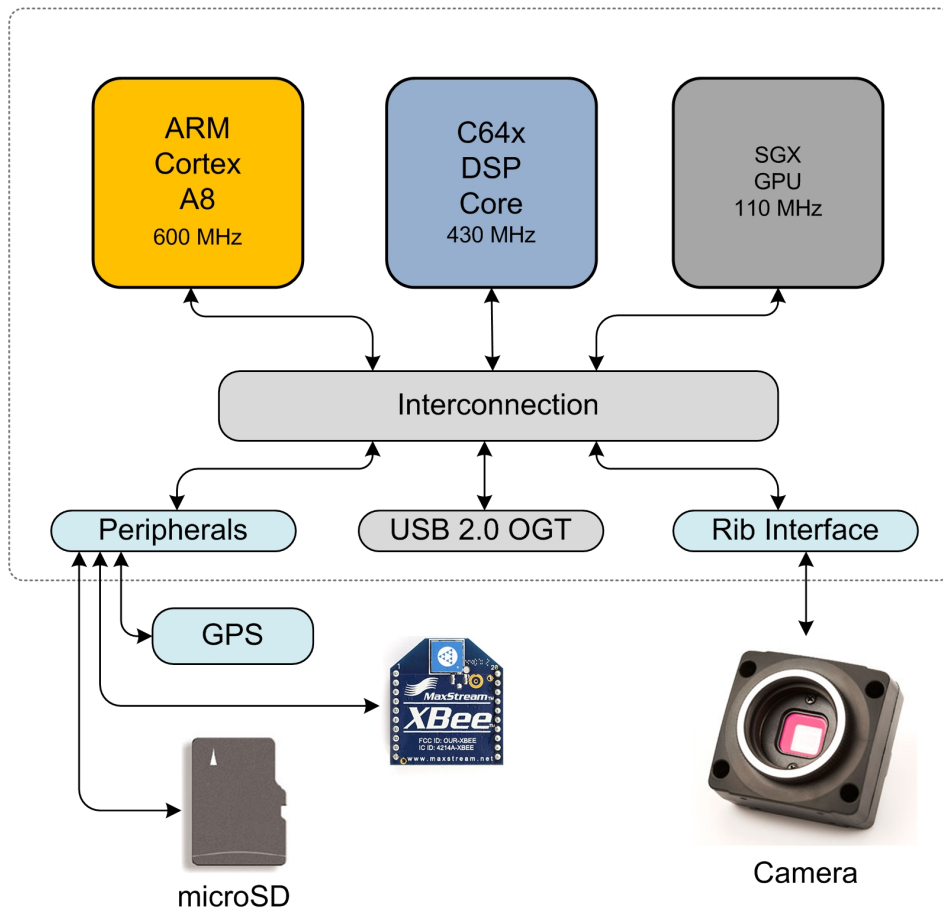


Figure 4.8: The processor block diagram

The GPS data is received directly from the GPS module and processed for the acquisition of the coordinate information from the bulky GPS data. The errors are calculated in earth frame for the generation of accelerations using PID controllers. Then, the attitude references for the low-level control system are computed (Fig. 4.9).

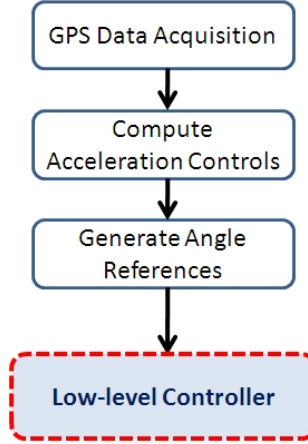


Figure 4.9: Flow diagram of the GPS based control

GPS Based Hovering

For the GPS based hovering, the high-level control system utilizes PID control algorithms. For \mathbf{x}_n ve \mathbf{y}_n being the unit vectors along the x and y axes of the world frame and $x(t)$ being the instantaneous position of the vehicle provided by GPS, e_x and e_y are the position errors along x and y axes. It follows that

$$e_x = (\mathbf{x}^d - \mathbf{x}(t)) \cdot \mathbf{x}_n \quad (4.52)$$

$$\dot{e}_x = -\mathbf{v}(t) \cdot \mathbf{x}_n \quad (4.53)$$

$$e_y = (\mathbf{x}^d - \mathbf{x}(t)) \cdot \mathbf{y}_n \quad (4.54)$$

$$\dot{e}_y = -\mathbf{v}(t) \cdot \mathbf{y}_n \quad (4.55)$$

To hover the vehicle at a given position, PID controllers are designed along both x and y axes (Fig. 4.10), namely

$$u_x = K_{x,p}e_x + K_{x,d}\dot{e}_x + K_{x,i} \int_0^t e_x dt \quad (4.56)$$

$$u_y = K_{y,p}e_y + K_{y,d}\dot{e}_y + K_{y,i} \int_0^t e_y dt \quad (4.57)$$

Note that these controllers are acceleration controllers along x and y axes. To handle the effect of the air vehicle's heading, ψ , which is the radian value of the compass heading wrt. north being 0 angle, these accelerations must be transformed using a 2D rotation matrix, $R(\psi)$, as follows:

$$a_{xy} = R(\psi)(u_x \cdot \mathbf{x}_n + u_y \cdot \mathbf{y}_n) \quad (4.58)$$

By using equation (4.58), reference attitude angles which allows the vehicle to hover at a given position are computed using the following formulas [159]:

$$\theta_{ref} = \arcsin\left(\frac{a_x}{\|a\|}\right) \quad (4.59)$$

$$\phi_{ref} = -\arcsin\left(\frac{a_y}{\|a\| \cos(\theta)}\right) \quad (4.60)$$

where a is $a = (a_x, a_y, a_z)$, a_x and a_y are the x and y components of the acceleration vector, a_{xy} , defined by Eqn. (4.58). The third component of the acceleration vector, a_z , is the acceleration of the vehicle along the z axis and is computed as $a_z = u_1/m$. $\|a\|$ is the Euclidean norm of a and is defined as

$$\|a\| = \sqrt{a_x^2 + a_y^2 + a_z^2} \quad (4.61)$$

Reference attitude angles computed by (4.59) and (4.60) can be low-pass filtered to be used for the attitude control performed in the low-level control system.

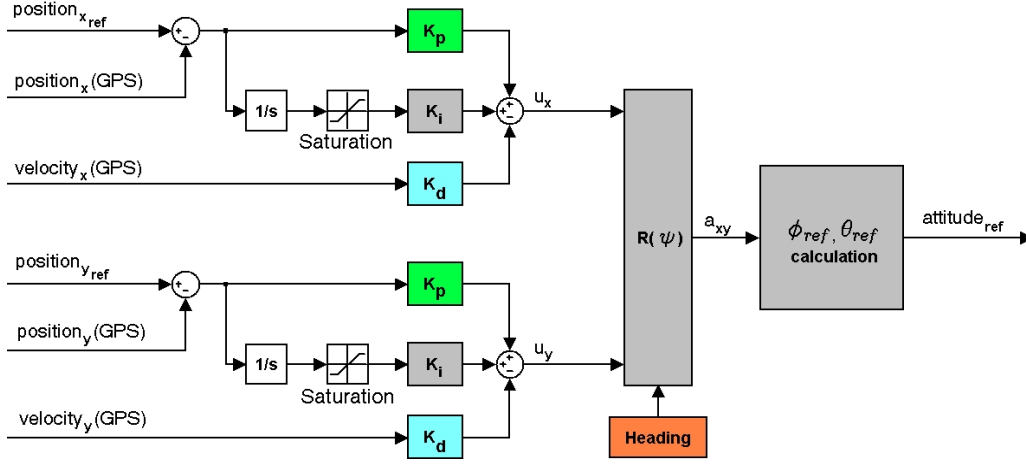


Figure 4.10: GPS based hovering control

GPS Based Waypoint Navigation

For the GPS based waypoint navigation, the high-level control system utilizes similar methods with the GPS based hovering control. A trajectory, $P \in N \times R^3$ is generated by N waypoints \mathbf{x}_i^d . For each trajectory part P_i , the flight vector of the aerial vehicle is set along the vector from \mathbf{x}_i^d to \mathbf{x}_{i+1}^d . For the along track and cross track position, a unit tangent vector \mathbf{t}_i along and a unit normal vector \mathbf{n}_i perpendicular to that vector are defined. For $x(t)$ being the current position of the vehicle measured from GPS, and v_i^d being the desired flight speeds of the vehicle between two consecutive waypoints i and $i + 1$, the cross track error e_{ct} , its derivative \dot{e}_{ct} , and the along track error rate \dot{e}_{at} are defined as

$$e_{ct} = (\mathbf{x}_i^d - \mathbf{x}(t)) \cdot \mathbf{n}_i \quad (4.62)$$

$$\dot{e}_{ct} = -\mathbf{v}(t) \cdot \mathbf{n}_i \quad (4.63)$$

$$\dot{e}_{at} = v_i^d - \mathbf{v}(t) \cdot \mathbf{t}_i \quad (4.64)$$

For controlling the speed in along track direction, a PI controller is designed for the control of speed in the along track direction, whereas a PID controller is designed for the control of cross track position (Fig. 4.11); i.e.

$$u_{at} = K_{at,p}\dot{e}_{at} + K_{at,i} \int_0^t \dot{e}_{at} dt \quad (4.65)$$

$$u_{ct} = K_{ct,p}e_{ct} + K_{ct,d}\dot{e}_{ct} + K_{ct,i} \int_0^t e_{ct} dt \quad (4.66)$$

These controllers are acceleration controllers along x and y axes. The desired acceleration vector is constructed from the controller outputs (4.65) and (4.66) as

$$a_{des} = R(\psi)(u_{ct} \cdot \mathbf{n} + u_{at} \cdot \mathbf{t}) \quad (4.67)$$

where $R(\psi)$ is a 2D rotation matrix depending on the heading (ψ) for transforming the accelerations in world frame to accelerations on the body frame.

Reference attitude angles which allow the vehicle to navigate on a trajectory are computed by using Eqn. (4.59) and Eqn. (4.60) given in hovering section.

4.4.2 The Low-level Controller

The low-level control system is responsible for the realization of low-level control methods as requested by the high-level controller via high-level inputs (u^H) and acquire low-level measurement data (y^L) for sending to the high-level controller. These attitude control and signal acquisition processes can be accomplished at very high frequencies when compared with the high-level processes. The low-level controller also behaves as a buffer between these

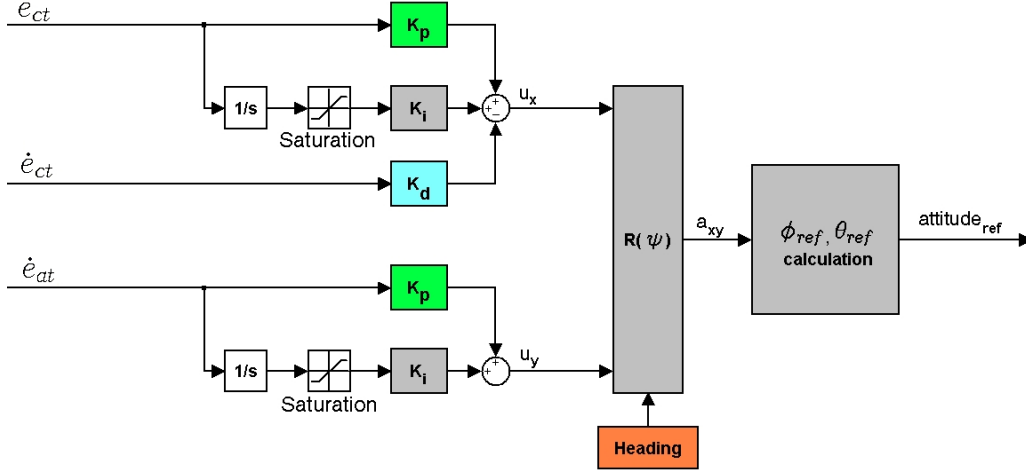


Figure 4.11: GPS based waypoint navigation

high-frequency and low-frequency processes.

The low-level control system is implemented in Atmel Atmega16 micro-controllers that operate as real-time systems. It utilizes PID controllers for attitude stabilization and gravity compensated PID controller for altitude stabilization. The PID controller in Eqn. (4.49) can be restated for altitude (Fig. 4.12) and attitude (Fig. 4.13) control of SUAVI as:

$$u_1 = K_{p,z}e_z + K_{d,z}\dot{e}_z + K_{i,z} \int e_z dt - \frac{mg}{c_\phi c_\theta} \quad (4.68)$$

$$u_2 = K_{p,\phi}e_\phi + K_{d,\phi}\dot{e}_\phi + K_{i,\phi} \int e_\phi dt \quad (4.69)$$

$$u_3 = K_{p,\theta}e_\theta + K_{d,\theta}\dot{e}_\theta + K_{i,\theta} \int e_\theta dt \quad (4.70)$$

$$u_4 = K_{p,\psi}e_\psi + K_{d,\psi}\dot{e}_\psi + K_{i,\psi} \int e_\psi dt \quad (4.71)$$

where u_1 is the control effort of the overall thrust for lift, u_2 is the effort for roll, u_3 is the effort for pitch, and u_4 is the effort for yaw.

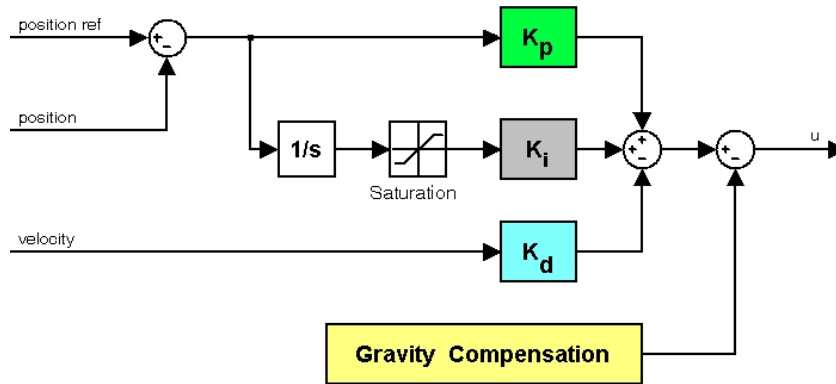


Figure 4.12: PID altitude control system

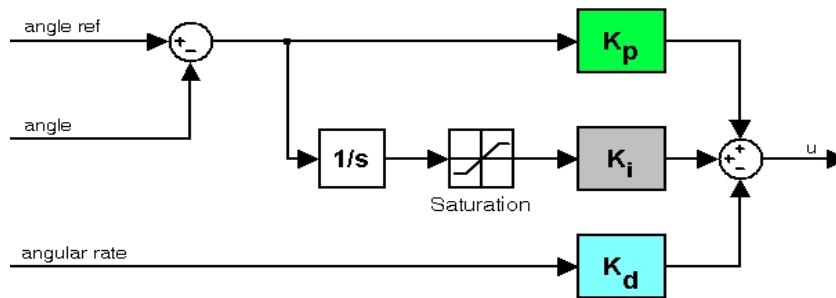


Figure 4.13: PID attitude control system

As stated before, the PID control equation for the altitude includes an additional gravity compensation term. This term cancels the continuous effect of the gravity on the air vehicle to improve the altitude control performance.

4.5 Overall Supervisory Control System

The overall supervisory control system is depicted as in Fig. 4.14. It is apparent that the sensors that are very crucial for stabilization of the system are communicating with the low-level control system directly to prevent un-

necessary interrupt handling tasks in the high-level controller and guarantee the real-time utilization of sensor data without time loss.

The data transfer between the low-level and high-level control systems is accomplished on a multi-directional RS232 communication line. The low-level control system transmits all the states, sensor data and control variables to the Gumstix microcomputer, which acts as the supervisor, periodically. The high-level controller generates the attitude references for the trajectory tracking and sends these references to the low-level control system.

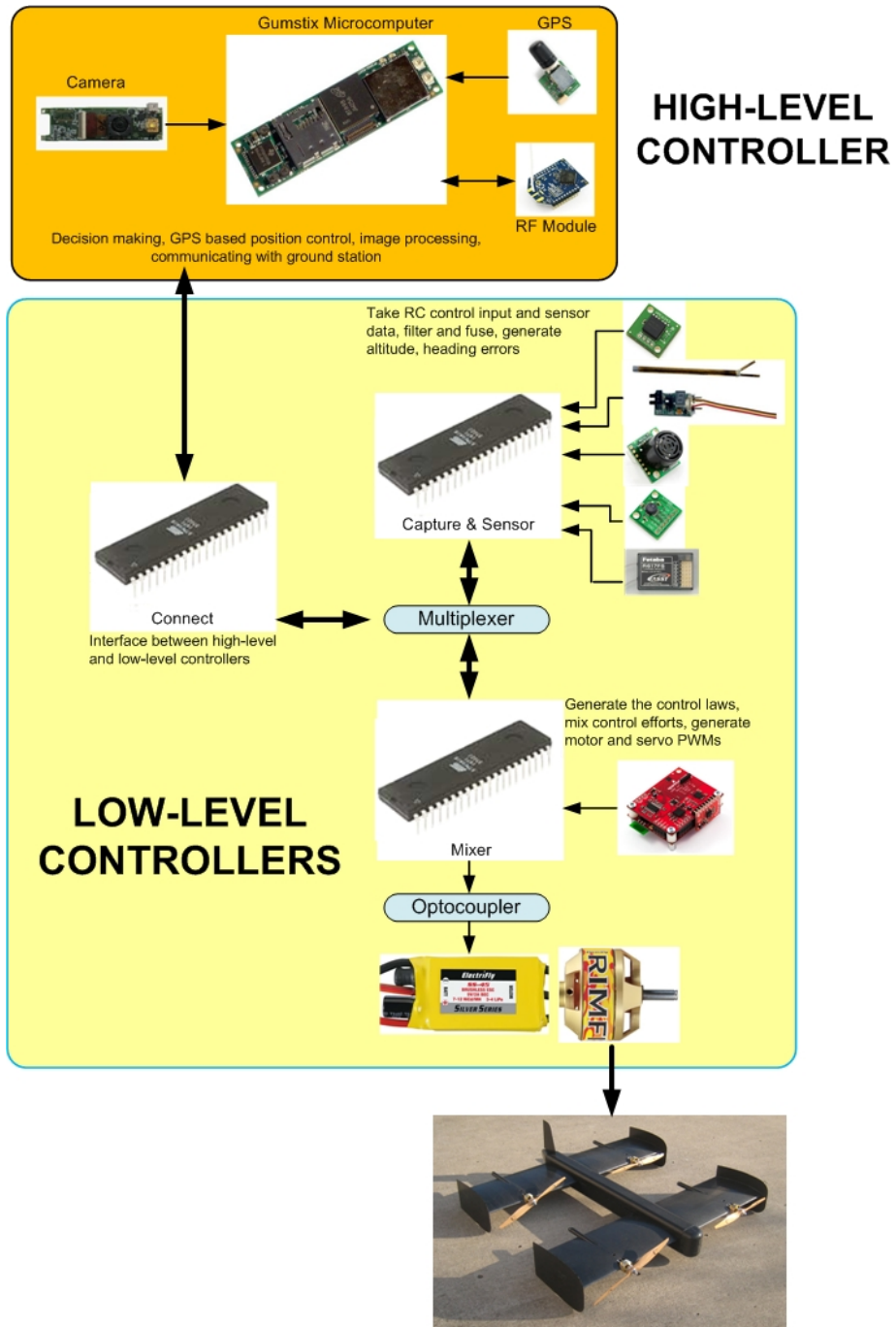


Figure 4.14: The schematic of the supervisory control system

Chapter 5

5 Flight Control System Components

The electronic system of SUAVI is the backbone of the flight; without an electronic control circuit a control architecture cannot be implemented and the UAV body is only an object to be controlled. This system contains sensors and actuators for situational awareness and acting on the mechanical system, filters to make the sensor data useful, microcontrollers to implement the low-level controllers and surely the integration of all these systems for the flight.

5.1 Sensors

To achieve satisfactory stabilization and trajectory tracking, reliable state estimates need to be acquired by the supervisory control system. For obtaining these reliable state estimates, sensor data is required to be gathered properly and several filters are needed to be applied.

5.1.1 Inertial Measurement Unit (IMU)

The stabilization of SUAVI during the flight is highly dependent on the accurate measurement of the roll, pitch, yaw angles and angular velocities

due to the requirements of the control. To provide these measurements, a sensor board named as IMU is utilized.

The IMU used in this project is mainly a sensor board containing 3-axis accelerometer, 3-axis gyro, 3-axis magnetometer and an ARM processor for a variety of processes (Fig. 5.1). It has some additional features such as RS232 and Bluetooth communications and onboard power regulation to reduce noise transmitted through the power line.

For accurate conversion of sensor readings to angular position and velocity data, Extended Kalman Filter is implemented in the ARM processor using C language and the resultant data is fed to the low-level control system via the RS232 communication line.

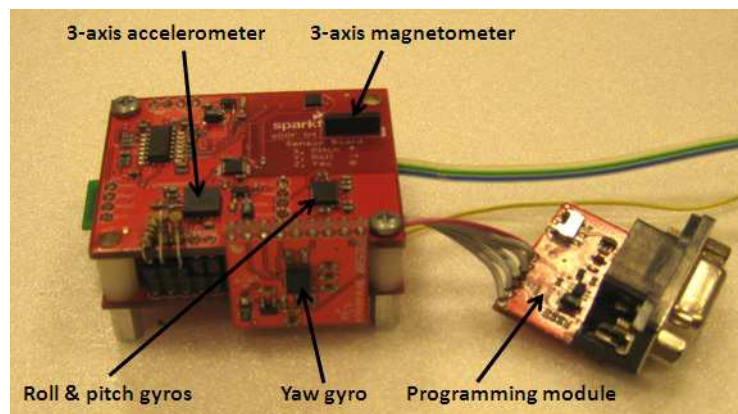


Figure 5.1: Inertial Measurement Unit (IMU) used in the system

5.1.2 Compass

The digital compass is nearly an inevitable sensor for all UAVs, due to the fact that it delivers very crucial heading data both for yaw stabilization and navigation. In the project, SparkFun Electronics compass module with Honeywell HMC6343 tilt compensated compass is utilized (Fig. 5.2). This

compass includes a three-axis accelerometer and a three-axis magnetometer in a single chip. It can output tilt-compensated heading measurement, magnetometer readings and accelerometer readings all through I^2C communication protocol. It delivers the tilt-compensated heading measurement using both the magnetometer readings for estimating 3D magnetic direction of the earth magnetic field and accelerometer readings to estimate its inclination wrt. the ground.

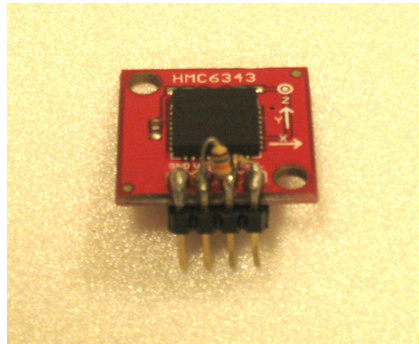


Figure 5.2: Digital compass used in the system

For the sea vessels, normally, two-axis compass is sufficiently useful, since they are parallel to the ground all the time except the cruises on very rough seas, where some periodic rolling and pitching exists. On the air vehicles however, there are the rolling and pitching actions most of the time, causing errors on the measurements.

The reason for the error is mainly the inclination of the magnetic field lines wrt. the ground, that is rarely 0° . 2D compasses do not measure the vertical component of the magnetic field. If the compass tilts, this third component adds or subtracts some magnetic reading (Fig. 5.3). This change in magnetic reading causes the compass to read the heading with errors that can be fairly large.

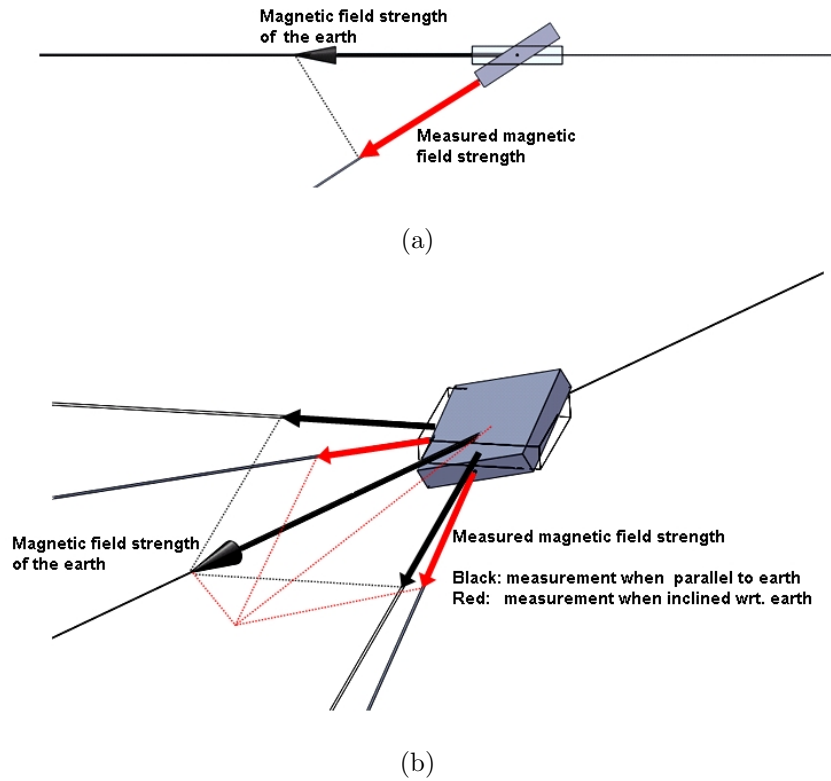


Figure 5.3: The reason for the errors on the heading measurement due to one axis (a) and two axes (b) inclinations

The tilt compensated compass solves this problem by finding the 3D magnetic field direction and projecting it on the virtual ground plane that it estimates through the inclination wrt. the ground. It uses the 3-axis accelerometer to find this inclination.

However, using only accelerometers to find the inclination is not a perfect solution for applications, where strong vibrations exist. In SUAVI, there are severe propulsion system driven vibrations, which add large errors on the tilt-compensated heading measurements. There is not any analog filtering pin on the compass chip for plugging some RC components for low-pass

filtering of the vibrant accelerometer readings in the compass. Hence, only the magnetometer readings in the chip are taken by the control system and they are fused with the tilt angle data from the IMU to provide low-noise heading information (Fig. 5.4).

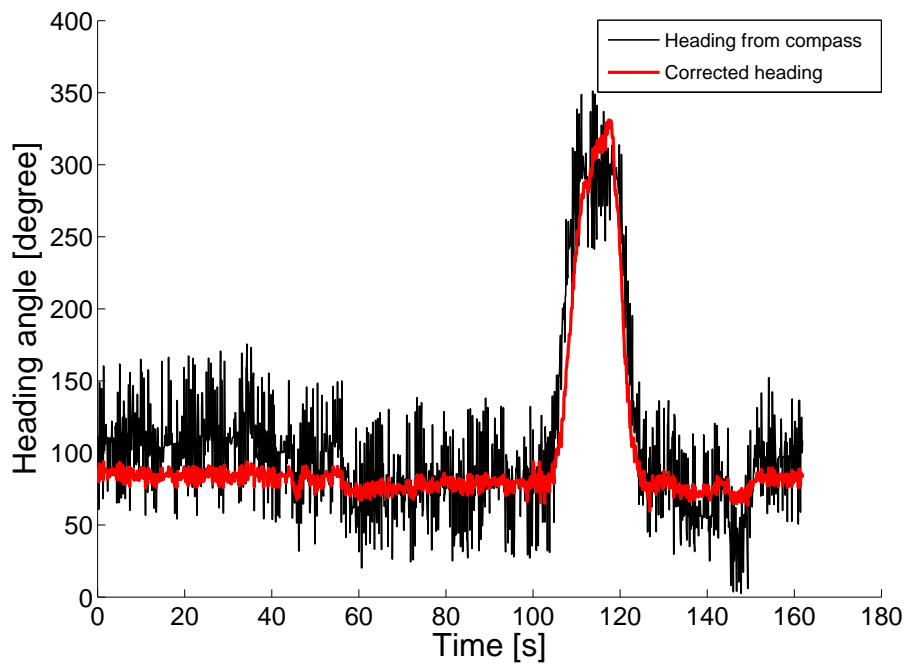


Figure 5.4: Compass reading with the noise due to the vibration and without that noise

An important issue to be careful on using the compass is that magnetic fields generated by high current flow in the cables and motors affects the reading of the compass and causes large errors. This is especially very effective on electric powered UAVs, on which the electric motors draw very high currents. To solve this problem, the compass should be positioned far from electric motors and cables, that carry high currents.

5.1.3 Sonar

Sonar, which is in fact an ultrasonic range finder is a fairly accurate distance measuring device. It operates relying on the returning time delay of the reflected high frequency sound waves. When this sensor is pointed to the ground, it can be used to measure the height from the ground.

In the electronic control system of SUAVI, Maxbotix EZ4 ultrasonic range finder is utilized (Fig. 5.5). According to its specs, this sonar has 2.54 cm (1") of resolution for up to 6.45 m distance. For the evaluation of performance, several types of sonar with different beam cone angles from widest to narrowest are tested and EZ4 with the narrowest beam cone angle is preferred due to its more reliable measurements in this application. This sensor has one main drawback of being able to operate only on hard surfaces due to its operating principle, so it cannot be used over grass, water and soil.



Figure 5.5: Ultrasonic distance sensor used in the system

The sonar directly outputs the analog signal that is proportional with the distance. This feature simplifies the interfacing of the sensor using the microcontroller, since it does not require any communication protocol, instead only the usage of an ADC channel on the microcontroller.

5.1.4 Altimeter

Altimeter is a barometric sensor that provides altitude measurement wrt. the sea level based on the ambient air pressure. It is widely used in aviation being the main altitude measurement device in all aircrafts. The key for its correct measurement is the correct setting of the pressure offset at the sea level on the place to be flown. In the project, VTI Technologies SCP1000 series barometric pressure sensor is utilized as an altimeter. According to the specs of this chip, it is sensitive to altitude differences of 10 cm (Fig. 5.6).



Figure 5.6: Ultrasonic sensor used in the system

The communication interface used in this IC is also I^2C as in the compass, however the data length is 19 bits to allow the resolution of 10 cm in the air, which has a very low density. Hence, the hardware I^2C module on the microcontroller cannot be used for data acquisition from this sensor due to the register size limitations in the hardware I^2C module. As a result, an I^2C communication code is implemented in the C compiler of the microcontroller to acquire the temperature and pressure data from the pressure sensor.

During the tests of this sensor in comparison with the sonar readings, it is observed that the measurements of this sensor can have errors of up to ± 50 cm and have some delay (Fig. 5.7). At less than 2 m of altitude above the ground, control of altitude based only on altimeter data may become

disastrous due to these errors and oscillations rise due to the sensor delay. For this reason, usage of sonar having much more accurate measurements is preferred at low altitude and additional D^2 control is implemented on the vertical axis to dampen the oscillations on altimeter usage.

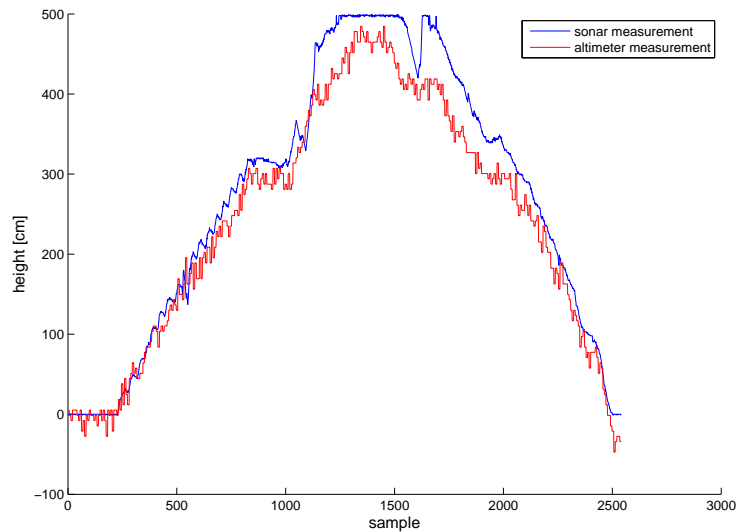


Figure 5.7: Sonar and altimeter measurements without motor operation (a) and during the flight (b)

5.1.5 GPS

GPS is yet another navigation tool, that only operates outdoors due to its dependency on the GPS satellites traveling in the earth orbit. It is a widely used navigation tool not only in aviation and sailing, but also in road tracking on the land. The usefulness of this technology makes it very popular, despite its relatively low data rate of 1-2 Hz and positional accuracy up to few m's. In the control system of SUAVI, ADH Technology D2523T GPS unit with a high-gain active antenna and 50 channel GPS receiver circuits is utilized

(Fig. 5.8).

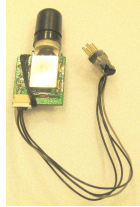


Figure 5.8: GPS module used in the system

This sensor can process GPS data at 2 Hz, but it also has the ability to deliver 4 Hz GPS data applying interpolation on the processed GPS data.

During the initial trials for the positioning accuracy, it is observed that this module has a positioning error of around 1-2 m when staying statically on the ground in an average cloudy day in a place where disturbances such as some trees, lamp posts and buildings exist with large clearances from each other (Fig. 5.9).

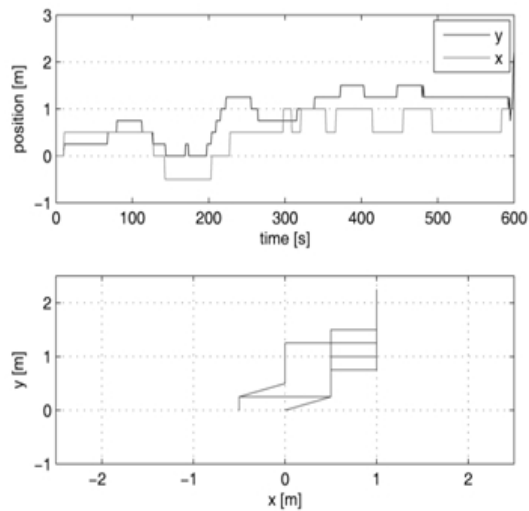


Figure 5.9: GPS measurement deviation in static conditions

To evaluate the positional accuracy of the GPS, in motion measurements are also obtained. In low-speed motion test, the GPS module is moved on an L-shaped track with walking speed and returned on the same track finishing the test at the initial point. In Fig. 5.10, it can be seen that the results of the GPS are generally satisfactory.

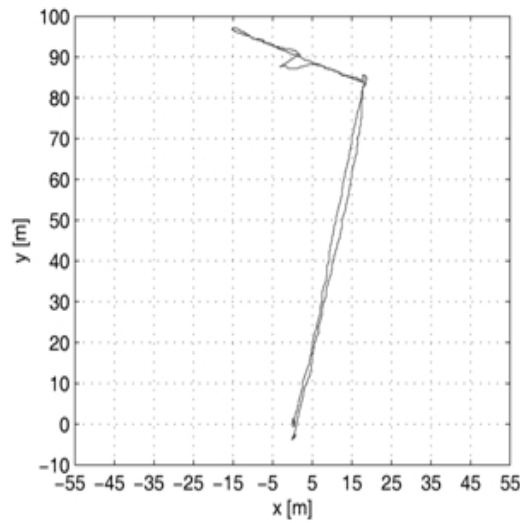


Figure 5.10: GPS measurement on an L shaped trajectory with low speed motion

The performance of the GPS module is also evaluated at higher speeds fixing it on a car and tracking the road around the Sabancı University campus. Through the mapping of the GPS readings on Google Earth software, it is observed that the performance of the GPS module is also satisfactory at higher speeds, which is very crucial at high speeds such as 60 km/h (Fig. 5.11). As a result of these tests, GPS is found to be useful for navigating, while its altitude measurement can sometimes be slow and unreliable in some cases.



Figure 5.11: Visualization of GPS measurement around Sabancı University at high speed

To obtain the coordinates using the GPS module, it is required to capture the sequential data sent on RS232 communication line and extract the coordinates from the line beginning with “GPGGA” in the data with NMEA protocol. An algorithm is developed to handle the raw data first to find “GPGGA” and then the commas, since the number of commas does not change even though data length can change depending on the required number of digits.

It is also worth to note that the GPS sends data only at some intervals depending on its data output frequency, and a bulky data is needed to be processed at those intervals. Additionally, the default settings of the GPS module dictates the GPS frequency of 1 Hz. To improve the quality of GPS tracking, codes for 2 Hz GPS reading setting are sent to the GPS at every startup or a backup battery for feeding the GPS when system is not working

can be utilized.

5.1.6 Airspeed Sensor with Pitot Tube

The airspeed sensor with pitot tube is a very crucial sensor, especially for the transition and horizontal flight modes, because the wing angle of attacks and motor speed controls have to adapt to the airspeed for stable flight. In the control system of SUAVI, Eagle Tree Airspeed MicroSensor V3 is utilized (Fig. 5.12).

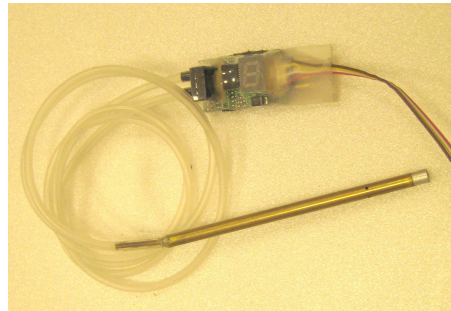


Figure 5.12: Airspeed sensor with Pitot Tube used in the system

This sensor operates by benefiting from the Bernoulli equations. These equations state, that the pressure difference between the dynamic pressure at front and the static pressure at side holes on the Pitot tube is proportional to the square of the frontal velocity. This airspeed sensor has a differential pressure sensor with its two pressure inputs connected to the two pressure lines of the Pitot tube. Using the pressure difference measurement, this sensor delivers an output of the square root of the measurement with some predefined offset value. Up to the minimum flight speed it can sense, which is around 15 km/h for this sensor, it delivers this offset value and beyond that speed it adds a term proportional to the speed to the offset value. To

calibrate this sensor, an experiment is conducted, in which this airspeed sensor and a precise anemometer are placed near to each other in the wind tunnel and the measurements of these two sensors are compared (Fig. 5.13).

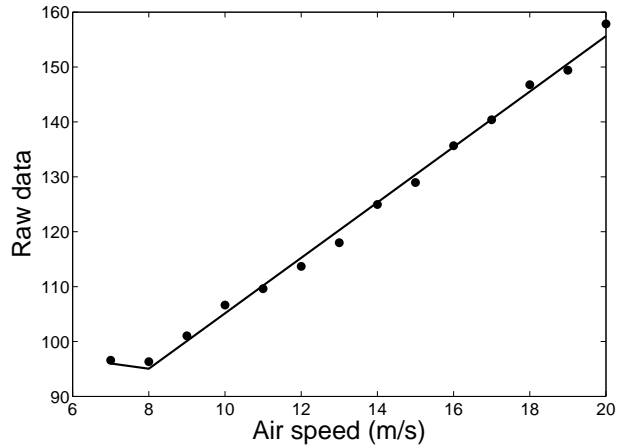


Figure 5.13: Calibration of the airspeed sensor in comparison with a sensitive airspeed measurement system

According to the results obtained from this comparison, the conversion formula from the raw measurement of the sensor to the airspeed value is determined to be

$$S = \frac{D - 54.6461}{5.0491}$$

where D is the airspeed sensor reading and S is the corresponding air speed.

5.2 Filters

The stabilization of SUAVI during the flight is highly dependent on the accurate measurement of the roll, pitch, yaw angles and angular velocities due to the requirements of the control. Since the UAV flies, its angular

position and velocity data cannot be obtained directly connecting encoders. Instead, they need to be estimated using inertial sensors on the aerial vehicle, however there are important obstacles to be hurdled. The first obstacle is the effect of motor vibrations on the accelerometer measurements, which ruins the accelerometer measurements and causes the angle data to be useless. This problem is solved using an analog low-pass filter.

The second obstacle is the effective noise on the sonar readings. Due to this noise with spikes, the sonar readings cannot be utilized directly. This problem is handled utilizing a digitally implemented exponentially weighted moving average filter.

A third very important obstacle is the imperfectness of these sensors. The zero measurement mean values of both the accelerometers and gyros change and also there are couplings between the measurements of different motions. As an instance, the x-axis measurement of an accelerometer changes both by a linear acceleration in x-direction and a change in pitch angle. Extended Kalman Filter is utilized for the sensor data fusion to obtain reliable attitude estimation.

5.2.1 Analog Low-pass Filter

To handle the problem of vibration effect on the accelerometer readings, a very logical solution is to apply analog low-pass filters on the outputs of the accelerometers. Usage of analog low-pass filters is reasonable due to two separate reasons. First, low-pass filtering directly attacks the addition of the vibration components on the measurements. The main reason of the vibrations in the propulsion system is the effect of high speed rotation of unbalanced loads, that is also magnified proportionally with the square of the

rotation speed. The accelerations caused by these large magnitude vibrations are added on the real measurements (Fig. 5.14). The rotors rotating with beyond 4000 RPM rotational speeds cause very high frequency accelerations. Hence, this vibration effect is to be filtered out through low-pass filtering.

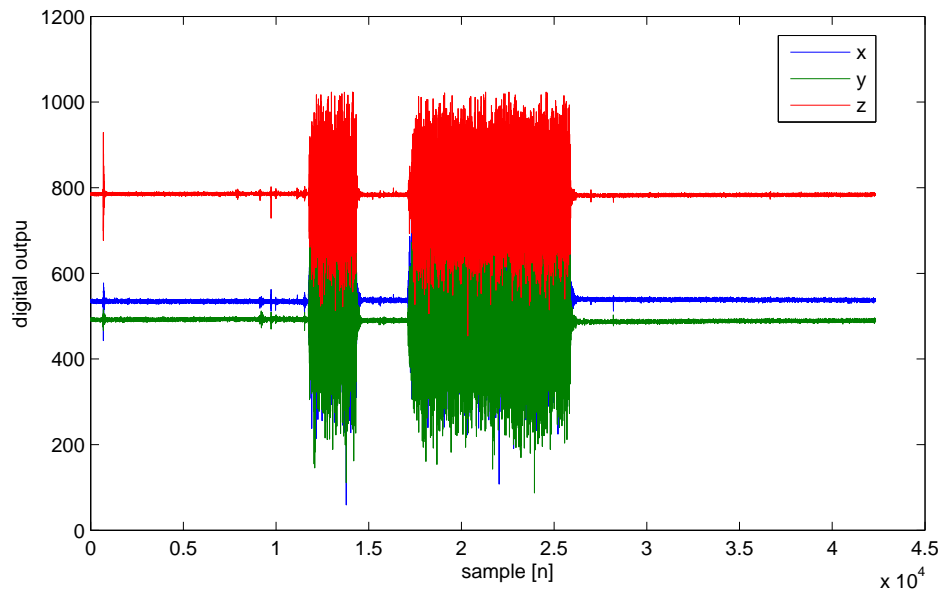


Figure 5.14: Raw accelerometer readings around x, y, z axes during hover

Second, analog low-pass filtering is superior in the performance to the digital low-pass filtering because the ADC samples the filtered signal, so the problem of aliasing is prevented.

The RC low-pass filter is implemented on the IMU between the accelerometer outputs and the ADC inputs of the ARM processor. The cut-off frequency to obtain proper acceleration readings under the existence of the vibrations is determined to be 0.6 Hz. The inclusion of this low-pass filter brings reasonable readings for the utilization in the sensor fusion (Fig. 5.15).

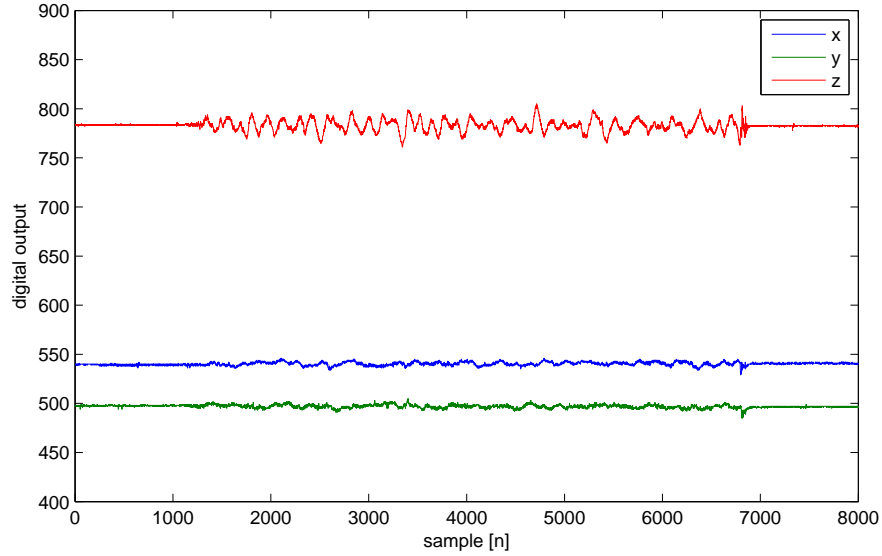


Figure 5.15: Low-pass filtered accelerometer readings around x, y, z axes during hover

5.2.2 Digital Exponentially Weighted Moving Average Filter

The raw measurement of the sonar is very noisy with dangerous spikes under the effect of propulsion system driven vibration, air flow directed to the ground and even the inclinations at altitudes above 3.5 m making it impossible to use directly in the altitude control (Fig. 5.16).

A low-pass filter is also not very effective to solve the problem. Hence, an Exponentially Weighted Moving Average (EWMA) filter is implemented, in which the filter output is a convex combination of the filter output in the previous step and the current raw sensor measurement as in equation

$$F_t = \alpha S_t + (1 - \alpha)F_{t-1} \quad (5.1)$$

where F_t is the current filtered measurement, F_{t-1} is the previous filtered

measurement, α is the weighting scale and S_t is the current raw measurement.

In this equation $0 \leq \alpha \leq 1$ and the weighting of the previous filtered measurement $(1 - \alpha)$ is increased when the difference between two consecutive sonar measurements is very large. When this difference is not large, the weighting scale α is increased for the incorporation of the current raw measurement. The formula for the adaptive calculation of α is:

$$\alpha = \frac{|\Delta S|}{|\Delta S|^{\delta_1} + (|\Delta S|^{\delta_2} + \varepsilon)^{-1}} \quad (5.2)$$

where $\Delta S = S_t - S_{t-1}$, $\delta_1 = 1.4$, $\delta_2 = 0.2$ and $\varepsilon = 0.1$. Fig. 5.16 reveals unfiltered and filtered altitude data to show the performance of the filter.

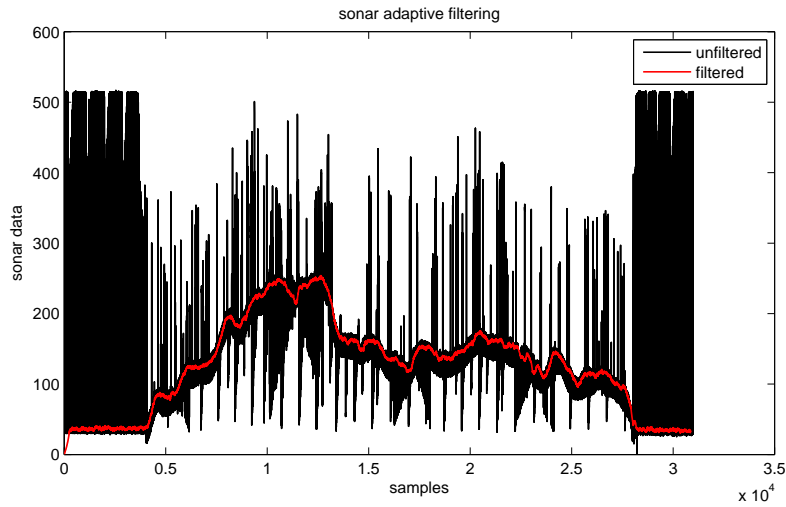


Figure 5.16: The raw and the filtered altitude measurements from sonar

5.3 Sensor Fusion via Kalman Filter

For accurate conversion of sensor readings to angular position and velocity data, Extended Kalman Filter (EKF) is implemented in the IMU. Gyros,

that are utilized in the IMU, have fast response, however it is not possible to estimate angular position through integrating the gyro readings due to the gyro drift problem (Fig. 5.17). During the operation, even without any vibration, the gyro reading zero mean changes. Hence, the integral of the gyro reading becomes irrelevant with the actual value as time passes.

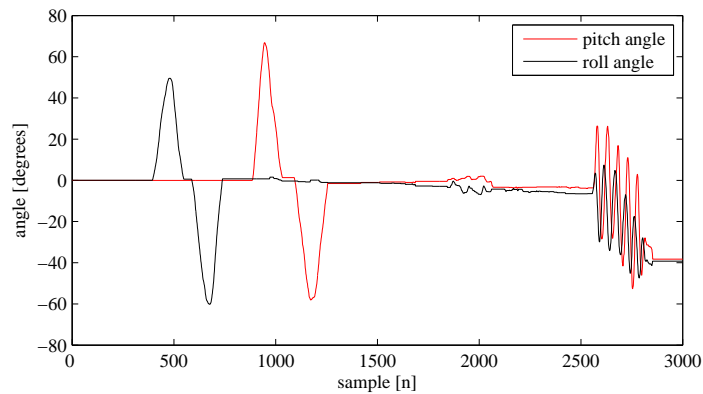


Figure 5.17: Drift in the integrated gyro data

Even though the accelerometers are much more reliable than the gyros in terms of mean value repeatability, their readings are delayed due to the low-pass filters applied into the system. This is also true for the heading information obtained from the compass. Additionally, the compass reading can be affected instantly from the magnetic field changes due to the ferromagnetic materials and electrical currents in the area.

EKF is utilized as a reliable attitude estimation tool that fuses the gyro, accelerometer and compass measurements [160]. By fusing these sensor types, it combines the fast response characteristic of the gyro measurements with the low drift feature of the accelerometers and the compass.

In EKF, the state transition and observation models can be nonlinear functions of states and inputs; there is no obligation for linear functions.

The system model for the design of the filter is

$$x_k = f(x_{k-1}, u_{k-1}) + \eta_{k-1} \quad (5.3)$$

$$z_k = h(x_k) + \nu_k \quad (5.4)$$

where η_k and ν_k are process and measurement noises.

In light of Eqn. (4.5), it follows that

$$\dot{\alpha}_w = \Omega_w = E^{-1}(\phi, \theta) \cdot \Omega_b \quad (5.5)$$

or,

$$\begin{bmatrix} \dot{\phi} \\ \dot{\theta} \\ \dot{\psi} \end{bmatrix} = \begin{bmatrix} 1 & s_\phi t_\theta & c_\phi t_\theta \\ 0 & c_\phi & -s_\phi \\ 0 & s_\phi/c_\theta & c_\phi/c_\theta \end{bmatrix} \begin{bmatrix} p \\ q \\ r \end{bmatrix} \quad (5.6)$$

Through the discretization using approximate derivative, Eqn. (5.5) becomes

$$\alpha_{w_k} = \alpha_{w_{k-1}} + TE^{-1}(\alpha_{w_{k-1}})\Omega_{b_{k-1}} \quad (5.7)$$

State evolution is conducted as

$$x_k = \begin{bmatrix} \alpha_w \\ b_g \end{bmatrix}_k = \begin{bmatrix} \alpha_{w_{k-1}} + TE^{-1}(\alpha_{w_{k-1}})\Omega_{b_{k-1}} \\ b_{g_{k-1}} + v_{g_{k-1}} \end{bmatrix} \quad (5.8)$$

where $b_g \in \mathbb{R}^3$ refers to the bias in gyros and T is the sampling time. EKF corrects bias term periodically by comparing the estimation of angle with the measurements from the accelerometers and the compass. The filter has prediction and correction steps. The prediction part is

$$\hat{x}_{k|k-1} = f(\hat{x}_{k-1|k-1}, u_{k-1}) \quad (5.9)$$

The four main equations of the Kalman Filter are:

$$P_{k|k-1} = A_{k-1}P_{k-1|k-1}A_{k-1}^T + Q_{k-1} \quad (5.10)$$

$$K_k = P_{k|k-1}H_k^T(H_kP_{k|k-1}H_k^T + R_k)^{-1} \quad (5.11)$$

$$\hat{x}_{k|k} = \hat{x}_{k|k-1} + K_k(z_k - h(\hat{x}_{k|k-1})) \quad (5.12)$$

$$P_{k|k} = (I - K_kH_k)P_{k|k-1} \quad (5.13)$$

where Q and R denote process and measurement covariance matrices, and A and H matrices are defined as

$$A_{k-1} = \frac{\partial f}{\partial x} \Big|_{\hat{x}_{k-1|k-1}, u_{k-1}} \quad (5.14)$$

$$H_k = \frac{\partial h}{\partial x} \Big|_{\hat{x}_{k|k-1}} \quad (5.15)$$

$P_{k|k-1}$ in Eqn. (5.10) is a priori error covariance matrix. It is used to compute Kalman gain (K_k) in Eqn. (5.11). The optimal state vector $\hat{x}_{k|k}$ is the sum of predicted state vector $\hat{x}_{k|k-1}$ and the correction term $K_k(z_k - h(\hat{x}_{k|k-1}))$. The correction term is computed using the measurements from the accelerometers and the compass. $P_{k|k}$ in Eqn. (5.13) is the posteriori error covariance matrix. It is utilized to update $P_{k|k-1}$ in Eqn. (5.10). Note that EKF requires initial conditions of \hat{x}_0 and $P_{0|0}$ for the first cycle.

Q and R matrices in EKF can be tuned experimentally to improve the

performance of the filter.

$$Q = \begin{bmatrix} 0.0001 & 0 \\ 0 & 0.000001 \end{bmatrix}, \quad R = \begin{bmatrix} 0.2 & 0 \\ 0 & 0.2 \end{bmatrix} \quad (5.16)$$

In the results of the EKF implementation it is observed, that the drift in the integral of gyro reading is eliminated both in the measurements without any vibration (Fig. 5.18) and with motor vibration (Fig. 5.19). It is also remarkable, that the estimations are not affected by the motor vibrations.

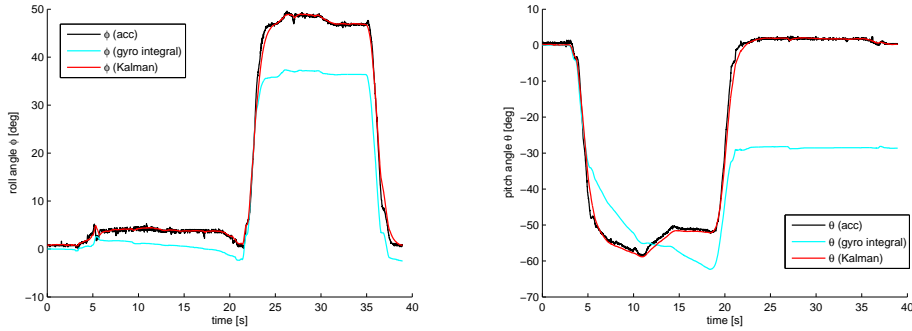


Figure 5.18: Kalman filter results in roll (a) and pitch (b) with hand motion

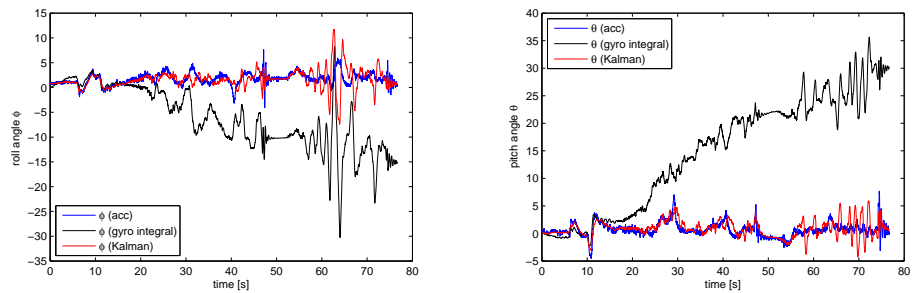


Figure 5.19: Kalman filter results in roll (a) and pitch (b) during flight

5.4 Microcontrollers

For the coded tasks in the low-level control system of SUAVI, Atmel Atmega16 microcontroller is preferred for its computational and peripheral features, much easier and faster supply, and broad development support on the Internet (Fig. 5.20).

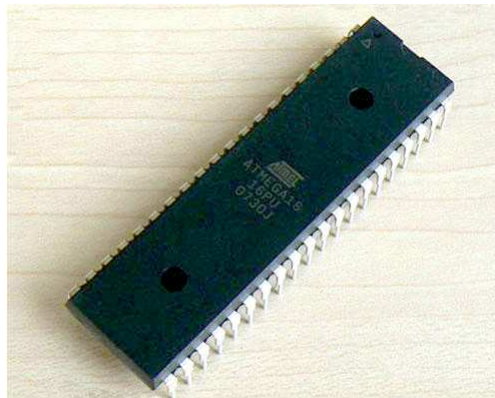


Figure 5.20: Atmel Atmega16 microcontroller with DIP package

A microcontroller is an integrated circuit that contains a microprocessor, a program memory, ADCs, modules for various communication protocols, PWM modules and peripheral I/O pins for a variety of possible tasks to be performed.

Atmel Atmega16 microcontroller has 16 MHz clock frequency with single clock operations, is able to handle 8 channel 10 bit analog to digital conversions, analog signal level comparisons, serial, I^2C , SPI communications, 2 channel PWM generations, and timer/counter operations.

It is programmed in Assembly or C languages, or as a combination of two, where C programming brings great ease of coding especially in big mathematical operations and Assembly language delivers precise timing.

5.5 Overall Electronic Control System

The electronic control system consists of a Gumstix microcomputer for high-level control side and four Atmega16 microcontrollers for the low-level control side. The programming and integration of the high-level computer into the system and the low-level control circuit design, production and coding are all performed as a part of this study. The entire electronic control system including the high-level computer, low-level control system and all the sensors and actuators is shown in Fig. 5.21.

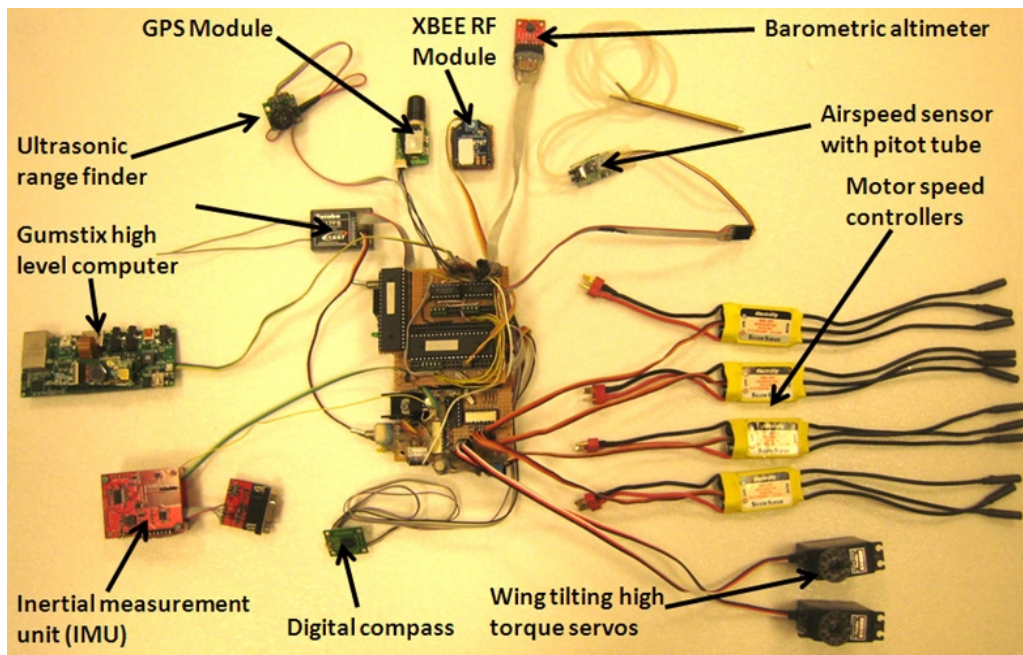


Figure 5.21: Overall electronic control system

The Gumstix Overo Fire that performs as the high-level computer of the control system is a very compact (17 mm x 58 mm x 4.2 mm), very lightweight (6 gr) but computationally powerful microcomputer (Fig. 5.22). It has an 600 MHz Texas Instruments OMAP (Open Multimedia Application Platform)

3503 microprocessor with floating point capabilities and a 256 MB DDR RAM memory. To access its peripheral signals, it is mounted on a Gumstix Overo Summit expansion board, which is also a compact (80 mm x 39 mm) and lightweight (16 g) circuit, but has power regulation, DVI-D screen port, three USB ports, sound I/O ports and a forty pin I/O port with serial I/O, I^2C , SPI, PWM, ADC and general purpose I/O signals. Gumstix can operate embedded Linux distributions and OpenCV, and perform complex tasks such as GPS based position control.

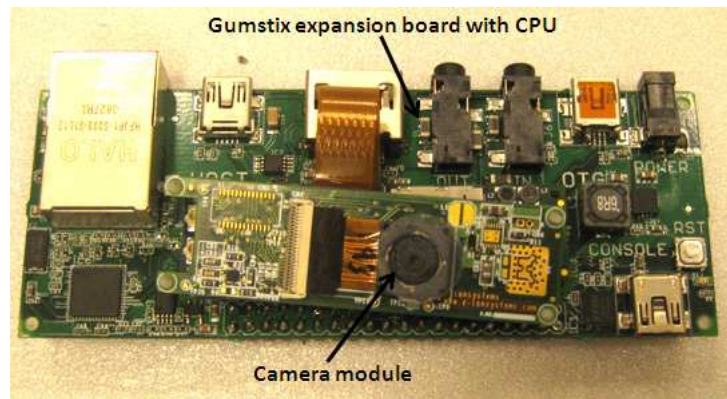


Figure 5.22: Gumstix Overo microcomputer with its onboard camera

The Gumstix microcomputer receives all flight data to have full information of the air vehicle related with control to enable the implementation of various control algorithms both for recent tests and for the future developments on the system. This microcomputer transmits the attitude references to the low-level control system in a sporadic manner. The timing of the data transmission is highly dependent on the tasks it performs as a high-level controller. Hence, the low-level control system receives this data utilizing an interrupt handler not to miss any data transmitted by the high-level controller.

The tasks of the low-level control are to gather sensor data, perform necessary filterings for reliable state estimations, gather the human operator inputs on the system, handle the low-level control calculations for the stabilization of SUAVI on the reference orientations demanded by the high-level controller and generate the control signals for the actuators.

The low-level control circuit, that is designed, produced and programmed in this study, contains a total of three Atmel Atmega16 microcontrollers (Fig. 5.23). The reason for the existence of that many microcontrollers is that there are hard real-time, soft real-time and sporadic tasks altogether to be accomplished without missing any sensor data, any control loop and any control pulse generation. These microcontrollers have separate tasks and are named mainly depending on their tasks that are Mixer, Capture & Sensor and Connect.

The Mixer microcontroller obtains the angle and angular velocity measurements from the IMU and references from the capture, computes the control commands, mixes the main four control commands, that are the roll, pitch, yaw and throttle commands, and finally generates the corresponding motor throttle references for propulsion and the servo control references for the wing tilting servos and the flaperon servos on the wings. All this operation is performed at 100 Hz and is hard-real time at all.

This loop is triggered by the end of the angle and angular velocity transmission of the IMU to the Mixer. It runs on interrupt of the RS232 channel not to miss any data transmitted by the IMU. Since there is no tolerance for latency on the Mixer's operation, Mixer-Capture & Sensor communication is done only by the Mixer's request. Also the Connect does not disturb the SPI communication line that is multiplexed between Connect-Capture & Sensor

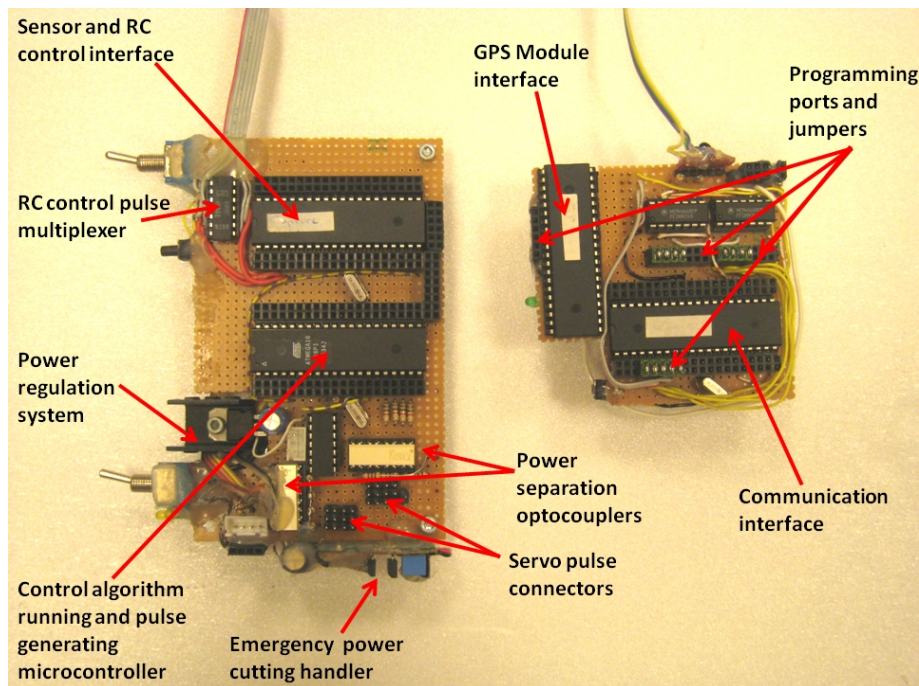


Figure 5.23: Low-level control circuit

and Mixer-Capture & Sensor when Mixer is communicating with Capture & Sensor.

The Capture & Sensor microcontroller obtains 3-axis magnetometer data from the compass via I^2C , airspeed data from the airspeed sensor via software coded I^2C , barometric pressure and temperature data from the altimeter again via software coded I^2C , sonar altitude data from the sonar utilizing its ADC and the control references from the RC control capturing the servo pulses. It also supports the data exchange between Connect and Mixer, responding both of them through the SPI communication line and performs the filtering and conversion tasks of the sensor data. It also generates the altitude control command through fusing the barometric altitude and ultrasonic altitude, and finding the altitude error.

The Connect microcontroller provides the bi-directional communication between the low-level control circuit and the Gumstix high-level control computer. It collects sensor data from the Capture & Sensor microcontroller, sends the obtained data to the Gumstix and gets the commands of the Gumstix computer through the RS232 interrupt, since the time when Gumstix transmits command message is not very strict. When a command message from the Gumstix is received, Connect transfers it to the Capture & Sensor for the low-level controller to fulfill the reference commands sent by the high-level computer.

The I^2C communication is used in the interfacing of the compass, the airspeed sensor and the altimeter that contains both barometer and thermometer. It is noticeable that, the digital output single chip small sensors in the system communicate through I^2C communication and it would not be a surprise if in the near future also the rest of the sensors use I^2C communication. The advantage of this protocol is that a device such as a microcomputer or microcontroller can communicate with up to 128 sensors or other devices only using two wires for communication, one line being for clock and the other being for data transmission.

This communication is clock synchronized with the master device controlling the clock. Thus, the master device has the ability to determine when to start, stop or suspend the communication. Both communication lines are connected to the supply voltage via pull-up resistors, so when a device needs to transmit its 0 signal on the line, it pulls the line down by connecting the line to the ground with its inner transistors (Fig. 5.24). I^2C is similar to CANBUS in this aspect.

The servo pulses that are both captured and generated in the control

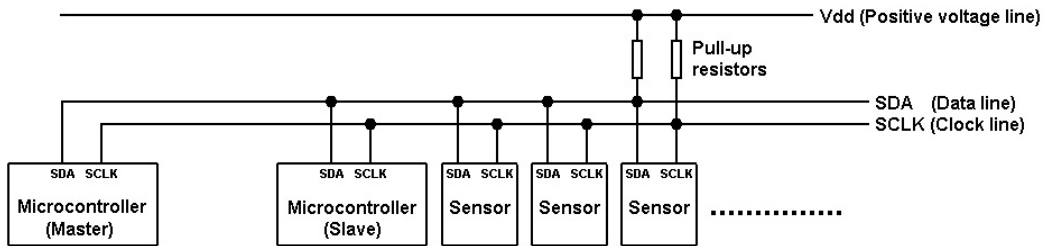


Figure 5.24: I2C communication circuit structure

circuit are rectangle waves having 10-20 ms periods and 1-2 ms positive pulse widths (Fig. 5.25). The excess pulse width beyond 1 ms determines the position of servos and motor speed controllers in proportional radio control systems. These pulses can be generated using hardware PWM modules of the microcontrollers or microcomputers, however 8 bit PWM is too coarse to be used since the resolution is only 12-13. 16 bit PWM modules generate very fine PWM signals that are far finer than required.

There are two 8 bit hardware PWM modules on Atmega16 microcontroller. For this reason, a software PWM code is written, in which the counter variables are assigned with the numbers to be counted back, servo pulse signals are risen and counters are lowered in every counting period until the 2 ms time counter becomes 0.

When a counter becomes 0 before the 2 ms total time, the signal on its channel falls. To prevent the fallen channels from decreasing the total time of 2 ms and the pulse widths of the still risen channels, one clock cycle long "nop" commands are added to the conditional statements of the fallen channels. By this way, 8 servo pulse channels with $3.6 \mu\text{s}$ resolution are obtained. This result would even not be achieved by eight 12 bit PWM channels.

The capturing method of the servo pulses from the RC receiver uses one

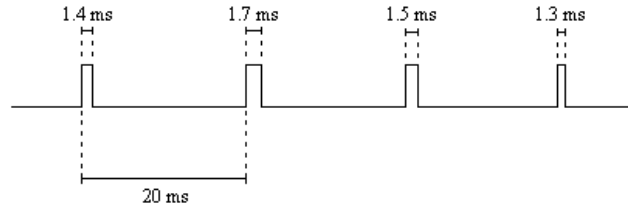


Figure 5.25: Servo pulse

capture pin on the Atmega16 due to the availability of only one. This method exploits the fact that RC receivers produce the servo pulses sequentially, so when one pulse falls, the next pulse rises (Fig. 5.26).

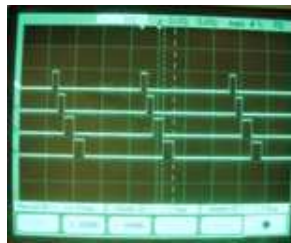


Figure 5.26: Servo control pulses generated by the RC receiver

In this method (Fig. 5.27), a multiplexer with four inputs connected to the RC receiver's channels sequentially transfers the signal of the selected channel to the capture input pin of the microcontroller. At the very beginning of the operation, the first channel is selected and the interrupt source of the capture pin is defined as rising edge. The capture module generates an interrupt, when the signal of the first channel is risen.

In the interrupt code, first the capture timer count is cleared and then if the valid channel number is 1, the interrupt source of the capture pin is defined as a falling edge. This is done since up to the end of the capturing of all channels, only the falling edge of the valid channels will be detectable. After up to 2 ms time, the next interrupt is taken meaning that the signal

Chapter 6

6 Simulations and Experiments

For the evaluation of the developed control algorithms, first, simulations are performed in *Matlab*[®] environment. When a control simulation is evaluated as successful, the codes are implemented into the electronic control system of a quadrotor helicopter test platform and then into the SUAVI for further testing and addition on the system.

6.1 Simulation Results

For the development of control algorithms and for the very first performance tests, a simulation environment of SUAVI is built in Matlab Simulink with VR Toolbox utilizing the developed dynamical model of the aerial vehicle. Before trying the GPS codes in the flight tests, numerous GPS based control simulations are performed in this environment both for GPS based hovering and waypoint navigation. The results of these tests are found to be promising.

6.1.1 GPS Based Hover

For the evaluation of the hovering performance, the PID type GPS based hovering control algorithm, which is explained in Chapter 4, is employed on the dynamic model of SUAVI. The simulations in Simulink environment are performed with the external disturbances applied on the system utilizing the

Dryden wind model. The performance of the hovering control is found to be satisfactory with the implementation of the parameters given in Table 6.1 and disturbance observer.

Table 6.1: Implementation Parameters for Hovering Control

Control	K_p	K_d	K_i
Roll	30	10	0.1
Pitch	30	15	0.1
Yaw	10	4	0.1
Altitude	40	15	0.1
X position	25	40	8
Y position	25	40	8

Figures 6.1 and 6.2 depict the hovering and the attitude tracking performances with disturbance rejection. The disturbance observer, that is proposed in Chapter 4, is used to estimate the effect of the wind on the aerial vehicle and reject it. In the hovering simulations, SUAVI takes off from just below the reference position for hovering and is controlled for staying on the reference position in the existence of winds and gusts.

It should be noted that the position reference in x-y plane is tracked with some error that is bounded by 20 cm and the altitude reference is tracked with error that is less than 10 cm. The tracking errors of attitude angles do not exceed $\pm 2^\circ$. Moreover, it is apparent in Fig. 6.2 that the aerial vehicle follows its constant heading reference, $\psi_{ref} = 0^\circ$, with less than 1° error. As Figure 6.3 depicts, the required motor thrusts do not exceed 16 N, that is the limit of the motor-propeller couples utilized in SUAVI.

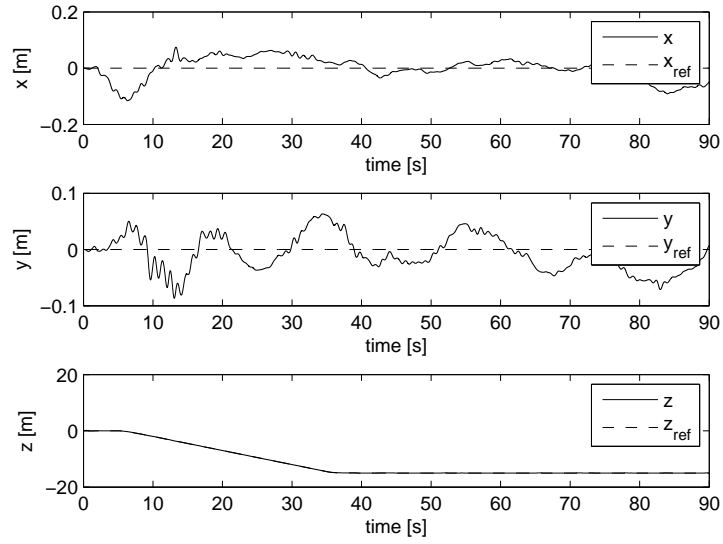


Figure 6.1: Hovering performance with disturbance observer

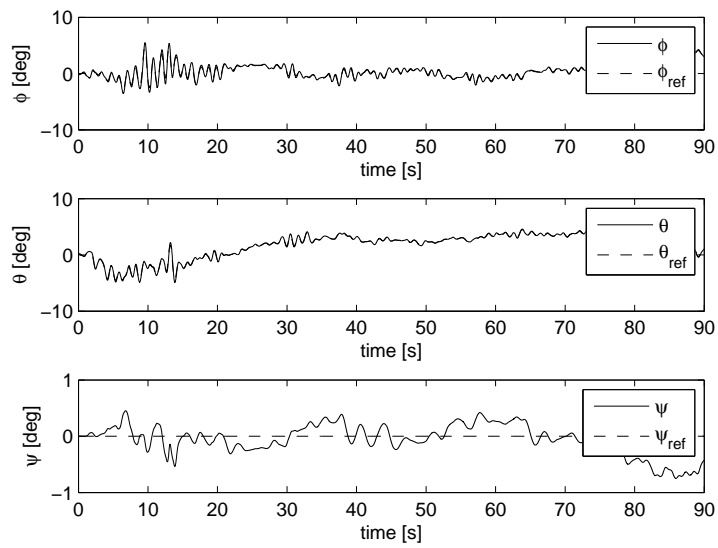


Figure 6.2: Attitude performance with disturbance observer

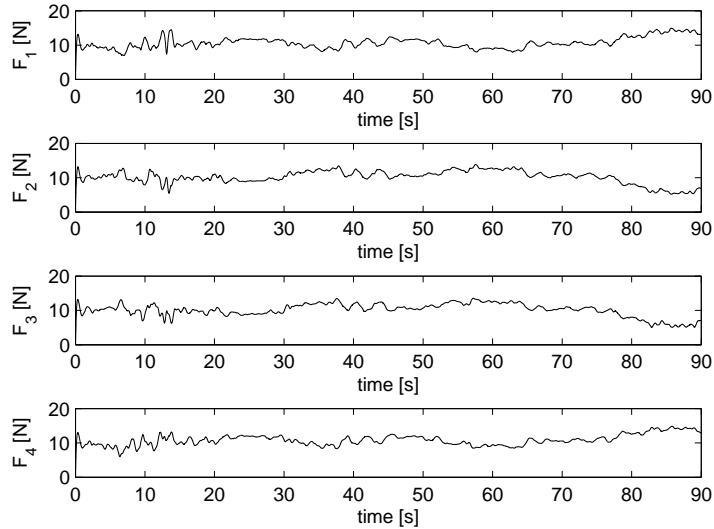


Figure 6.3: Motor thrust forces with disturbance observer

Figures 6.4 and 6.5 depict the wind forces on the aerial vehicle, that are generated by the Dryden wind model, and the estimation of the disturbances by the disturbance observer. The effecting force due to the winds is up to 6 N. Note that the estimation of the disturbance is very similar to the low-pass filtered shape of wind forces. This is due to the fact that winds have dominance on the total disturbance acting on the vehicle.

In the presence of the disturbance observer, the PID control system is able to hover the aerial vehicle in the close vicinity of the horizontal reference position despite the negative effects of the winds (Fig. 6.6).

The aerodynamic effects acting on the aerial vehicle reduce the performance of the hovering control, when these forces are not estimated and handled accordingly. The benefit of the disturbance observer becomes evident when the simulation is repeated without disturbance rejection (Fig. 6.7, 6.8).

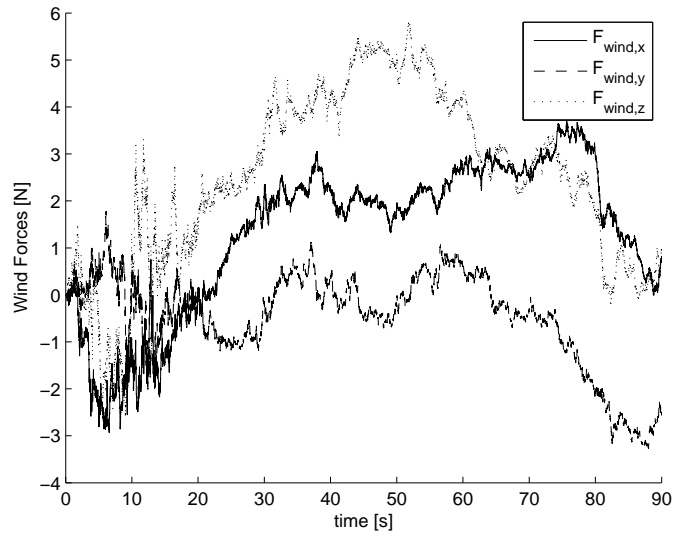


Figure 6.4: Wind forces acting as disturbance

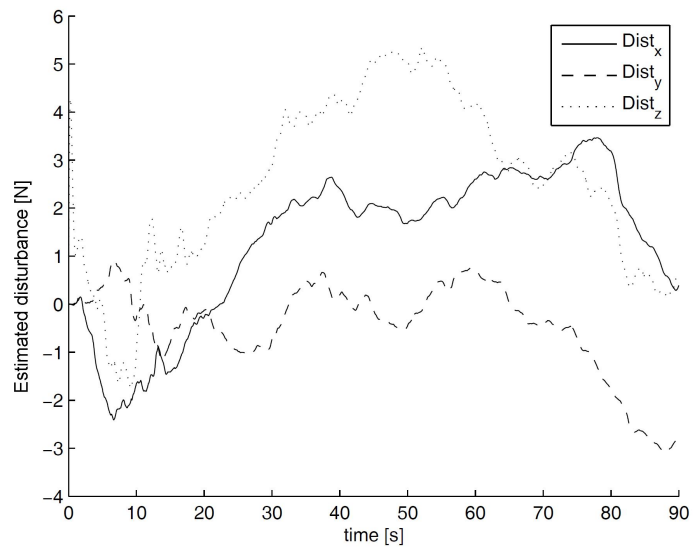


Figure 6.5: Estimated disturbance

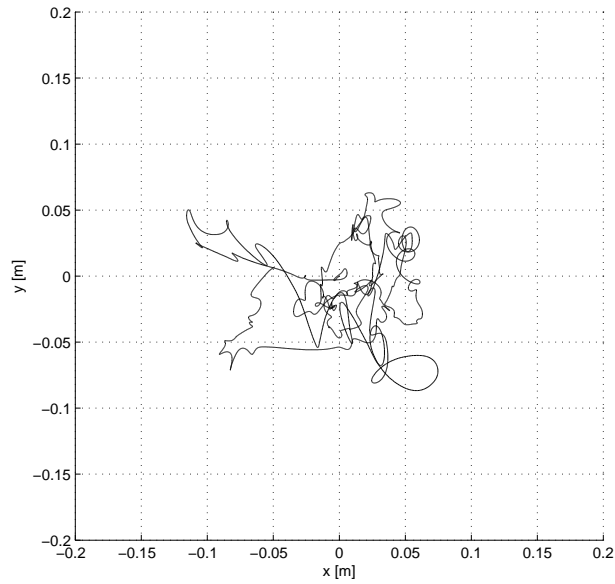


Figure 6.6: Hovering performance with disturbance observer (motion in the horizontal plane)

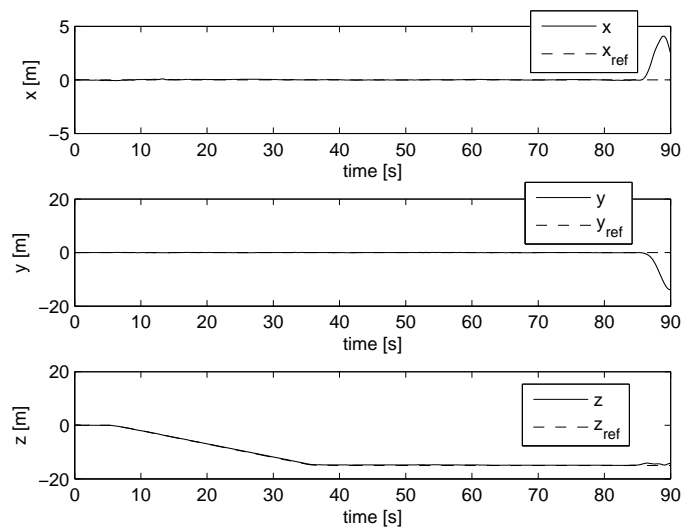


Figure 6.7: Hovering performance without disturbance observer

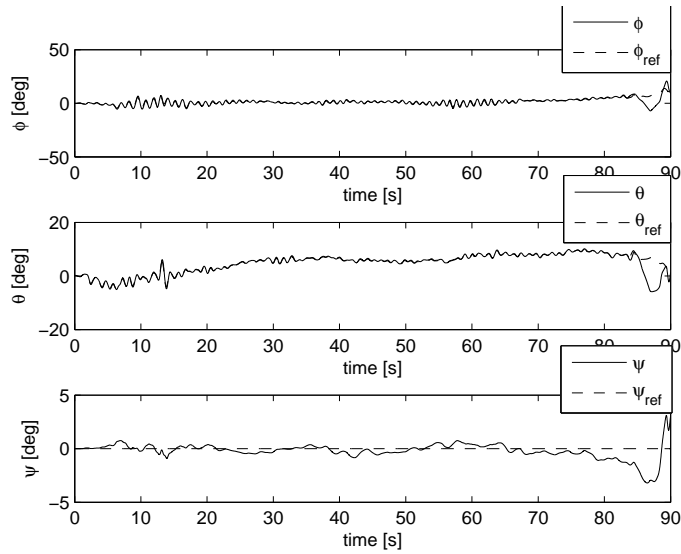


Figure 6.8: Attitude performance without disturbance observer

In this simulation, it is observed that the position errors in horizontal plane and attitude deviations are larger when compared with the results in Figures 6.1, 6.2. It is also evident, that the controller cannot keep the position and attitude errors of the aerial vehicle low when large disturbances, such as the one occurring at 86th second, exist. Consequently, the aerial vehicle moves away from the desired position as depicted in Figure 6.9.

6.1.2 GPS Based Trajectory Tracking

For the evaluation of the GPS based position control on a desired trajectory, the PID type GPS based trajectory tracking control algorithm, which is explained in Chapter 4, is employed on the dynamic model of SUAVI. The simulations in Simulink environment including the Dryden wind model based external disturbances are performed on elliptic and rectangular trajectories.

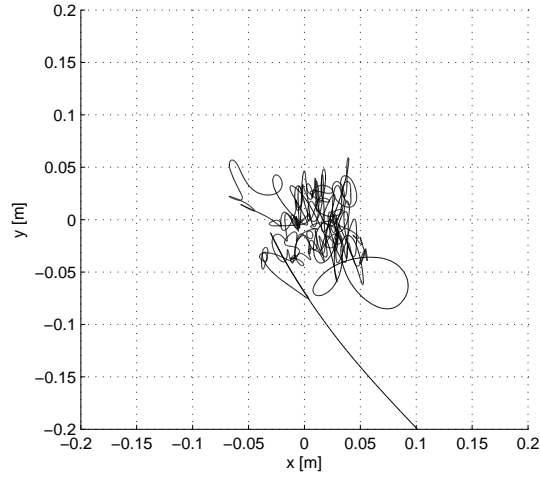


Figure 6.9: Hovering performance without disturbance observer (motion in the horizontal plane)

Since the disturbance rejection implies a linear model with nominal parameters, PID type controllers prove to be satisfactory. The implementation parameters are set as in Table 6.2.

Table 6.2: Implementation Parameters for Waypoint Navigation

Control	K_p	K_d	K_i
Roll	30	10	0.1
Pitch	30	15	0.1
Yaw	10	4	0.1
Altitude	40	15	0.1
Along track	1	0	0.1
Cross track	25	40	8

In the first simulation, the 3-D cartesian reference trajectory is defined as an ellipse, in which the aerial vehicle gains altitude up to a limit and then stays at constant altitude (Fig. 6.10). For this trajectory, the position of the aerial vehicle along with references and attitude angles are depicted in Figures 6.11 and 6.12.

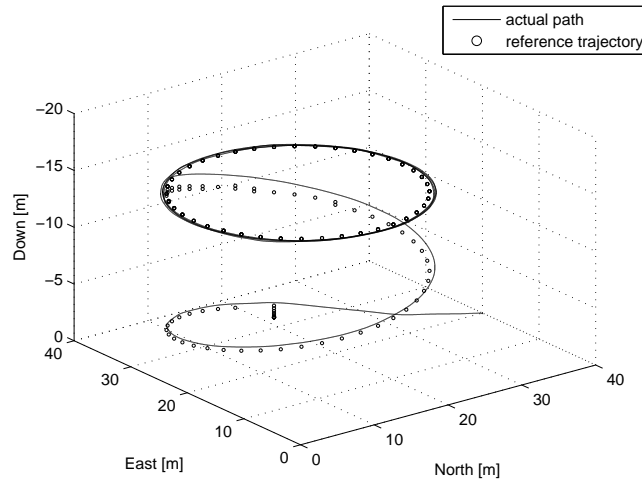


Figure 6.10: Elliptic trajectory tracking performance

It is worth to note that the position and angle references are tracked with reasonably small errors, where the position references are tracked with small phase shift due to the inertia and continuously changing position reference. The tracking errors of attitude angles do not exceed $\pm 2^\circ$. Moreover, the aerial vehicle follows its constant heading reference, $\psi_{ref} = 0^\circ$, with less than 1° error. The cross track error and the along track speed reference tracking performance are depicted in Figures 6.13, 6.14.

In these figures it is apparent, that the cross track error at steady state is less than 0.5 m, whereas the along track speed oscillates around its constant reference at a magnitude of 1.5 m/sec. As Figure 6.15 depicts, the required

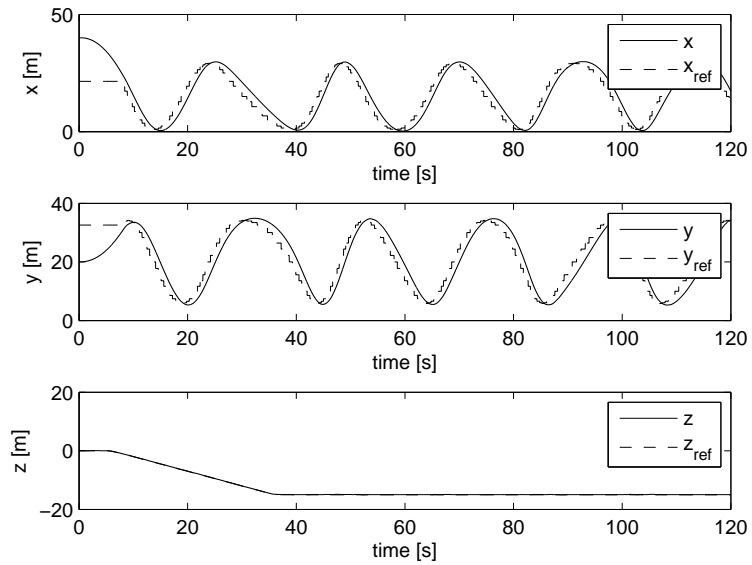


Figure 6.11: Position tracking performance

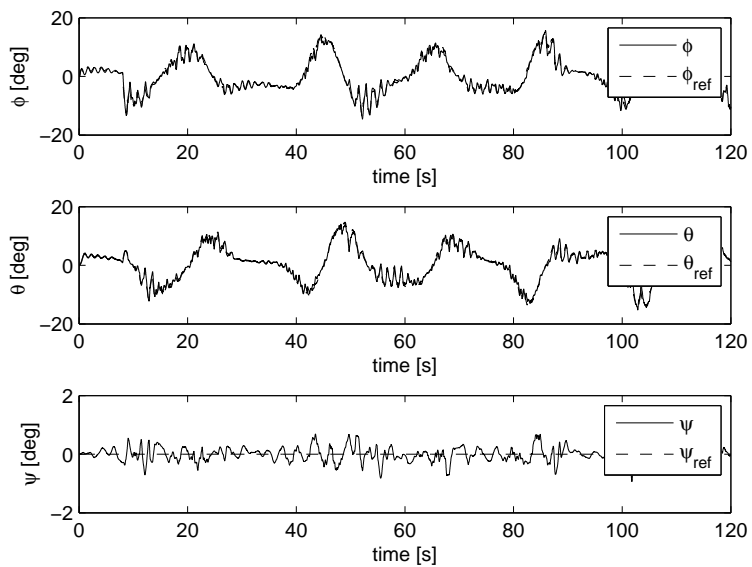


Figure 6.12: Attitude tracking performance

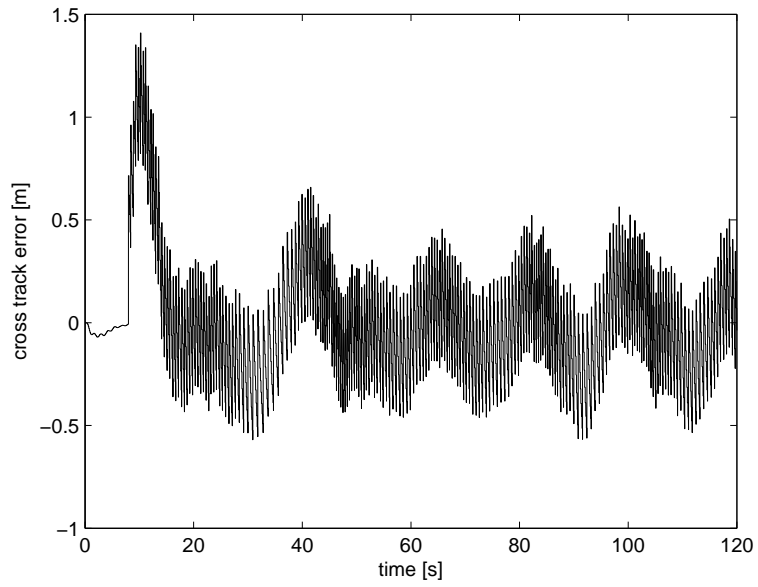


Figure 6.13: Cross track error

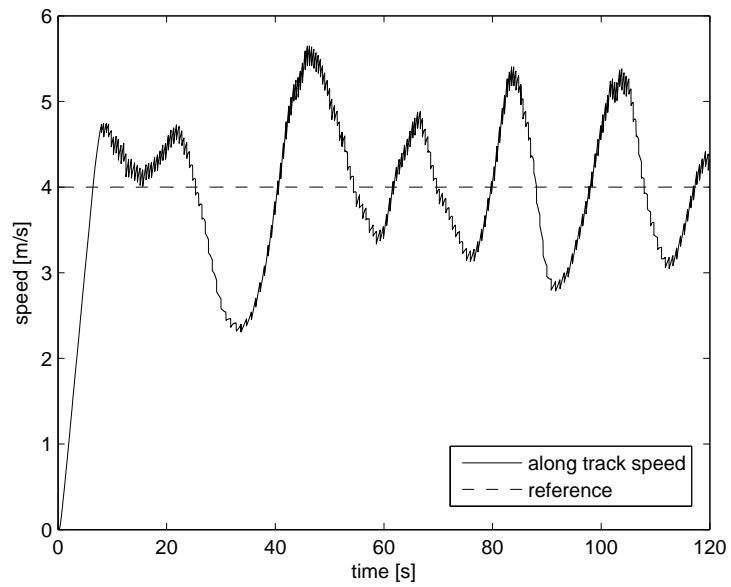


Figure 6.14: Along track speed

motor thrusts do not exceed 16 N, that is the limit of the motor-propeller couples utilized in SUAVI.

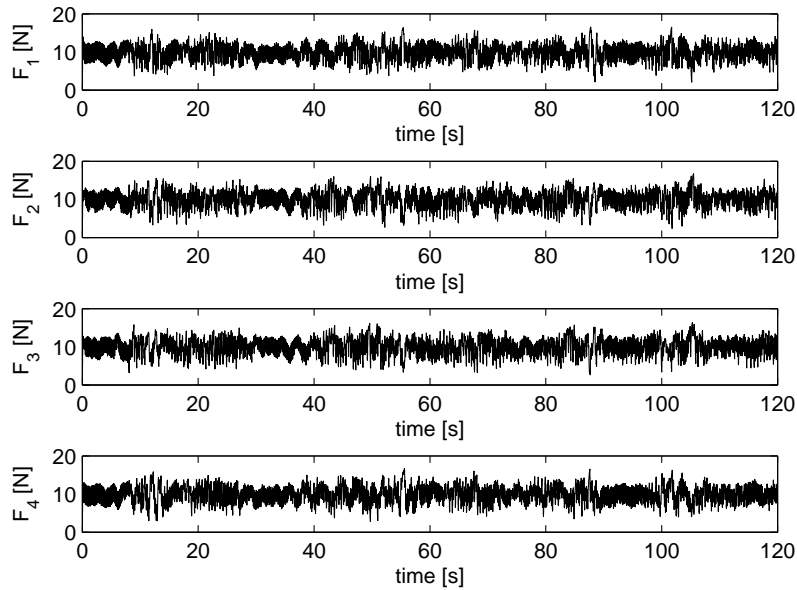


Figure 6.15: Thrust forces created by rotors

Figures 6.16 and 6.17 depict the wind forces on the aerial vehicle, that are generated by the Dryden wind model, and the estimation of the disturbances by the disturbance observer. It is obvious that the estimation of the disturbance is very similar to the low-pass filtered shape of wind forces. This is due to the fact that winds have dominance on the total disturbance acting on the vehicle.

In the second simulation, the cartesian reference trajectory is defined as a square. Figure 6.18 depicts the reference trajectory and the trajectory of the aerial vehicle. In this figure it is apparent that the error increases at sharp corners, where very instant reactions from the aerial vehicle are required to

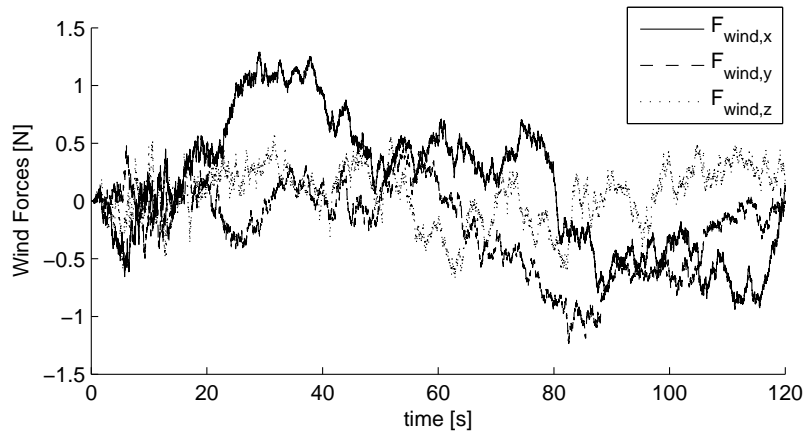


Figure 6.16: Wind forces acting as disturbance

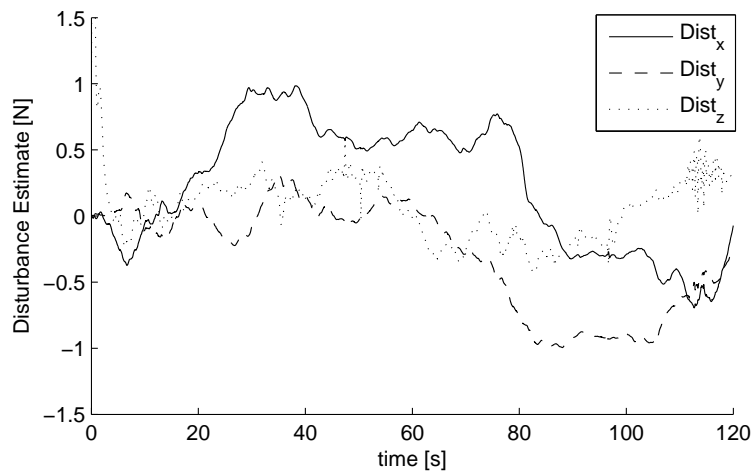


Figure 6.17: Estimated disturbance

keep the error at minimum level. Instead, a feasible reference trajectory, that does not have such sharp corners, can be defined for further improving the tracking performance.

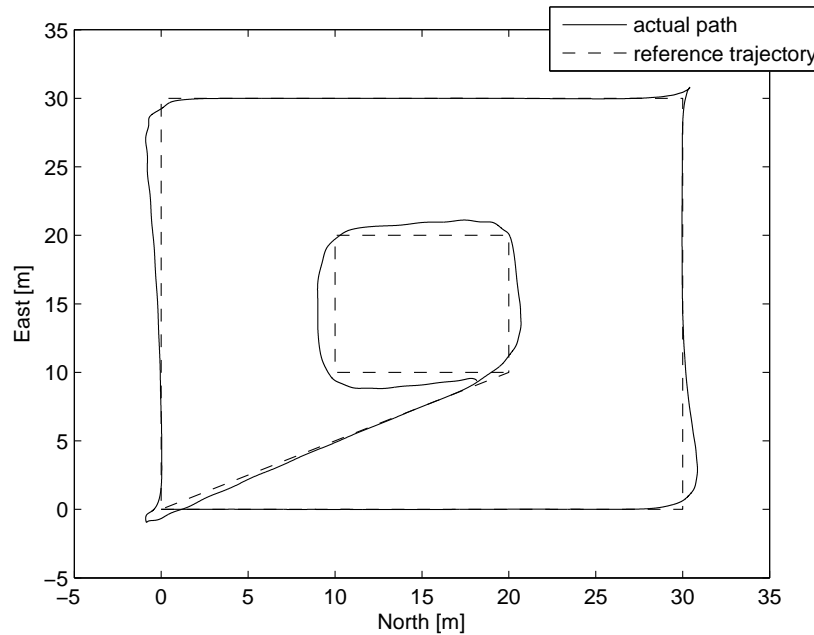


Figure 6.18: Square shaped trajectory tracking performance

6.2 Experimental Results

For developing control algorithms on the onboard control system of SUAVI, tuning the control variables and testing the performance of the supervisory control system, real flight experiments are performed both indoors and outdoors. The VTOL flight experiments are done first on a quadrotor platform, SUQUAD, that is developed as a by-product in this project (Fig. 6.19).

This platform is a quadrotor helicopter with a relatively simple structure, high tolerance for hard landings and simple repairing opportunities when

compared with SUAVI. It is equipped with the same control system, actuators and sensors and has also the same parameters in terms of dimensions and very similar weight and inertia values. It is a useful test platform not to risk SUAVI at every flight test. An advance in the control system is directly transferred to SUAVI if it proves to be safe and successful during flight tests.



Figure 6.19: SUQUAD test platform

6.2.1 Vertical Flight Stabilization Tests

The initial flight tests of SUAVI are focused on achieving stable vertical flights with SUAVI. In these tests both altitude and attitude stabilization performances are evaluated.

Figure 6.20 reveals the altitude reference tracking performance of the gravity compensated PID altitude controller during a stable hover of SUAVI. It is obvious that the aerial vehicle follows the reference with some oscillations despite the wind and the latency in the altitude measurements. These oscillations do not cause any instability though.

Figure 6.21 shows the attitude stabilization performance of the aerial vehicle. In this figure, it is apparent that the roll and pitch angle deviation is bounded by 2° . The vehicle is affected by the ground effect, which is caused

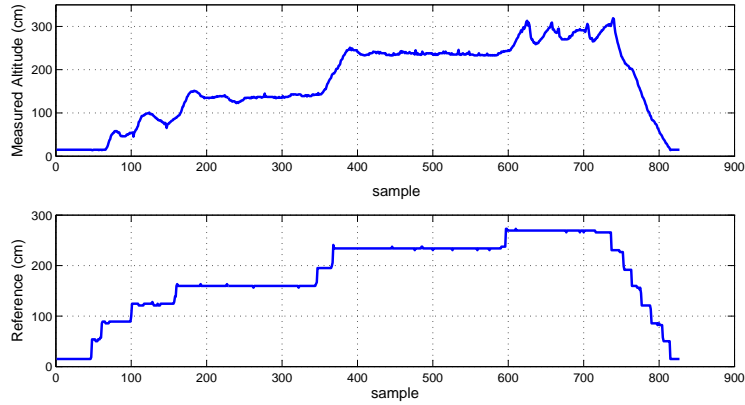


Figure 6.20: Altitude stabilization using PID

by the additional disturbance of the airflow reflection from the ground at altitudes less than 0.5 m. Even though, the attitude deviations do not exceed 3° in the presence of the ground effect. The snapshots of the test flight can be seen in Figure 6.22.

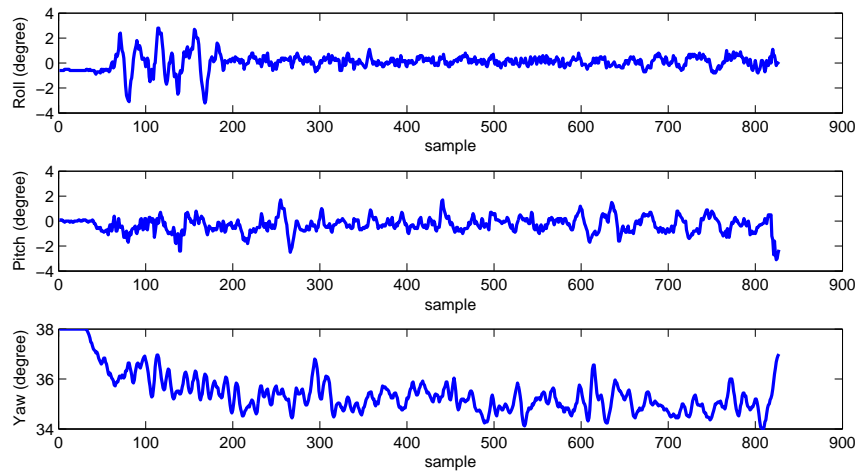


Figure 6.21: Attitude stabilization using PID

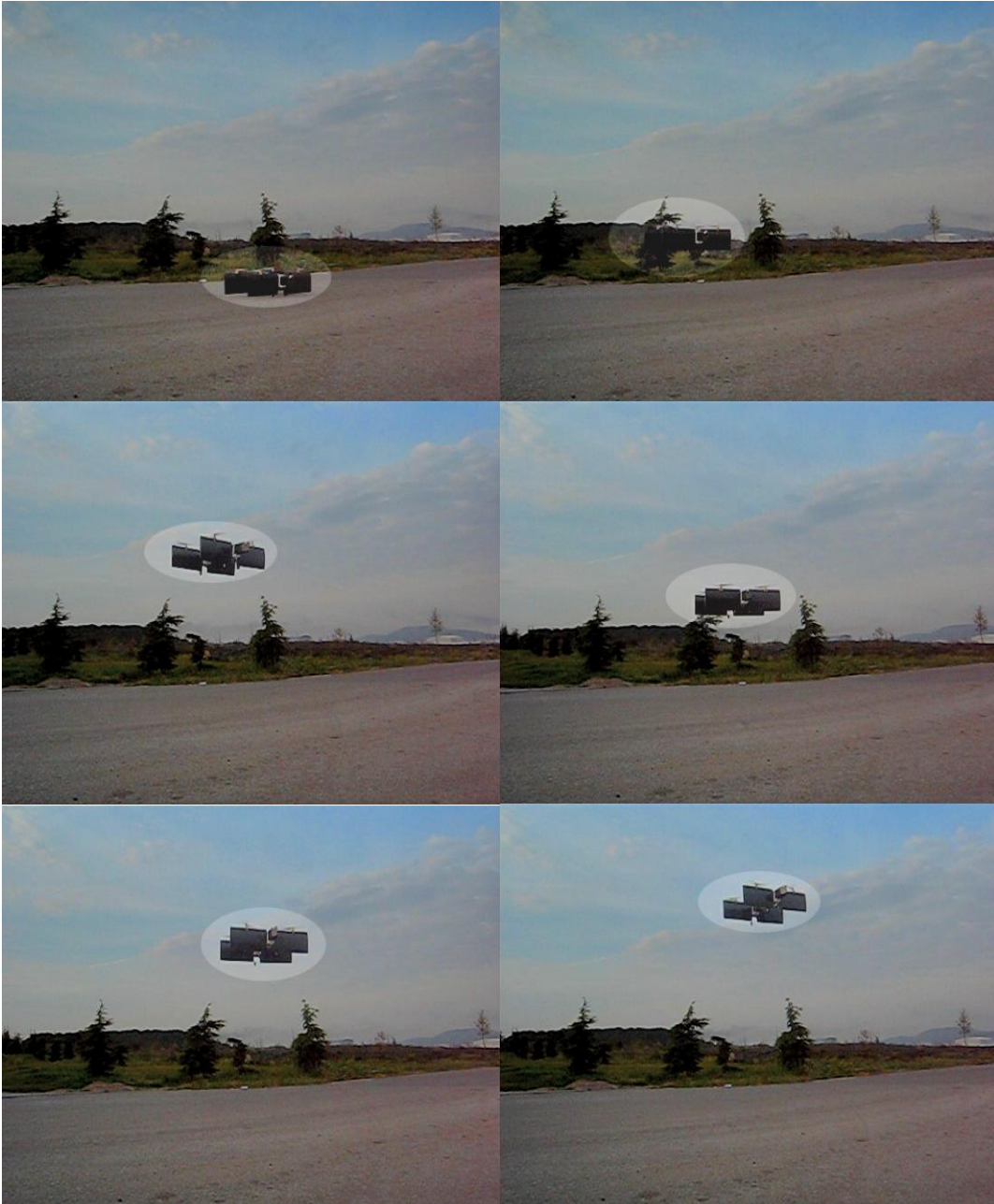


Figure 6.22: Snapshots during a vertical flight

6.2.2 GPS Based Hover during Vertical Flight

The GPS based hovering controller explained in Chapter 4 is implemented and tested on SUAVI after several successful tests on SUQUAD. Hovering tests in several open areas of Sabancı University under average winds and gusts are depicted in Figures 6.23, 6.24, 6.25 and 6.26. In these tests, the actual flight performance of SUAVI is found to be close to simulation results and the stability is proven to be high.

6.2.3 Horizontal Flight Tests

After the vertical flight tests with very good stabilization performance, horizontal flight tests on SUAVI are also conducted. During these tests, successful flights with up to 15 km/h horizontal speed are accomplished and SUAVI is landed safely. Snapshots from two horizontal flight tests are presented in Figures 6.27 and 6.28.



Figure 6.23: Outdoor hover test with SUAVI in helicopter field



Figure 6.24: Outdoor hover test with SUAVI in university campus

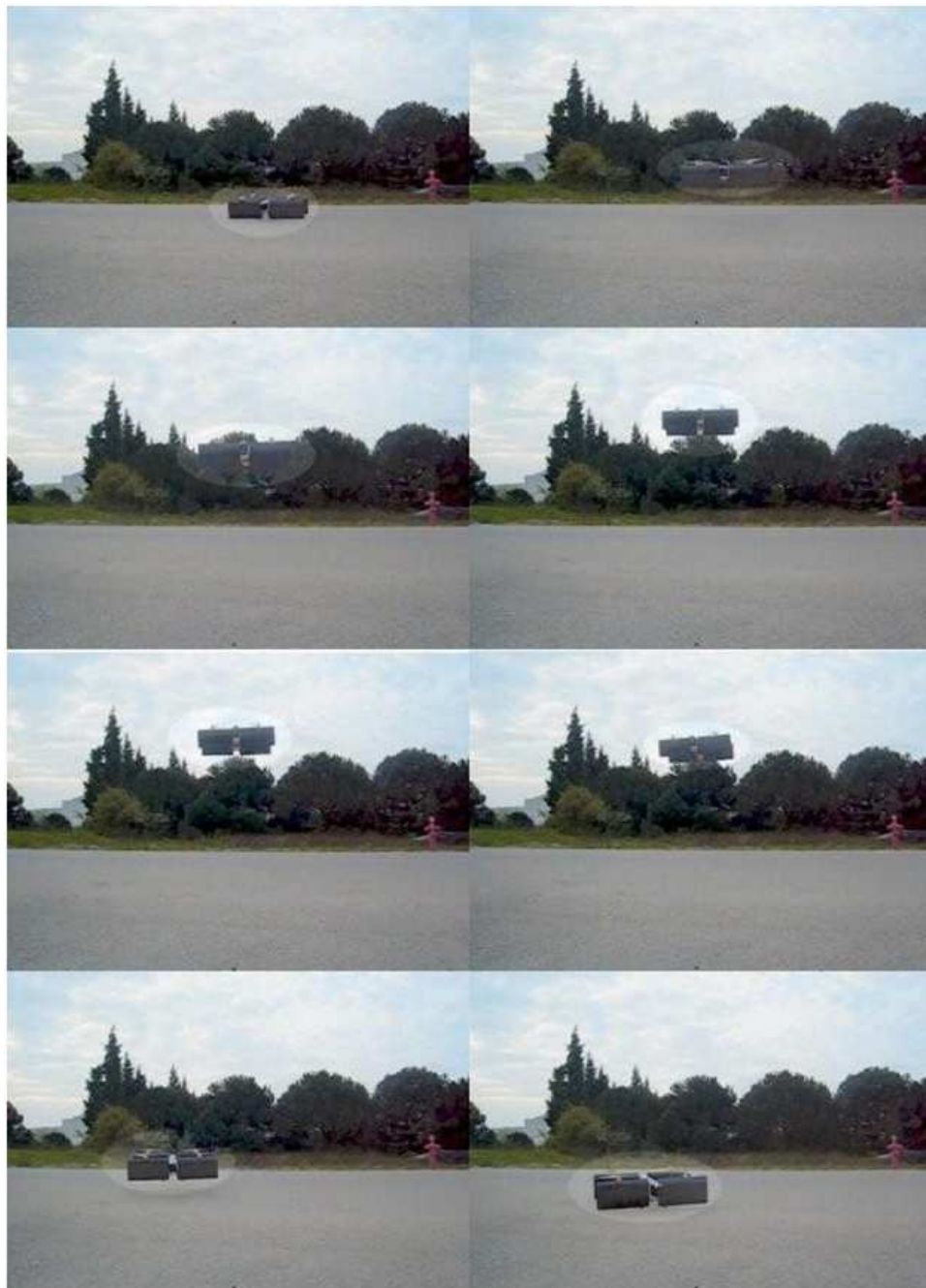


Figure 6.25: Outdoor hover test with SUAVI in university campus

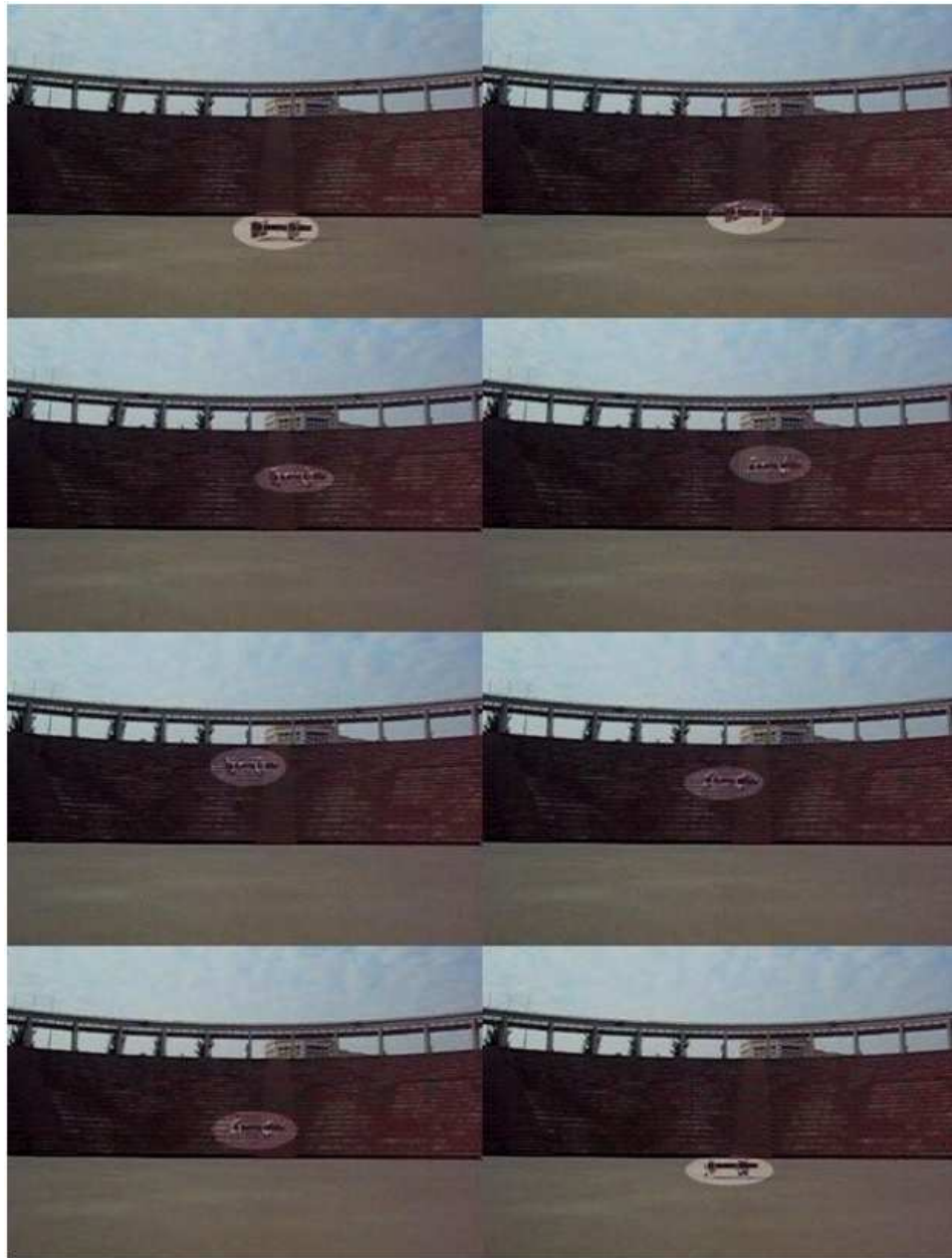


Figure 6.26: Outdoor hover test with SUAVI in amphitheater



Figure 6.27: Horizontal flight snapshots of SUAVI



Figure 6.28: Horizontal flight snapshots of SUAVI

Chapter 7

7 Concluding Remarks and Future Work

In this work, design, construction and flight control system of a conceptually new type of unmanned aerial vehicle (SUAVI: Sabancı University Unmanned Aerial Vehicle) are presented. The conceptual design of SUAVI is carried out taking the VTOL and horizontal flight capabilities, flight duration goals, and the power source and size limits into account. The aerodynamic design including the selection of the propulsion system components is carried out to maximize the aerodynamic efficiency and guarantee safe flight characteristics of the quad tilt-wing air vehicle. Several fluid flow simulation programs and test systems such as a test bench designed in the project and the wind tunnel test facility are utilized in this design and optimization process. The mechanical design of SUAVI is conducted to satisfy the strength, lightness and conformity to the mission criteria. Mechanical properties of several candidate materials are tested for the selection of the most appropriate production material. The design is performed in 3D CAD environment for accurate detailing of the mechanical design before production and for simulations performed in ANSYS. SUAVI is prototyped using carbon composite material with Aramid honeycomb core and CNC machined parts.

A full non-linear dynamical model including aerodynamic disturbances is developed using Newton-Euler formulation. A supervisory control architec-

ture is implemented on SUAVI where a Gumstix microcomputer behaves as a supervisor and orchestrates switching of low-level controllers into the system. Supervisory control is responsible for decision making, monitoring states of the vehicle, checking the safety during the flight and generating attitude references for the low-level controllers using GPS data. Various analog and digital filters are implemented to smooth out noisy sensor measurements. To obtain reliable orientation information by fusing data from low-cost MEMS inertial sensors such as gyros, accelerometers and the compass, Extended Kalman filter is implemented in the control system. For the execution of the flight controls, real-time control software is developed and tested.

To evaluate the performance of the control system on the SUAVI, numerous simulations and real flight tests are conducted. For the real flight tests, the developed control algorithms are implemented on the air vehicle through the supervisory control system. Initial tests are carried out on a quadrotor test platform (SUQUAD: Sabancı University QUADrotor), which is also produced in this work. SUAVI is tested with the proven control algorithms to verify the flight control system. In these tests hovering, VTOL and horizontal flights are successfully realized.

Future work includes fully autonomous flight of SUAVI from the takeoff to the landing based on the given flight trajectory reference.

References

- [1] A . R . Johnston. An Experiment in Manipulator Control with Proximity Sensors. In *Jet Propulsion Laboratory, California Institute of Technology*, April 1974.
- [2] Gourin C. G. Faust R. A. Hockstein, N. G. and D. J. Terris. A History of Robots: From Science Fiction to Surgical Robotics. *Journal of Robotic Surgery*, (1):113–118, 2007.
- [3] C. Hagsis. History of Robots. Master’s thesis, Wagner College, 2003.
- [4] Robot Technology: History. [online] http://www2.toyota.co.jp/en/tech/robot/p_robot/history.html.
- [5] M. Hirose and T. Takenaka. A History of Robots: From Science Fiction to Surgical Robotics. *Honda R&D Technical Rev.*, 13(1):1–6, 2001.
- [6] Toyota Partner Robot. [online] http://en.wikipedia.org/wiki/Toyota_Partner_Robot.
- [7] Watanabe R. Aoyama C. Matsunaga S. Higaki N. Sakagami, Y. and K. Fujimura. The Intelligent ASIMO: System Overview and Integration. In *IEEE International Conference on Intelligent Robots and Systems*, September 2002.
- [8] Human-Like Robots to Mimic Human Facial Expressions. [online] <http://www.infoniac.com/hi-tech/human-like-robots-to-mimic-human-facial-expressions.html>.

- [9] Robot Face Mimics Human Expression: Crosses Uncanny Valley. [online] <http://www.wired.com/gadgetlab/2007/09/robot-face-mimi/#ixzz0u5wMM6cm>.
- [10] Robotic Face Mimics Human Reactions. [online] <http://swns.com/robotic-face-mimics-human-reactions-101106.html>.
- [11] M. A. Turk, D. G. Morgenthaler, K. D. Gremban, and M. Marra. VITS-a Vision System for Autonomous Land Vehicle Navigation. *IEEE Transactions on Pattern Analysis and Machine Intelligence*, 10(3):342–361, May 1988.
- [12] Darpa Urban Competition. [online] <http://www.darpa.mil/grandchallenge/index.asp>.
- [13] Darpa Grand Challenge. [online] http://en.wikipedia.org/wiki/DARPA_Grand_Challenge.
- [14] McCord M. Mishalani R. Coifman, B. and K. Redmill. Surface Transportation Surveillance from Unmanned Aerial Vehicles. In *83rd Annual Meeting of the Transportation Research Board*, January 2004.
- [15] Hamel T. Suter, D. and R. Mahony. Visual Servo Control Using Homography Estimation for the Stabilization of an X4-Flyer. In *IEEE Conference on Decision and Control*, 2002.
- [16] Lee D. Tippetts B. J. Lillywhite K. D. Dennis A. W. Fowers, S. G. and J. K. Archibald. Vision Aided Stabilization and the Development of a Quad-Rotor Micro UAV. In *IEEE International Symposium on Computational Intelligence in Robotics and Automation*, 2007.

- [17] M. Seelinger and J. D. Yoder. Automatic Visual Guidance of a Forklift Engaging a Pallet. *Elsevier Robotics and Autonomous Systems*, 54:1026–1038, 2006.
- [18] Hong B. Tamba, T. A. and K. S. Hong. A Path Following Control of an Unmanned Autonomous Forklift. volume 7, pages 113–122, 2009.
- [19] Automated People Mover (APM). [online] http://en.wikipedia.org/wiki/People_mover.
- [20] Advanced Public Transport Systems-Phileas. [online] <http://www.apt-phileas.com/>.
- [21] Bao Q Yao Z. Ge Z. Xie, Y. and Z. Du. First Automatic Empty Container Yard with No Operator in China. In *International Technology and Innovation Conference*, 2006.
- [22] Volpe R. Backes P. Balaram J. Welch R. Ivlev R. Tharp G. Peters S. Ohm T. Petras R. Hayati, S. and S. Laubach. The Rocky 7 Rover: A Mars Sciencecraft Prototype. In *IEEE Conference on Robotics Automation*, 1997.
- [23] D. A Bickler. New Family of JPL Planetary Surface Vehicles. In *Missions, Technologies, and Design of Planetary Mobile Vehicles*, September 1992.
- [24] Foster-Miller Talon Armed UGV. [online] http://en.wikipedia.org/wiki/Foster-Miller_TALON.
- [25] Gardner K. Belluck D. A. Seager T. P. Kiker G. A. Yatsalo B. Tkachuk

- A. Kim J. Bridges T. S. Linkov, I. and R. Lahdelma. *Environmental Security in Harbors and Coastal Areas*. Springer, May 2007.
- [26] V. Bertram. Unmanned Surface Vehicles-A Survey. 2008.
- [27] Prior S. D. Karamanoglu M. Odedra S. Barlow C. Erbil, M. Aehmet Ali and D. Lewis. Reconfigurable Unmanned Aerial Vehicles. In *International Conference on Manufacturing and Engineering Systems*, pages 392–396, 2009.
- [28] A. Puri. A Survey of Unmanned Aerial Vehicles (UAV) for Traffic Surveillance. In *Department of Computer Science and Engineering, University of South Florida*, May 2008. [online] <http://www.csee.usf.edu/~apuri/techreport.pdf>.
- [29] ISTAR (Intelligence, Surveillance, Target Acquisition & Reconnaissance, September 2009. [online] <http://www.generaldynamics.uk.com/solutions-andcapabilities/istar>.
- [30] Lozano R. Salazar, S. and J. Escareno. Stabilization and Nonlinear Control for a Novel Trirotor Mini-Aircraft. *Elsevier Control Engineering Practice*, 17:886–894, February 2009.
- [31] H. Latchman and T. Wong. Statement of Work for Airborne Traffic Surveillance Systems - Proof of Concept Study for Florida Department of Transportation, October 2002. [online] http://www.list.ufl.edu/publications/atss_prop-oct-02-verb.pdf.
- [32] McCord M. Mishalani M. Coifman, B. and K. Redmill. Surface Transportation Surveillance from Unmanned Aerial Vehicles. In *83rd Annual Meeting of the Transportation Research Board*, 2004.

- [33] D. W. Murphy. The Air Mobile Ground Security and Surveillance System (AMGSSS). In *10th Annual ADPA Security Technology Symposium*, September 2005.
- [34] K. Nonami. Prospect and Recent Research & Development for Civil Use Autonomous Unmanned Aircraft as UAV and MAV. *Journal of System Design and Dynamics*, 1(2):120–128, 2007.
- [35] D. Travers. Brigade ISTAR Operations. *The Army Doctrine and Training Bulletin* 3, 3(4):43–49, 2000.
- [36] Ebbage L. McGuinness, B. Assessing Human Factors in Command and Control: Workload and Situational Awareness Metrics. In *Proceedings of the Command and Control Research and Technology Symposium*, 2002.
- [37] E. Crück and J. Lygeros. Sense and Avoid System for a MALE UAV. In *AIAA Guidance, Navigation and Control Conference and Exhibit*, August 2007.
- [38] P. Grigson and A. Gray. CFD Analysis of the Low-Speed Aerodynamic Characteristics of a UCAV. In *13th RPVs/UAVs International Conference*, 1999.
- [39] Everett H. R. Gilbreath G. Carroll, D. and K. Mullens. CFD Analysis of the Low-Speed Aerodynamic Characteristics of a UCAV. In *Missions, Technologies, and Design of Planetary Mobile Vehicles*, January 2006.
- [40] Attack of the Drones. [online] <http://www.newsweek.com/2009/09/18/attack-of-the-drones.html>.

- [41] U.S. Air Force Contemplates an All-UAV Future. [online] <http://homelandsecuritynewswire.com/us-air-force-contemplates-all-uav-future>.
- [42] The Demise of the F-22 Raptor: The Story Behind the Story. [online] <http://themoderatevoice.com/47669/the-demise-of-the-f-22-raptor-the-story-behind-the-story/>.
- [43] UAV as Sixth-Gen Fighter? [online] <http://www.airforce-magazine.com/DRArchive/Pages/2009/July%202009/July%2027%202009/UAVasSixth-GenFighter.aspx>.
- [44] Drone Wars. [online] <http://www.forbes.com/2009/06/01/northrop-boeing-defense-business-aviation-drones.html>.
- [45] Pentagon's Budget Review Boosts UAVs, Drops F-22, VH-71 and CSAR-X. [online] http://www.ainonline.com/ain-defense-perspective/single-publication-story/browse/0/article/pentagons-budget-review-boosts-uavs-drops-f-22-vh-71-and-csar-x-20415/?no_cache=1&tx_ttnews%5Bmode%5D=1.
- [46] Aeroplanes: Past, Present, And Future. [online] <http://luckybogey.wordpress.com/2010/03/23/aeroplanes-past-present-and-future/>.
- [47] Karamanoglu M. Odedra S. Foran T. Prior, S. D. and M. A. Erbil. Development of a Co-Axial Tri-Rotor UAV. In *24th Bristol International Unmanned Air Vehicle Systems Conference*, April 2009.

- [48] R. M. Howard and I. Kaminer. Survey of Unmanned Air Vehicles. In *IEEE American Control Conference*, 2005.
- [49] W. L. Chan. Computer Aided Landing Control System Design For A Fixed Wing UAV. Master's thesis, National Cheng Kung University, 2005.
- [50] Long L. N. Hanford, S. D. and J. F. Horn. A Small Semi-Autonomous Rotary-Wing Unmanned Air Vehicle (UAV). In *AIAA Infotech @ Aerospace Conference*, September 2005.
- [51] E. P. Anderson and R. W. Beard. An Algorithmic Implementation of Constrained Extremal Control for UAVs. In *AIAA Guidance, Navigation, and Control Conference*, 2002.
- [52] W. R. Ren and R. W. Beard. CLF-based Tracking Control for UAV Kinematic Models with Saturation Constraints. In *IEEE Conference on Decision and Control*, 2003.
- [53] Hovakimyan N. Kaminer I. Patel V. V. Cao, C. and V. Dobrokhodov. Stabilization of Cascaded Systems via L1 Adaptive Controller with Application to a UAV Path Following Problem and Flight Test Results. In *IEEE American Control Conference*, 2007.
- [54] P. Riseborough. Autonomous Take-Off and Landing Control for Small UAVs. In *5th Asian Control Conference*, July 2004.
- [55] Griffiths S. R. McLain T. W. Barber, D. B. and R. W. Beard. Autonomous Landing of Miniature Aerial Vehicles. In *AIAA Infotech@Aerospace Conference*, June 1994.

- [56] M. I. Lizarrage. Autonomous Landing System for a UAV. Master's thesis, Naval Postgraduate School, 2004.
- [57] O. Bourquardez and F. Chaumette. Visual Servoing of an Airplane for Auto-Landing. In *IEEE Conference on Intelligent Robots and Systems*, 2007.
- [58] O. Bourquardez and F. Chaumette. Visual Servoing of an Airplane for Alignment with respect to a Runway. In *IEEE Conference on Robotics and Automation*, 2007.
- [59] Suter D. Tung, D. and A. Bab-Hadiashar. Aircraft Approach Angle Estimation: Vision Based Landing. In *Technical Report MECSE-28-2003*.
- [60] Walker R. Fitzgerald, D. and D. Campbell. A Vision Based Forced Landing Site Selection System for an Autonomous UAV. In *IEEE International Conference on Intelligent Sensors, Sensor Networks and Information Processing*, 2005.
- [61] Walker R. Fitzgerald, D. and D. Campbell. A Vision Based Emergency Forced Landing System for an Autonomous UAV. In *Australian International Aerospace Congress Conference*, 2005.
- [62] Kim Z. Rathinam, S. and R. Sengupta. Vision-Based Following of Structures Using an Unmanned Aerial Vehicle (UAV). In *Research Report UCB-ITS-RR-2006-1*, 2006.
- [63] McGee T. Kim Z. Xiao X. Jackson S. Morimoto M. Rathinam S. Padiyal J. Frew, E. and R. Sengupta. Vision-Based Road-Following Using a Small Autonomous Aircraft. In *IEEE Aerospace Conference*, 2004.

- [64] Champion B. Pegard C. Kaaniche, K. and P. Vasseur. A Vision Algorithm for Dynamic Detection of Moving Vehicles with a UAV. In *IEEE Conference on Robotics and Automation*, 2005.
- [65] Chen B. M. Lee T. H. Cai, G. An Overview on Development of Miniature Unmanned Rotorcraft Systems. *Frontiers of Electrical and Electronic Engineering in China*, May.
- [66] Park I. Lee H.Y. Jung J.S. Hwang I.S. Kim S.J. Yun, C.Y. and S.N. Jung. A New VTOL UAV Cyclocopter with Cycloidal Blades System. In *American Helicopter Society 60th Annual Forum*, June 2004.
- [67] Sanchez A. Garcia O. Escareno, J. and R. Lozano. Triple Tilting Rotor mini-UAV: Modeling and Embedded Control of the Attitude. In *American Control Conference*, June 2008.
- [68] Frazzoli E. Mettler B. Piedmonte M. Gavrillets, V. and E. Feron. Aggressive Maneuvering of Small Autonomous Helicopters: A Human-Centered Approach. *AIAA Journal of Aerospace Computing, Information and Communication*, 20:795–807, 2001.
- [69] Chen B. M. Peng K. Dong M. Cai, G. and T. H. Lee. Modeling and Control System Design for a UAV Helicopter. In *14th Mediterranean Conference on Control and Automation*, 2006.
- [70] Chen B. M. Peng K. Dong M. Cai, G. and T. H. Lee. Design and Assembling of a UAV Helicopter System. In *5th International Conference on Control and Automation*, July 2005.
- [71] E. N. Johnson and D. P. Schrage. The Georgia Tech Unmanned Aerial

- Research Vehicle: GTMax. In *AIAA Guidance, Navigation, and Control Conference*, 2003.
- [72] Escareno J. Garcia O. Sanchez, A. and R. Lozano. Autonomous Hovering of a Noncyclic Tiltrotor UAV: Modeling, Control and Implementation. In *17th World Congress of the International Federation of Automatic Control*, July 2008.
- [73] Draganflyer X6 Helicopter Tech Specs, July 2009. [online] <http://www.draganfly.com/uav-helicopter/draganflyer-x6/specifications/>.
- [74] Dzul A. Castillo, P. and R. Lozano. Real-Time Stabilization and Tracking of a Four Rotor Mini-Rotorcraft. *IEEE Transactions on Control Systems Technology*, 12(4):510–516, July 2004.
- [75] Meister O. Schlaile C. Wendel, W. and G. F. , Trommer. An Integrated GPS/MEMS-IMU Navigation System for an Autonomous Helicopter. *Elsevier Aerospace Science and Technology*, May.
- [76] A. Tayebi and S. McGilvray. Attitude Stabilization of a VTOL Quadrotor Aircraft. *IEEE Transaction on Control Systems Technology*, May.
- [77] Lozano R. Dzul A. E. Castillo, P. *Modelling and Control of Mini-Flying Machines*. Springer, Berlin, 2005.
- [78] Rajnarayan D. Waslander S. Dostal D. Jang J. Hoffmann, G. and C. Tomlin. The Stanford Testbed of Autonomous Rotorcraft for Multi Agent Control (Starmac). In *23rd Digital Avionics Systems Conference*, 2004.

- [79] MikroKopter. [online] <http://www.mikrokoetter.de/ucwiki/en/MikroKopter?action=show&redirect=FrontPage>.
- [80] Salazar S. Sanchez A. Romero, H. and R. Lozano. A New UAV Configuration Having Eight Rotors: Dynamical Model and Real-Time Control. In *46th IEEE Conference on Decision and Control*, December 2007.
- [81] Deeg C. Hommel G. Musial M. Kondak, K. and V. Remuss. Mechanical Model and Control of an Autonomous Small Size Helicopter with a Stiff Main Rotor. In *IEEE/RSJ International Conference on Intelligent Robots and Systems*, 2004.
- [82] Mettler B. Gavrilets, V. and E. Feron. Nonlinear Model for a Small-size Acrobatic Helicopter. In *AIAA Guidance, Navigation, and Control Conference*, 2001.
- [83] Liu M. Chen, W. and Y. Ge. Subspace Model Identification Methods for Identifying the Small-Scale Unmanned Helicopter Dynamics. In *IEEE International Conference on Integration Technology*, 2007.
- [84] P. Kerrow. Modelling the Draganflyer Four-rotor Helicopter. In *IEEE International Conference on Robotics and Automation*, 2004.
- [85] B. Erginer and E. Altug. Modeling and PD Control of a Quadrotor VTOL Vehicle. In *IEEE Intelligent Vehicles Symposium*, 2007.
- [86] Mahony R. Pounds, P. and P. Corke. Modeling and Control of a Quadrotor Robot. In *Australasian Conference on Robotics and Automation*, 2007.

- [87] A. Tayebi and S. McGilvray. Attitude Stabilization of a VTOL Quadrotor Aircraft. *IEEE Transactions on Control Systems Technology*, May.
- [88] S. Bouabdallah and R. Siegwart. Full Control of a Quadrotor. In *IEEE/RSJ International Conference on Intelligent Robots and Systems*, 2007.
- [89] B. M. V. Gavrilets and E. Feron. Nonlinear Model for a Smallsize Aerobatic Helicopter. In *AIAA Guidance, Navigation and Control Conference*, 2001.
- [90] S. K. Kim and D. M. Tilbury. Mathematical Modeling and Experimental Identification of an Unmanned Helicopter Robot with Flybar Dynamics. *Journal of Robotic Systems*, 21(3), 2004.
- [91] Mettler B. Gavrilets, V. and E. Feron. Flight Test and Simulation Results for an Autonomous Aerobatic Helicopter. In *AIAA Guidance, Navigation, and Control Conference*, 2001.
- [92] Amidi O. Miller J. R. Vallidis N. Bergerman, M. and T. Dudek. Cascaded Position and Heading Control of a Robotic Helicopter. In *IEEE/RSJ International Conference on Intelligent Robots and Systems*, 2007.
- [93] Kroupa S. Spinka, O. and Z. Hanzalek. Control System for Unmanned Aerial Vehicles. In *IEEE International Conference on Industrial Informatics*, 2007.
- [94] Plestan F. Cheviron, T. and A. Chriette. A Robust Guidance and Control Scheme of an Autonomous Scale Helicopter in Presence of Wind

- Gusts. *International Journal of Control*, 82(12):2206–2220, February 2009.
- [95] Wyeth G. Roberts J. Buskey, G. Autonomous Helicopter Hover Using an Artificial Neural Network. In *IEEE International Conference on Robotics & Automation*, pages 1635–1640, 2001.
- [96] M. Earl and R. D’Andrea. Real-Time Estimation Techniques Applied to a Four-Rotor Helicopter. In *IEEE International Conference on Decision and Control*, 2004.
- [97] Pflimlin J. M. Hamel T. Metni, N. and P. Soueres. Attitude and Gyro Bias Estimation for a Flying UAV. In *IEEE/RSJ International Conference on Intelligent Robots and Systems*, 2005.
- [98] A. Baerveldt and R. Klang. A Low-Cost and Low-Weight Attitude Estimation System for an Autonomous Helicopter. In *IEEE International Conference on Intelligent Engineering Systems*, 1997.
- [99] J. H. Kim and S. Sukkarieh. Flight Test Results of GPS/INS Navigation Loop for an Autonomous Unmanned Aerial Vehicle (UAV). In *ION GPS Conference*, September 2002.
- [100] Sukkarieh S. Kim, J. H. and S. Wishart. Real-Time Navigation, Guidance and Control of a UAV Using Low-Cost Sensors. In *International Conference of Field and Service Robotics*, 2003.
- [101] C. S. Yoo and I. K. Ahn. Low Cost GPS/INS Sensor Fusion System for UAV Navigation. In *22nd Digital Avionics Systems Conference*, 2003.

- [102] Nonami K. Hirata M. Wang, W. and O. Miyazawa. Autonomous Control of Micro Flying Robot. *Journal of Vibration and Control*, May.
- [103] Wendel J. Trommer G. F. Schlaile, C. Stabilizing a Four-Rotor Helicopter Using Computer Vision. In *First European Micro Air Vehicle Conference and Flight Competition EMAV*, July 2004.
- [104] Micheli M. Donate G. Sinopoli, B. and T. J. Koo. Vision Based Navigation for an Unmanned Aerial Vehicle. In *IEEE International Conference on Robotics and Automation*, 2001.
- [105] Schulz H. W. Buschmann M. Kordes T. Winkler, S. and P. Vörsmann. Improving Low-Cost GPS/MEMS-Based INS Integration for Autonomous MAV Navigation by Visual Aiding. In *ION GNSS Conference*, 2004.
- [106] Schulz H. W. Buschmann M. Kordes T. Winkler, S. and P. Vörsmann. Horizon Aided Low-Cost GPS/INS Integration for Autonomous Micro Air Vehicle Navigation. In *First European Micro Air Vehicle Conference and Flight Competition EMAV*, 2004.
- [107] Ostrowski J. P. Altug, E. and C. J. Taylor. Quadrotor Control Using Dual Camera Visual Feedback. In *IEEE International Conference on Robotics and Automation*, 2003.
- [108] Dawson D. M. Chen J. Chitrakaran, V. K. and M. Feemster. Vision Assisted Autonomous Landing of an Unmanned Aerial Vehicle. In *IEEE Conference on Decision and Control, and the European Control Conference*, 2005.

- [109] Shakernia O. Sharp, C. S. and S. S. Sastry. A Vision System for Landing an Unmanned Aerial Vehicle. In *IEEE International Conference on Robotics and Automation*, 2001.
- [110] A. A. Proctor and E. N. Johnson. Vision-Only Approach and Landing. In *AIAA Guidance, Navigation, and Control Conference*, 2005.
- [111] Ma Y. Koo T. J. Hespanha J. Shakernia, O. and S. S. Sastry. Vision Guided Landing of an Unmanned Air Vehicle. In *IEEE Conference on Decision and Control*, 1999.
- [112] Montgomery J. F. Saripalli, S. and G. S. Sukhatme. Visually Guided Landing of an Unmanned Aerial Vehicle. *IEEE Transactions on Robotics and Automation*, June.
- [113] Montgomery J. F. Saripalli, S. and G. S. Sukhatme. Vision-based Autonomous Landing of an Unmanned Aerial Vehicle. In *IEEE Conference on Robotics and Automation*, 2002.
- [114] S. Saripalli and G. S. Sukhatme. Landing a Helicopter on a Moving Target. In *IEEE Conference on Robotics and Automation*, 2007.
- [115] Vidal R. Sharp C. S. Shakernia, O. and S. S. Sastry. Multiple View Motion Estimation and Control for Landing an Unmanned Aerial Vehicle. In *IEEE Conference on Robotics and Automation*, 2002.
- [116] P. Doherty and P. Rudol. A UAV Search and Rescue Scenario with Human Body Detection and Geolocalization. In *20th Australian Joint Conference on Advances in Artificial Intelligence*, 2007.

- [117] Sukhatme G. S. Garcia-Pardo, P. J. and J. F. Montgomery. Towards Vision-Based Safe Landing for an Autonomous Helicopter. *Elsevier Robotics and Autonomous Systems*, January.
- [118] J. Hintze. Autonomous Landing Of A Rotary Unmanned Aerial Vehicle In A Non-Cooperative Environment Using Machine Vision. Master's thesis, Brigham Young University, 2004.
- [119] Geyer C. Meingast, M. and S. S. Sastry. Vision Based Terrain Recovery for Landing Unmanned Aerial Vehicles. In *IEEE Conference on Decision and Control*, 2004.
- [120] Montgomery J. F. Johnson, A. and L. Matthies. Vision Guided Landing of an Autonomous Helicopter in Hazardous Terrain. In *IEEE Conference on Robotics and Automation*, 2005.
- [121] H. Eisenbeiss. A Mini Unmanned Aerial Vehicle (UAV): System Overview and Image Acquisition. In *International Workshop on Processing And Visualization Using High-Resolution Imagery*, 2004.
- [122] T. Madani and A. Benallegue. Backstepping Control with Exact 2-Sliding Mode Estimation for a Quadrotor Unmanned Aerial Vehicle. In *IEEE/RSJ International Conference on Intelligent Robots and Systems*, 2007.
- [123] Huzmezan M. Chen, M. A Simulation Model and H_∞ Loop Shaping Control of a Quad Rotor UAV. In *IASTED International Conference on Modeling, Simulation and Optimization*, 2003.
- [124] Won D.H. Kang M.S. Kim T.J. Lee H.G. Park, S. and S.J. Kwon. RIC (Robust Internal-loop Compensator) Based Flight Control of a

- Quad-Rotor Type UAV. In *IEEE/RSJ International Conference on Intelligent Robots and Systems*, 2005.
- [125] H. Voos. Nonlinear State-Dependent Riccati Equation Control of a Quadrotor UAV. In *IEEE International Conference on Control Applications*, 2006.
- [126] H. Voos. Nonlinear and Neural Network-based Control of a Small Four-rotor Aerial Robot. In *IEEE/ASME International Conference on Advanced Intelligent Mechatronics*, 2007.
- [127] Salazar-Cruz S. Escareno, J. and R. Lozano. Embedded Control of a Four-rotor UAV. In *IEEE American Control Conference*, 2006.
- [128] A. Hably and N. Marchand. Global Stabilization of a Four Rotor Helicopter with Bounded Input. In *IEEE/RSJ International Conference on Intelligent Robots and Systems*, 2007.
- [129] P. Castillo. Real-Time Stabilization and Tracking of a Four-Rotor Mini Rotorcraft. *IEEE Transactions on Control Systems Technology*, July.
- [130] Sergio-S. Anand S. Castillo P. Hugo, R. and R. Lozano. Modeling and Real-time Control Stabilization of a New VTOL Aircraft with Eight Rotors. In *IEEE/RSJ International Conference on Intelligent Robots and Systems*, 2007.
- [131] Sergio-S. Anand S. Castillo P. Hugo, R. and R. Lozano. A New UAV Configuration Having Eight Rotors: Dynamical Model and Real-Time Control. In *IEEE Conference on Decision and Control*, 2007.

- [132] W. Bath and J. Paxman. UAV Localisation & Control through Computer Vision. In *Australasian Conference on Robotics and Automation*, 2005.
- [133] Ostrowski-J. P. Altug, E. and R. Mahony. Control of a Quadrotor Helicopter Using Visual Feedback. In *IEEE International Conference on Robotics and Automation*, 2002.
- [134] G. R. Gress. Using Dual Propellers as Gyroscopes for Tilt-Prop Hover Control. In *Biennial International Powered Lift Conference and Exhibit*, November 2002.
- [135] The Bell Eagle Eye UAS, September 2008. [online] <http://www.bellhelicopter.com/en/aircraft/military/bellEagleEye.cfm>.
- [136] Min-B. Lee, J. and E. Kim. Autopilot Design of Tilt-rotor UAV Using Particle Swarm Optimization Method. In *IEEE International Conference on Control, Automation and Systems*, October 2007.
- [137] Fantoni-I. Kendoul, F. and R. Lozano. Modeling and Control of a Small Autonomous Aircraft Having Two Tilting Rotors. In *IEEE Conference on Decision and Control, and the European Control Conference*, December 2005.
- [138] Wong K.C. UAV Design Activities in a University Environment. In *9th Australian International Aerospace Congress*, March 2001.
- [139] Poinot-D. Thipyopas C. Bataille, B. and J.M. Moschetta. Fixed-Wing Micro Air Vehicles with Hovering Capabilities. In *NATO RTO meeting, AVT-146, Symposium on Platform Innovations and System Integration for Unmanned Air, Land and Sea Vehicles*, May 2007.

- [140] R.H. Stone and G. Clarke. The T-Wing: A VTOL UAV for Defence and Civilian Applications. In *Flight International's UAV Australia Conference*, February 2001.
- [141] Miles D. Cifdaloz O. Wells V. L. Dickeson, J. J. and A. A. Robriguez. Robust LPV H Gain-Schedules Hover-to-Cruise Conversion for a Tilt-Wing Rotorcraft in the Presence of CG Variations. In *American Control Conference*, July 2007.
- [142] Fully autonomous quad tilt wing UAV makes maiden flight. [online] <http://www.flightglobal.com:80/articles/2008/03/20/222373/fully-autonomous-quad-tilt-wing-uav-makes-maiden-flight.html>.
- [143] R. H. Barnard and D. R. Philpott. *Aircraft Flight: A Description of the Physical Principles of Aircraft Flight*. Prentice Hall, Upper Saddle River, NJ, 2004.
- [144] L. Dingle and M. Tooley. *Aircraft Engineering Principles*. Elsevier Butterworth-Heinemann, Oxford, 2005.
- [145] B. W. McCormick. *Aerodynamics, Aeronautics, and Flight Mechanics*. Wiley, NY, 1995.
- [146] J. D. Anderson. *Fundamentals of Aerodynamics*. McGraw-Hill, Boston, 2001.
- [147] J. A. Franklin. *Dynamics, Control, and Flying Qualities of V/STOL Aircraft*. American Institute of Aeronautics and Astronautics, Reston, VA, 2002.

- [148] M. E. Dreier. *Introduction to Helicopter and Tiltrotor Flight Simulation*. American Institute of Aeronautics and Astronautics, Reston, VA, 2007.
- [149] I. H. Abbott and A. E. von. Doenhoff. *Theory of Wing Sections*. Dover Publications Inc., 1959.
- [150] R. E. Sheldahl and P. C. Klimas. Aerodynamic Characteristics of Seven Symmetrical Airfoil Sections Through 180 Degree Angle of Attack For Use in Aerodynamic Analysis of Vertical Axis Wind Turbines. July 1981. [online] <http://prod.sandia.gov/techlib/access-control.cgi/1980/802114.pdf>.
- [151] Vacuum Bagging and Sandwich Core Construction, 1995. [videorecording].
- [152] V. Kelly. *Carbon Fiber: Manufacture and Applications*. Kidlington, Oxford, UK; Elsevier, NY, USA, 2004.
- [153] Americal Society for Testing and Materials. C 297-94 Standard Test Method for Flatwise Tensile Strength of Sandwich Contructions. 2002.
- [154] T Bresciani. Modeling Identification and Control of a Quadrotor Helicopter. Master's thesis, Department of Automatic Control, Lund University, 2008.
- [155] K. T. Öner, E. Çetinsoy, E. Sırımoğlu, C. Hançer, M. Ünel, M. F. Akşit, K. Gülez, and İ. Kandemir. Mathematical Modeling and Vertical Flight Control of a Tilt-Wing UAV. In *Turkish Journal of Electrical Engineering and Computer Sciences*, 2009.

- [156] K. T. Öner. Modeling and Control of a New Unmanned Aerial Vehicle (SUAVİ) with Tilt-Wing Mechanism. Master's thesis, Sabanci University, 2009.
- [157] Steven L. Waslander and Carlos Wang. Wind disturbance estimation and rejection for quadrotor position control. *In AIAA Infotech@Aerospace Conference and AIAA Unmanned...Unlimited Conference*, April 2009.
- [158] K. Ohnishi and T. Murakami. Advanced motion control in robotics. In *Industrial Electronics Society, 1989. IECON '89., 15th Annual Conference of IEEE*, pages 356 –359 vol.2, 6-10 1989.
- [159] K. Kondak, M. Bernard, N. Meyer, and G. Hommel. Autonomously flying vtol-robots: Modeling and control. In *Robotics and Automation, 2007 IEEE International Conference on*, pages 736 –741, 10-14 2007.
- [160] R. E. Kalman. A New Approach to Linear Filtering and Prediction Problems. *Transactions of the ASME, Journal of Basic Engineering*, (82 (Series D)):35–45, 1960.